Formation of Embedded Nitride Semiconductor Nanocrystals

by

Adam W. Wood

A dissertation submitted in partial fulfillment
of the requirements for the degree of
Doctor of Philosophy
(Physics)
in the University of Michigan
2012

Doctoral Committee:

Professor Rachel S. Goldman, Chair
Professor Roy Clarke
Professor Ctirad Uher
Associate Professor Kevin P. Pipe

© Adam W. Wood
2012

Acknowledgements

I would like to thank my family and friends, all of the teachers that have ever taught me, and give a special thanks to my fellow group members, past and present.

Support from the U.S. Department of Defense through the Intelligence Community Postdoctoral Research Fellowship under grant HM1582-05-1-2027, by the AFOSR through the MURI program under Grant No. FA9950-08-1-0340, and the CIA under Contract No. 2007-0919714-000 is gratefully acknowledged.

Table of Contents

Acknowledgements ii

List of Tables vi

List of Figures vii

List of Appendices xii

Abstract xiii

Chapter 1 Introduction 1

1.1 Overview 1

1.2 III-V Nitrides 2

1.3 Nanostructured Semiconductors 4

1.4 Synthesis of Nanostructures 8

1.5 Directed Seeding of Nanostructures 13

1.6 Dissertation Objectives 14

1.7 Dissertation Organization 15

References 21

Chapter 2 Experimental Procedures 32

2.1 Overview 32

2.2 Broad-Area Ion Implantation 33

2.3 Thermal Annealing 34

2.4 Transmission Electron Microscopy Sample Preparation 35

2.5 Transmission Electron Microscopy 38
2.6 X-Ray Energy Dispersive Spectroscopy 40
2.7 Channeling Rutherford Backscattering Spectrometry 40
2.8 References 54
Chapter 3 Formation Mechanisms of Embedded InN Nanocrystals 55
3.1 Overview 55
3.2 Background 56
3.3 Experiments 56
3.4 Nitrogen Incorporation 57
3.5 Nanocrystal Formation 58
3.6 Nanocrystal Phase Analysis 60
3.7 Nanocrystal Size Distribution 61
3.8 Mechanisms of Nanocrystal Nucleation 62
3.9 Conclusions 63
3.10 References 72
Chapter 4 Formation of GaN-rich Nanocrystals in Nitrogen Implanted GaAs 75
4.1 Overview 75
4.2 Background 75
4.3 Experimental Details 76
4.4 Role of Implantation Energy 77
4.5 Temperature-dependence of GaN Nucleation 78
4.6 Annealing Time-dependence of GaN Nucleation 79
4.7 Mechanisms for ZB vs. WZ GaN Nucleation 79
4.8 TTT Diagram 80

4.9 Conclusions 83

4.10 References 95

Chapter 5 Spatially Directed Formation of Embedded Zincblende GaN Nanocrystals ... 98

5.1 Overview 98

5.2 Background 98

5.3 Experimental Details 99

5.4 Depth-Dependence of Ion Damage 100

5.5 Nucleation of ZB Nitride Nanocrystals 102

5.6 Directed Seeding of GaN Nanocrystals 103

5.7 Mechanisms for ZB GaN Nucleation 104

5.8 Conclusions 106

5.9 References 116

Chapter 6 Summary and Suggestions for Future Work 118

6.1 Summary 118

6.2 Suggestions for Future Work 120

6.3 References 135

Appendices 138

List of Tables

Table 1.1 A comparison of the physical properties of AlN, GaN, and InN in both the ZB and WZ phases. 18

Table 1.2 Calculated exciton Bohr radii for selected semiconductors.......... 19

Table 3.1 Interplanar spacings of InAs:N following RTA at 550 and 600°C, determined from SAD, in comparison with the powder diffraction data for InAs and InN.. 64

Table 4.1 Literature reports on N ion irradiation of GaAs, followed by thermal annealing at various temperatures for times ranging from 30 s to 120 min. 85

Table 4.2 Interplanar spacings measured by SAD of GaAs:N following implantation at ion energies of 75-keV and 100-keV, and RTA at 800°C, in comparison to powder diffraction standards. 86

Table 5.1 A comparison of the interplanar distances measured by selected area diffraction of GaAs:N following RTA at 550 and 600°C with the powder diffraction data for GaAs and GaN. 107

List of Figures

Fig. 1.1 Ion beam synthesis of nitride nanostructures. In (a), a high dose of nitrogen ions (5.0×10^{17} cm^{-2} at 100 keV) is implanted into an epitaxial GaAs film to produce a supersaturated "amorphous" layer. In (b), after thermal annealing, nano-scale crystallites form within the disordered matrix.. 20

Fig. 2.1 Schematic of a typical ion implanter. 44

Fig. 2.2 Diagram of the furnace annealing setup. The sample sits between GaAs annealing caps on a quartz boat. The entire boat setup sits within a quartz tube purged with flowing gas controlled externally. 45

Fig. 2.3 Diagram of the rapid thermal annealing setup. The sample sits on a silicon wafer with a thermocouple contact on the underside. The chamber is purged with flowing nitrogen or argon gas and the sample is heated by a halogen lamp housed inside a quartz window.. 46

Fig. 2.4 Schematic of plan-view TEM specimens prepared by chemical etching. (a) The original sample is (b) polished from the back to a thickness of ~200 μm before (c) mounting film side down on a glass side using Crystalbond™. (d) The back of the sample is then covered in wax and a soldering iron is used to (e) melt holes in the wax coating. The sample is then dipped in solution and (f) etched until there is a perforation on the film side of the sample. 47

Fig. 2.5 Optical microscope views of chemically etched GaAs:N showing (a) an etched hole where etching was stopped after perforation, leaving a smooth edge along the hole and an undamaged surface. In (b), an etched hole was not removed from the etchant following perforation, resulting in a jagged hole edge and a partially etched, damaged surface layer. 48

Fig. 2.6 Schematic of cross-sectional TEM polishing. The sample is (a) cleaved into two equal parts and (b) glued film side together using epoxy. The Sample is then (c) mounted on a polishing stub and polished on one side before (d) mounting on a TEM grid and polishing the opposite side to a final thickness of 75-100 μm. The sample is then (e) placed in an Ar ion miller and milled until a perforation is formed in the center of the sample. 49

Fig 2.7 Schematic of FIB lift-out TEM sample preparation. An area of interest (a) is identified and then (b) a protective layer of Pt is deposited on the area of

interest. The FIB is then used to mill trenches away from the sides of the Pt, as well as to (d) thin the area of interest. The FIB is then used to (e) cut notches spanning the area of interest, but leaving enough material to maintain contact between the sample and the bulk material. A tungsten needle is then brought in and (f) attached to the sample using Pt deposition. The FIB is then used to (g) cut notches to free the sample from the bulk material. The sample can then be lifted out on the needle and (h) deposited on a TEM half-grid using Pt deposition, where it is then (i) disconnected from the needle using the FIB beam. 50

Fig. 2.8 Ray diagrams showing how the objective lens/aperture are used in combination to produce (a) a BF image from the direct beam and (b) a centered dark field image where the incident beam is tilted so that the scattered beam remains on axis. (Adapted from Ref. 3) 51

Fig. 2.9 Geometry of a backscattering experiment, illustrating the collection of backscattered particles in a solid angle Ω. 52

Fig. 2.10 Channeling in (a) a perfect crystal, for which the incident ion undergoes only small-angle scattering within the channel. Dechanneling may occur when the incident ion interacts with lattice defects, as shown in (b). 53

Fig. 3.1 SRIM simulation of vacancy and nitrogen concentrations as a function of depth for 100-keV N implantation into InAs. The vacancy concentration (solid) spans depths of 0 to ~300 nm, with a maximum at a depth of ~125 nm (solid arrow). The nitrogen concentration (dashed) spans depths of 0 to ~350 nm, with a maximum at a depth of ~200 nm (dashed arrow). The distribution of vacancies is consistent with the width of the amorphous layer following implantation..... 65

Fig. 3.2 (a) Cross-sectional HAADF STEM image and corresponding 2D XEDS spectral maps of a typical iplanted-plus-RTA sample with a nanocrystal-rich surface layer (S) and crystalline middle layer (M). Using the line-cut indicated in (a), with the y-coordinate expanded by 63%, the atomic ratios are presented for (c) In, (e) As, and (g) N. Popped Nitrogen bubbles are labelled with circles. 66

Fig. 3.5 Size distributions of the crystallites in implanted-plus-RTA InAs:N for RTA at (a) 550ºC and (b) 600ºC, estimated from analysis of dark-field TEM images. The size distribution was fit with a Poisson regression, overlayed on the distribution. A maximum likelihood estimate of nanocrystal radius gives r_{ML} values of 1.3 and 2.6 nm, respectively. 69

Fig. 3.6 Plot of the difference between the free energies of formation for WZ and ZB InN following RTA at 550°C (dashed line) and 600°C (solid line). For radii less than 6.5 Å (6.25 Å), the ZB phase is thermodynamically favored, while the WZ phase is favored for larger radii. 70

Fig. 3.7 Models of (a) ZB and (b) WZ GaN. Close packed surface planes are indicated in pink. There is a higher density of close packed {111} surface planes for ZB nanocrystals in comparison to the {001} close packed surface planes of WZ... 71

Fig. 4.1 Annealing time vs. annealing temperature for N ion-implanted GaAs, compiled from the references in Table 4.1. Short (30s) anneals at high temperatures lead to the nucleation of ZB GaN (square). Following high temperature annealing for longer annealing times (>1 min), WZ GaN (hexagon) is observed. In some FA studies, Ga-N bonding is reported (triangle) without identification of a phase. ... 87

Fig. 4.2 Dark-field TEM images of annealed GaAs:N layers implanted at (a) a dose of $2.5x10^{17}$ and ion energy of 75 keV and (c) a dose of $5.0x10^{17}$ and ion energy of 100 keV. The corresponding SAD patterns collected from the nanocrystal (NC) layer of (a) and (c) are presented in (b) and (d), respectively. ... 88

Fig. 4.3 SRIM simulations of vacancy concentration vs. implantation depth following N^+ implantation at 100-keV (solid) and 75-keV (dashed). The predicted maximum vacancy concentration for 100-keV implantation is approximately twice that for 75-keV implantation. ... 89

Fig. 4.5 Dark-field TEM of GaAs:N following furnace annealing at 650ºC for 10 minutes. The corresponding SAD pattern, presented in (b), indicates nucleation of WZ GaN. ... 91

Fig. 4.6 Models of (a) ZB and (b) WZ GaN. Close packed surface planes are indicated in pink. A higher density of close packed {111} surface planes for ZB nanocrystals in comparison to the {001} close packed surface planes of WZ is apparent. ... 92

Fig. 4.7 Plot of GaN nanocrystal size at nucleation vs. annealing temperature for rapid thermal annealed GaAs:N. Data contained in this thesis (squares) and data from Ref. 8 (circle) suggests that size increases with anneal temperature from 650 to 800°C, reaching a maximum size of 1.75 nm, as shown by the dashed line..... 93

Fig. 4.8 TTT diagram for ZB and WZ GaN formation based upon literature reports and data contained in this thesis. WZ GaN nucleation is indicated by triangles. Annealing paths for select RTA and FA temperatures are overlaid for comparison (dashed lines). For RTA at 650°C for 30 s, formation of ZB GaN (square) is observed. During the subsequent quench to RT, formation of polycrystalline GaAs is also observed. For RTA at 750°C for 30 s, formation of ZB GaN begins at 14 s; polycrystalline GaAs is not observed following the quench to RT. In the case of FA at 650°C for 10 min, formation of WZ GaN is observed and subsequent quenching to RT does not lead to the formation of polycrystalline GaAs. ... 94

Fig. 5.1 SEM image of FIB-milled trenches in GaAs:N. The trenches act as regions of increased vacancy concentration. FIB liftout techniques were used to create

cross sectional TEM samples perpendicular to the trenches (dotted line). Deep trenches were milled for position marking. 108

Fig. 5.2 SRIM simulations of the depth-dependence of vacancy and nitrogen concentrations for (a) 75 keV and (b) 100 keV N^+ ions implanted into GaAs overlaid onto dark-field TEM images of implanted-and-RTA GaAs. The regions of highest vacancy concentration (solid line) and highest nitrogen concentration (dashed line) from the simulation correspond to layers with crystallite formation and blistering, as shown in the underlying images. 109

Fig. 5.3 Channeling-RBS spectra as a function of backscattered energy of GaAs layers, comparing 100 and 75 keV as-implanted (solid lines) and implanted-and-RTA (dashed lines) samples with GaAs in the random and (001) aligned configurations. For the 75 keV (100 keV) as-implanted layer, a broad peak which spans depths from 0 to 250 nm (0 to 300 nm), indicated by brackets, is observed. Following RTA, minima from 0 to 150 nm (0 to 100 nm) indicate partial recovery of the lattice damage, at depths corresponding to those where nanocrystal nucleation is observed. 110

Fig. 5.4 Schematic of the directed matrix seeding process. N+ ions are broad-area implanted into the substrate to create a highly damaged, N-rich surface (a). Ga+ FIB irradiation is used to introduce regions of elevated vacancy concentration (b). Following thermal annealing, GaN is nucleated in the FIB irradiated regions (c). 111

Fig. 5.5 Dark field TEM image of (a) 75 keV and (c) 100 keV implanted-plus-FIB-and-RTA GaAs. Polycrystalline nanocrystals with a clustering of crystallites near the bottom of the FIB milled trenches appear as bright spots in the TEM image. The SAD patterns collected from the polycrystalline layers of (a) and (c), shown in (b) and (d), reveal the formation of ZB GaN in both cases. 112

Fig. 5.6 SRIM simulations of 30-keV Ga implanted into GaAs. The vacancy concentration is centered about a depth of ~18 nm. 113

Fig. 5.7 Schematic of the directed matrix seeding process, consisting of (a) broad-area high energy nitrogen ion irradiation to produce a N super-saturated amorphous layer, (b) FIB irradiation to produce arrays of localized high vacancy concentration, and (c) rapid thermal annealing to enable spatially–directed nanocrystal nucleation. 114

Fig. 5.8 Plot of the difference between the free energies of formation for WZ and ZB GaN following RTA at 800°C. For radii less than 2.10 Å, the ZB phase is thermodynamically favored, while the WZ phase is favored for larger radii. . 115

Fig. 6.1 Schematic of pump/probe thermal conductivity measurements. An optical signal (pump) hits the surface (a), creating a localized region of increased temperature (red). A stress pulse (black) is generated by the thermal expansion of the material. The pulse is (b) reflected off of interfaces in the material

(orange), where it returns to the origin and the stress alters the reflectivity, which is measured with a probe beam. 128

Fig. 6.2 Time-resolved thermoreflectance of GaAs:N obtained using a pump/probe technique. The thermal conductivity is lowest for high energy (100 keV) implantation, with a slight increase following RTA. All values are below those of bulk GaAs (55 W/mK). 129

Fig. 6.3 SRIM simulation of vacancy concentration introduced by 30 keV Ga incident on GaAs. For 3-D growth, the vacancy distribution should span depths similar to the nitrogen distribution from broad-area implantation. 130

Fig. 6.4 SRIM simulation of N concentration as a function of depth for broad-area N implantation into GaAs for various implantation energies. As implantation energy is reduced, the depth distribution of [N] is reduced. For 10-keV implantation, the maximum [N] is at a depth of ~20 nm. 131

Fig. 6.5 Schematic of the proposed directed seeding process using plasma-source FIB processing. A N FIB (a) is used to selectively pattern a surface with regions of high nitrogen and vacancy concentrations. Thermal annealing (b) would then be used to nucleate nitride nanocrystals in the FIB-processed regions. 132

Fig. 6.6 Schematic of the 2-D directed matrix seeding process. N+ ions are broad-area implanted into the substrate to create a highly damaged, N-rich surface (a). Ga+ FIB irradiation is used to introduce a patterned surface of elevated vacancy concentration (b). Following thermal annealing, GaN is nucleated in the FIB irradiated regions (c). 133

Fig. 6.7 Schematic of in-situ MBE/FIB experiment for nitride nanostructure growth. Conventional MBE growth is used to grow thin films of Ga(In)NAs. The sample is then processed using a UHV FIB mounted directly on the growth chamber and annealed using a substrate heater. This process can then be repeated to create multiple layers of nitride nanostructures. 134

List of Appendices

Appendix A Selected Area Electron Diffraction Analysis 139

Appendix B Calculation of Atomic Ratio Using the Cliff-Lorimer Factor.................... 147

Appendix C Free Energy of Wurtzite and Zincblende Nanocrystal Nucleation 153

Appendix D Measuring Thermal Conductivity Using Pump/Probe............................... 158

Abstract

Formation of Embedded Nitride Semiconductor Nanocrystals

by

Adam W. Wood

Chair: Rachel S. Goldman

In this thesis, the formation, phase selection, and spatial positioning of GaAs:N (InAs:N) nanocomposite layers produced by N-implantation, focused ion beam (FIB) irradiation, and rapid thermal annealing (RTA) of GaAs (InAs) were investigated.

To examine nanocrystal formation mechanisms, the influence of annealing temperature and annealing time on phase formation in GaAs:N were examined. For RTA times of 30 s, we observed the nucleation of zincblende (ZB) GaN at temperatures of 650 to 900ºC. For furnace anneal (FA) times of 10 min, wurtzite (WZ) GaN nucleation was observed for anneal temperatures as low as 650ºC. In the case of InAs:N, for RTA at 500-550ºC ZB InN nanocrystals were nucleated. However, RTA temperatures of 600ºC led to the nucleation of WZ InN nanocrystals with a larger average diameter. These results indicated the key role of annealing time and temperature on crystallite nucleation. A TTT diagram was developed for GaN nucleation in ion-implanted GaAs. The TTT diagram provides an annealing schedule for the selective formation of ZB and WZ GaN.

The formation mechanisms for nucleation of ZB and WZ GaN (InN) were investigated and a thermodynamic model for the preferential nucleation of the ZB phase was proposed. ZB nanocrystals had a higher density of low-energy surface planes, which drove the adoption of the ZB phase for sufficiently small nuclei. We demonstrated the first nucleation of ZB and WZ InN in InAs using ion-implantation followed by thermal annealing.

Finally, a new process for simultaneous nanostructuring and phase selection, termed "directed matrix seeding," was demonstrated. Broad-area N^+ implantation of GaAs followed by rapid thermal annealing led to the formation of nanocrystals at the depth of maximum ion damage. With additional irradiation using a Ga^+ focused ion beam, selective lateral positioning of the nanocrystals within the GaAs matrix was observed in isolated regions of increased vacancy concentration. Following rapid thermal annealing, the formation of zincblende GaN was observed in the regions of highest vacancy concentration. The directed matrix seeding process offers a method for precisely controlling the phase and spatial location of embedded nitride nanostructures in a variety of host materials.

Chapter 1

Introduction

1.1 Overview

For more than 55 years, silicon has been developed and extensively used for semiconductor electronics. III-V materials such as GaAs, AlAs, InP, GaP and related materials have been developed more recently for optoelectronics. However, these materials are intolerant of elevated temperatures and caustic environments.[1,2] For example, Si and GaAs devices are limited to temperatures below 250ºC and 350ºC, respectively, by junction leakage currents[3,4] and contact chemical stability.[5,6] Wide bandgap materials are of great interest for aggressive environment applications because their physical properties including thermal conductivities, breakdown electric fields, and thermal and chemical stability up to high temperatures, are superior to silicon and lower bandgap III-V compounds.[7,8]

Wide bandgap materials, such as the II-VI direct bandgap Zn,Cd,Be-S,Se,Te-related family have recently been developed for optoelectronic applications.[9,10,11,12,13] However, there is a general problem with ZnSe-type materials in that there is an intrinsic defect formed during the nucleation of the first heteroepitaxial monolayers which causes threading dislocations to penetrate into the active quantum well layer of the material.[14,15,16] Under high current injection, such as in lasing applications, the defects

are energized in nonradiative recombination processes at point defect sites within the quantum well. Dislocation multiplication leads to the development of optically inactive dark lines and ultimately, the failure of the device.[17]

III-V nitrides are excellent candidates for wide bandgap applications where high-power or high-temperature operation is essential.[18,19] III-V nitride materials may be grown by solution-based, solvo-thermal, detonation, or physical deposition. However, these techniques do not offer control over size and shape uniformity of nanocrystals.[20,21,22,23,24] Additionally, they typically suffer from agglomeration of the nanoparticles,[20,21,22,25] or suffer from impurities arising from the growth method.[20,26,27] In this thesis, a new technique for the growth of GaN (InN) nanostructures embedded in a GaAs (InAs) host matrix using ion implantation followed by thermal annealing is discussed.

This chapter opens with a description of the unique physical properties predicted and observed in III-V nitride materials. Next, we provide motivation for studies of nanostructured semiconductor materials. This is followed by a review of growth methods of nitride nanostructures and a discussion on the spatial ordering of nanocomposites. Finally, the chapter concludes with an outline and objectives of the dissertation.

1.2 III-V Nitrides

The III-V nitrides of primary interest are the direct bandgap group AlN-GaN-InN and their alloy systems. Most commonly, GaN, AlN, and InN crystallize in the hexagonal wurtzite (WZ) form;[28,29,30] however, there have been several reports of a cubic

zincblende (ZB) phase under certain growth conditions.[31,32,33,34] These materials offer a wide range of bandgaps, from 6.2 eV for AlN to 0.65-0.8 for InN.[7,35,36] A comparison of physical properties of III-nitrides is presented in Table 1.1. GaN and related compounds have been studied for potential applications in LEDs operating through the visible spectrum, and as electronic devices suited for high temperature, high power, and high frequency applications.[37,38] For example, in the GaN-InGaN system, light emitting diodes (LEDs) covering the color range from UV to orange have been achieved.[39,40,41,42] These InGaN LEDs have power efficiencies that are competitive with incandescent lamps in applications such as traffic lights, vehicles, large displays, etc.[39,4344] Other developments include nitride-based blue and violet lasers with high output powers and long lifetimes that make them attractive for projector and optical data storage applications.[45]

While GaN usually crystallizes in a WZ lattice, ZB GaN has also been reported, offering several advantages over WZ GaN, including lower bandgaps (3.28-3.23 eV[46,47] vs. 3.5 eV), and higher carrier mobilities.[48] WZ GaAsN has potential applications toward short-wavelength lasers,[49,50] and LEDs fabricated on $(10\bar{1}0)$ *m* plane WZ GaN have shown polarized spontaneous light emission, potentially useful in liquid crystal display applications.[51] In addition, the piezoelectric WZ nitrides have potential applications in field-effect transistors tuned by applying stress to the device.[52] Alternatively, ZB GaAsN is promising for optical communications (λ 1.3-1.55 μm) and may be readily integrated with existing ZB III-V semiconductor substrates and devices.[53]

ZB InN offers several potential benefits over WZ InN. Recently, interest in InN has been renewed due to reports of a low bandgap energy of 0.65-0.8 eV[54,55] in lieu of the

previously accepted value of 1.7-2.2eV for WZ InN.[56,57] Interestingly, the band gap of ZB InN is predicted to be 0.58 eV,[58] slightly below that of WZ InN, providing an opportunity for extending nitride based LEDs to the near infrared. ZB InN formation has been reported in 2D crystals[59,60,61] and nanowires,[62] and 3D nanoparticles,[63,64,65] although the formation of InN nanocrystals embedded in InAs and the conditions for selective phase formation of ZB vs. WZ InN have not been reported.

1.3 Nanostructured Semiconductors

1.3.1 Optoelectronic Properties

In semiconductor nanostructures, there is a size-dependent increase or reduction in the effective bandgap.[66] If the semiconductor is approximated as an infinite potential well, the energy of an electron in level *n* in a well with dimension *a* is given by:[67]

$$E = \frac{h^2 n^2}{8ma^2} \tag{1.1}$$

where *m* the electron mass and *h* is the Planck constant. As the nanostructure size is reduced, there is a splitting of the energy levels and the quantum confinement effects become more noticeable. The size at which quantum confinement effects begin to alter the properties of the nanostructure with respect to the bulk is given by the Bohr exciton radius. A table of Bohr exciton radii for selected semiconductors is presented in Table 1.2.

There are several limitations to producing nanostructures with sizes on the order of the exciton Bohr radius. The minimum size of nanostructures formed by Stranski-

Krastanow (SK) growth range from 10 to 20 nm in diameter,[68,69,70] sufficient for quantum-confinement in materials with a large Bohr exciton radius (e.g. InAs: 30-34 nm). [71,72] However, for materials with smaller Bohr exciton radii (e.g. GaN: 2.8-11 nm),[73,74,75] the nanostructure must be correspondingly small. For SK growth, the sizes of the nanostructures are limited by the misfit strain between the film and substrate.[76,77] Although this inherent limitation does not hold for droplet epitaxy of QDs,[78] the smallest droplet epitaxy GaN dots reported to date have similar diameters (~10 to 30 nm).[79,80,81]

Additionally, there are limitations to the performance of solution-based nanostructures. Solution-based synthesis of compound semiconductor nanostructures often results in intermittent fluorescence,[82,83,84] likely due to electron diffusion at the surface.[85,86,87] However, reductions in intermittence have been observed by immobilizing the colloids near metallic nanostructures.[88] Thus, alternative methods for fabricating these nanostructures embedded in controlled nanostructure environments are promising for reductions in intermittence. Ion-beam synthesis, discussed below, offers a promising route to the controlled formation of nanostructures as small as ~5 nm[89,90] with zero-dimensional quantum confinement.

1.3.2 Thermoelectric Properties

Low-dimensional structures are predicted to lead to an increased thermoelectric figure-of-merit, *ZT*, in comparison to bulk materials. *ZT* is defined as:

$$ZT = \frac{S^2\sigma}{\kappa}T \qquad (1.2)$$

where σ is the electrical conductivity, *S* is the Seebeck coefficient, *T* is temperature, and κ is the thermal conductivity. In bulk materials, including non-degenerate semiconductors,[91] the electrical conductivity and electronic contribution to the thermal conductivity (κ_e) are linked by the Wiedemann Franz law:

$$\frac{\kappa_e}{\sigma T} = C_{WFL} \quad (1.3)$$

where C_{WFL} is a constant (the Wiedemann-Franz-Lorenz coefficient). For most bulk materials, an increase in σ corresponds to a proportional increase in κ_e, resulting in minimal net benefit in terms of *ZT*. However, it has been predicted[92] and observed[93] that the electrical and thermal conductivities may be decoupled for quantum-confined structures. Increased phonon scattering at phase boundaries between the nanoparticles and the matrix is expected to lead to a decrease in thermal conductivity.[94,95] Additionally, due to the increased control of the density of states and hence, the energies of charge carriers, nanocomposite materials are predicted to have a significantly higher thermoelectric power factor ($S^2\sigma$) compared to bulk materials.[96] Nanoscale (~1.5 nm) inclusions of metallic and semimetallic particles are predicted to enhance the Seebeck coefficient via electron energy filtering.[97] For example, 2 – 3 nm sized ErAs nanoparticles embedded in InGaAlAs have been shown to increase the thermoelectric power factor by 8%.[98] In addition, arrays of 10 nm diameter InAs quantum dots have been predicted to exhibit an increased thermoelectric power factor in comparison with bulk GaAs.[99,100]

There have been several improvements in ZT using multi-component nanostructured thermoelectrics such as $Bi_2Te_3/Sb_2/Te_3$ thin-film superlattices.[101] It has also been reported that 100-fold improvements in ZT can be achieved over bulk Si by

varying size and impurity levels in nanostructured Si.[102] These results are expected to be applicable to other classes of semiconductor nanomaterials, and there have been several recent advances in the development of these materials for thermoelectric applications. For example, nanostructured porous GaAs has been reported to exhibit an order of magnitude decrease in thermal conductivity compared to bulk GaAs, with the thermal conductivity decreasing with a decrease in particle size.[103] A 450% increase in thermoelectric power factor was recently predicted for nanostructured GaAs in comparison to its bulk counterpart.[104] In both cases, the thermoelectric properties are heavily dependent on the nanostructure size.

It is predicted that 3-D ordered quantum dot superlattices lead to a lower electrical conductivity and, consequently, a decrease in the thermoelectric power factor ($S^2\sigma$, where S is the Seebeck coefficient and σ is the electrical conductivity) with respect to the bulk.[105] This decrease in σ is due to quantum dot spacings sufficiently small enough for strong interactions between the electronic wave functions of the quantum dots. This interaction leads to a delocalization of electrons and miniband formation in 3-D. The decreased density of states with respect to the bulk leads to a lower predicted σ. However, for one-dimensional chain of both Ge/Si and InAs/GaAs systems, there is a predicted increase in σ such that $S^2\sigma$ is much higher than that of both the 3-D superlattice array and the bulk.[106] Additionally, $S^2\sigma$ of the one-dimensional chains is predicted to increase with decreasing quantum dot size. Hence, the one-dimensional nature of conduction could be exploited to yield a thermoelectric enhancement. However, in order to realize this enhancement, a method must be employed for the spatial ordering of nanostructures.

1.4 Synthesis of Nanostructures

Several techniques have been explored for the synthesis of GaN nanostructures including colloidal growth, solvo-thermal preparation, detonations, epitaxial methods, and ion-beam synthesis. In this section, we review these various growth methods and their ability to control nanostructure size and composition.

1.4.1 Growth of Nanostructured III-V Nitrides

One method of nitride nanostructure growth is colloidal growth. GaN colloidal nanostructures with an average diameter of ~3.0 nm have been produced, but have a large size distribution (± 40%). Additionally, the density of nanostructures must be kept very low to avoid agglomeration and the purity of the samples is reduced by incorporation of carbon at the surface.[20] Solution production techniques are capable of producing InN nanostructures ~3 nm in diameter, although they also suffer from agglomeration, forming clusters of nanoparticles ~30-40 nm in diameter.[25]

Nitride nanostructures have also been synthesized using solvo-thermal methods. There have been reports of GaN formation via reacting Li_3N with $GaCl_3$ in benzene at 280ºC (ref. 21) or reacting $Ga(C_6H_5N_2)_2)_3$ with $(CH_3)_3SiNHSi(CH_3)_3$ in toluene at 280ºC (ref. 22). InN nanostructures have been formed by reacting $InBr_3$ with NaN_3 in toluene at 280ºC (ref. 26). However, the product nanoparticles are either too large to exhibit quantum effects (InN: 1.9 nm, GaN: 2.8-11 nm, see Table 1.2) or suffer from

agglomeration of the nanostructures. Additionally, these reactions produce a large amount of byproduct and organic surface impurities.

Detonations of gallium azides offer a reproducible approach to phase-pure WZ nanocrystalline GaN.[27] In this process, $(R_3N)Ga(N_3)_3$, where R is Me, Et, or $Me_2C_8H_{17}$, is filled into a pressure vessel connected to a heating unit. The detonation is induced by rapid heating to 400°C and is detectable by a very sudden pressure rise up to three times the calculated end pressure. The vessel is then immediately cooled to room temperature. The energy of the detonation determines the size of the GaN crystallites. By varying the volume of $Ga(N_3)_3$, the donor ligand, and the starting pressure, samples with typical particle sizes of 2 nm up to 3000 nm can be obtained selectively. The resulting GaN nanostructures are encased in a C/H/N matrix arising from the organic ligand R_3N. This protects against agglomeration of the nanostructures, but introduces surface impurities.

GaN self-assembled nanostructures have been grown by low-pressure metal-organic chemical vapor deposition (MOCVD) under very low V/III ratios. The typical diameter and height of the quantum dots were 20 and 2 nm, respectively, with a density of ~5.0×10^{10} cm^{-2} (ref. 107). InGaN self-assembled quantum dots with strong PL emission were successfully grown in the SK mode, with average diameters of 8.4±0.5 nm.[23] The density of quantum dots could be reduced with an increase in growth temperature, although the quantum dot density could not be controlled independently of the quantum dot size, with a reduction in density corresponding to an increase in size. More recently, similarly-sized InGaN nanostructures have been grown with density ranging from 10^{10} to 10^8 cm^{-2}, inversely proportional to the density of screw dislocations in the buffer layer.[108] InN nanostructures have been produced by metal-organic vapor-

phase epitaxy (MOVPE), but these structures suffer from instabilities at ambient conditions, resulting in a gradual WZ to ZB phase transformation and the formation of group-III oxides.[109]

Molecular beam epitaxy (MBE) has also been used for the growth of GaN quantum dots on an AlN buffer layer. The nanostructures grow in the SK mode, with deposition of a wetting layer of about two MLs, followed by 3D islanding.[110] The resulting GaN nanostructures are typically ~15 nm in diameter and ~2 nm high. GaN/AlGaN nanocavities were successfully grown on Si(111) by MBE.[24] These heterostructures have an active region consisting of GaN quantum disks embedded in an AlGaN nanocolumn and cladded by AlN/GaN distributed Bragg reflectors. However, there is a lateral growth enhancement that leads to a large heterostructure geometrical distortion, crack formation, and poor control over nanostructure size. There have been several reports of InN thin film growth via MBE,[59,60,61] but to date, this method has not been used to produce zero-dimensional InN nanostructures.

Despite significant progress in the synthesis of III-N nanostructures using several growth methods, it is still a challenge to synthesize stable nanostructures with controlled size and shape uniformity in the 1-5 nm range. Additionally, in many cases, the nanostructures tend to agglomerate or suffer from surface impurities, making it difficult to study the optical properties from individual isolated nanostructures. Although MOCVD and MBE methods offer control over the composition of the nanostructures, these methods are limited by the need for lattice-matched substrates and are unable to produce nanostructures on the order of the Bohr exciton radius.

1.4.2 Ion-Beam Synthesis

Ion implantation is an increasingly popular technique for the synthesis of nanostructures due in part to the wide range of available implant and target species, as well as adjustable implantation ion doses and energies.[111] Using ion implantation techniques, a selected host material is irradiated with energetic ions that are accelerated from a few tens to a few thousand kilovolts. High-dose implantations can create supersaturations of the implanted ions in a layer extending from the specimen surface to depths up to hundreds of nanometers.[112] Subsequent thermal processing or further ion irradiation can induce the implanted material to precipitate as discrete nanoparticles.[113,114,115]

The versatility of the ion implantation technique arises from the fact that essentially any element in the periodic table can be implanted into virtually any host material. The large variety of ion/host combinations allows for a wide range of potential nanoparticle/host combinations. In principle, useful properties of two or more precipitated phases may be combined into a single well-defined, integrated structure. The important physical properties of the nanocomposite would then be optimized by adjusting the concentration and average size of the precipitates. The average precipitate size would be controlled by varying the concentration of implanted ions (e.g., by selecting the appropriate dose, dose rate, and energy), or by varying the annealing parameters.[111] However, to date, the implantation and annealing parameters required for specific precipitates are limited.

Nanocomposites formed by ion implantation can also be reliably reproduced due to the self-passivated interfaces between the nanocrystal surface and the host matrix.[111] Stability of the nanocrystal-matrix interface is not necessarily true of other production techniques. For example, InN nanostructures produced by metal-organic vapor-phase epitaxy (MOVPE) suffer from instabilities at ambient conditions, resulting in a gradual WZ to ZB phase transformation and the formation of group-III oxides.[109] Ion beams have been used to nucleate embedded WZ and ZB InN nanocrystals using N implantation into InP (ref. 65) and In and N co-implantation into Si,[64] but precipitation of InN nanostructures embedded in InAs have not been previously achieved. We will discuss the nucleation of both WZ and ZB InN in ion-implanted InAs in Chapter 3 of this thesis.

A particularly promising approach to producing naturally passivated nitride nanostructures is matrix-seeded growth, which involves ion-beam-amorphization of a semiconductor film, followed by annealing.[116] This process is illustrated in Fig. 1.1. A supersaturated-layer is produced by high-energy ion implantation (Fig. 1.1(a)), and annealing leads to nanocrystallization in the matrix (Fig. 1.1(b)). For example, GaN nanocrystals have been nucleated in an amorphous matrix using N-ion implantation into epitaxial-GaAs, followed by rapid-thermal-annealing (RTA).[117] Remarkably, these nanostructures exhibit significant near-infrared photoluminescence and cathodoluminescence,[117,118] indicating sufficient crystallinity for devices such as high-sensitivity photodetectors.[119] In this thesis, we will present an extension of this technique to InAs:N.

1.5 Directed Seeding of Nanostructures

In lasing applications, the zero-dimensional electronic density of states of QDs enhances the gain and reduces the temperature dependence of laser threshold. However, to achieve these theoretically predicted advantages, it is necessary to achieve a very dense (>5×10^{10}/cm^2) array of uniform QDs. Growth of In(Ga)As/(Al)GaAs and In(Ga)As/In(GaAs)P using the SK growth mode via MBE[120,121,122] and MOCVD,[123,124] and similar approaches exploring the Si/Ge material system[125] have been unable to produce dense ordered arrays of nanostructures. The randomness of nucleation and the size variation of the nanostructures cause a large spread in the electronic state energies, thereby limiting device performance.

Properties of colloidal QDs, such as narrow emission spectra tunable throughout the entire visible spectrum and high photoluminescence efficiencies, suggest the use of QD films in electroluminescent devices and pixilated full-color displays.[126] The use of QD monolayers has minimized the negative impact of QD charging and resistive power losses associated with poor QD-to-QD charge transport[127,128] characteristic of the earlier devices that utilized QD multilayers.[129] However, these advances highlight the need for a reproducible method for the formation of close-packed laterally patterned QD films, as would be needed in full-color pixilated structures.

In terms of lateral patterning of nanocrystals, focused ion beam (FIB) milling has been used to produce sites for selective nucleation of Ge islands on Si(001),[130] Cu_2O nanodots on $SrTiO_3$(100),[131] and InP nanowires on GaAs(100).[132] In addition, it has been proposed that FIB-induced vacancy motion would enable void organization in broad-area

implanted GaSb and InSb, although this has not been demonstrated.[133] In this thesis, we report the influence of combined broad-area and FIB irradiation, followed by RTA, on the phase selection and lateral patterning of nitride nanocrystals embedded in GaAs. Specifically, we present selected growth of ZB vs. WZ nitride nanocrystals in an embedded matrix, and show the influence of local increases in vacancy concentration on the spatial positioning of those nanocrystals.

1.6 Dissertation Objectives

The first part of this thesis work focuses on InN nanocrystal formation in N-implanted InAs. The influence of annealing temperature on the nucleation of zincblende and/or wurtzite structure was examined. We observe nucleation of zincblende InN following RTA at 550ºC. RTA at 600ºC leads to nucleation of both zincblende and wurtzite InN, with an increase in nanocrystal size in comparison to 550ºC anneals. This is the first report of ion-beam synthesis of InN in InAs. We propose a thermodynamic model for the nucleation of the zincblende phase that illustrates the key role of surface energy in the nucleation of InN nanocrystals.

The middle part of this thesis is devoted to investigations of the influence of post-implantation annealing on the structure of GaAs:N films. The role of annealing temperature and annealing time on the selective nucleation of zincblende and/or wurtzite GaN is examined. Through a comparison of our data with literature reports, we have developed a time-temperature-transformation diagram for the GaAs:N system to provide

a “roadmap” for the influence of annealing on the nucleation and structural development of GaN nanocrystals.

In the final part of this thesis, the demonstration of a new process for ordered nanostructuring, termed directed matrix-seeding, is described. In this technique, N ion implantation, FIB irradiation, and RTA are used to achieve laterally directed nucleation of GaN nanostructures. We identify the critical role of vacancy concentration on the spatially-directed nucleation of nanocrystals. We also apply a thermodynamic model for the nucleation of GaN that illustrates the key role of surface energy in the preferential nucleation of zincblende vs. wurtzite GaN.

1.7 Dissertation Organization

This dissertation is organized as follows. Chapter 2 describes the experimental procedures used for this thesis work, including ion implantation, transmission electron microscopy (TEM), channeling-Rutherford backscattering spectrometry (RBS), and focused ion beam (FIB). Details of TEM sample preparation are also presented.

In Chapter 3, the nucleation of InN nanocrystals in an amorphous InAs matrix is described. The influence of annealing temperature on the nanostructure of the implanted layer is studied by TEM and SAD. The size-distributions of the nucleated InN nanocrystals are discussed and a thermodynamic model for the nucleation of ZB vs. WZ InN for small nanocrystal radii is presented. Following implantation, a N-rich highly damaged surface layer is formed, with crystalline InAs remnants near the interface of the implanted layer and the near-substrate layer. For low annealing temperatures, nucleation

of polycrystalline InAs and ZB InN is observed. As the annealing temperature is increased, the nanocrystal size is increased and the nucleation of WZ InN is observed. A thermodynamic model for the minimization of free energy of InN nanocrystals is proposed. This model predicts the nucleation of the ZB phase for sufficiently small nucleates. The preference for the ZB phase for small radii is likely governed by a minimization of surface energy through adoption of the ZB phase, which has a higher density of low-energy surface planes.

Chapter 4 presents investigations of the influence of the energy and dose of the implanted ions, and the temperature and duration of post-implantation annealing, on the nucleation of GaN in N ion implanted GaAs. We compare the size distributions of nucleated GaN at several annealing temperatures with literature reports; for short annealing times (i.e. RTA), the maximum observed size at nucleation is smaller than the size required for WZ GaN nucleation. Furthermore, post-implantation RTA at 600 and 650ºC leads to the formation of polycrystalline GaAs and ZB GaN-rich nanocrystals, respectively. Longer anneals (i.e. FA) at 650ºC leads to the nucleation of wurtzite GaN. We capture these findings in a TTT diagram for the nucleation of ZB and WZ GaN in ion-implanted GaAs based on literature reports and work presented in this thesis.

In Chapter 5, we present a new method for spatially directing the nucleation of GaN in N ion-implanted GaAs. Using a combination of broad area implantation and FIB irradiation, we introduce laterally controlled damage regions which act as seeding locations for the formation of nanocrystalline GaN. We find that after annealing, a bilayer is formed with: (1) a surface layer with spatially directed nanostructures, and (2) a GaN-rich nanocrystalline layer. A comparison of implantation energies reveals a greater

selectivity in lateral ordering for the lowest energies due to the relative contribution of FIB-induced damage. We apply a thermodynamic model for GaN nucleation and find that ZB GaN is favored for sufficiently small nuclei. Finally in Chapter 6, we present a summary and an outline for future work.

Table 1.1 A comparison of the physical properties of AlN, GaN, and InN in both the ZB and WZ phases.

	AlN		GaN		InN	
	ZB	WZ	ZB	WZ	ZB	WZ
Band Gap Energy	5.94	6.2	3.2	3.39	0.58	0.65-0.8
Lattice Constant (Å)	a=4.12	a=3.111	a=4.520	a=3.189	a=0.498	a=3.538
		c=4.979		c=5.186		c=5.703
Density (gcm^{-3})	3.893	3.261	6.092	6.088	7.068	6.921

Table 1.2 Calculated exciton Bohr radii for selected semiconductors [71,72,73,74,75,134,135,136,137,138,139]

Semiconductor	Exciton Bohr Radius (nm)
Si	4.3
GaAs	15-16
InAs	30-34
GaN	2.8-11
InN	1.9
AlN	1.2

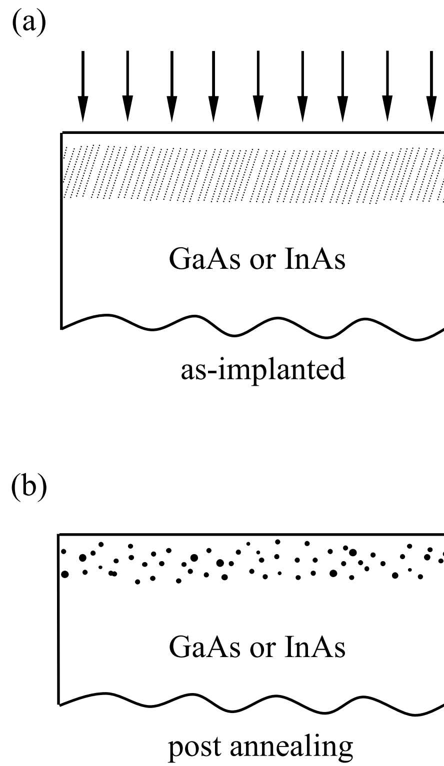

Fig. 1.1 Ion beam synthesis of nitride nanostructures. In (a), a high dose of nitrogen ions (5.0×10^{17} cm^{-2} at 100 keV) is implanted into an epitaxial GaAs film to produce a supersaturated "amorphous" layer. In (b), after thermal annealing, nano-scale crystallites form within the disordered matrix.

References

[1] M. R. Werner, and W. R. Fahrner, *IEEE Trans. Indust. Electron*. **48**, 249 (2001).

[2] P. L. Dreike, D. M. Fleetwood, D. B. King, D. C. Sprauer, and T. E. Zipperian, IEEE *Trans. Comp. Pack. Manufact. Technol.* **17**, 594 (1994).

[3] D. W. Palmer and R. C. Heckman, *IEEE Trans. Comp. Hybrids, Manuf. Technol*., **CHMT-1**, 333 (1978).

[4] T. E. Zipperian, *Proc. Power Conversion Intelligence*, 353 (1986).

[5] F. Magistrali, C. Tedesci, and E. Zanoni, *Semiconductor Device Reliability* (A. Christou and B. A. Unger, Eds.) p 211, 1990.

[6] M. Sokolich, K. K. Yu, M. Chiang, H. M. Le, and Y. C. Shih, Trans. *First. Int. High Temperature Electronics Conf.*, Albuquerque, NM, 302 (1991).

[7] S. Strite and H. Morkoc, *J. Vac. Sci. Technol. B* **10**, 1237 (1992).

[8] S. N. Mohammad, A. A. Salvador and H. Morkoc, *Proc. IEEE* **83**, 1306 (1995).

[9] H. Jeon, J. Ding, W. Patterson, A. V. Nurmikko, W. Xie, D. C. Grillo, M. Kobayashi, and R. L. Gunshor, *Appl. Phys. Lett.* **59,** 3619 (1991).

[10] M. Haase, J. Qiu, J. DePuydt, and H. Cheng, *Appl. Phys. Lett.* **59,** 1272 (1991).

[11] N. Nakayama, S. Itoh, K. Nakano, H. Okuyama, M. Ozawa, A. Ishibashi, M. Ikeda, and Y. Mori, *Electron. Lett.* **29,** 1488 (1993).

[12] A. Salokatve, H. Jeon, J. Ding, M. Hovinen, A. Nurmikko, D. C. Grillo, J. Han, H. Li, R. L. Gunshor, C. Hua, and N. Otsuka, *Electron. Lett.* **29,** 2192 (1993).

[13] S. Taniguchi, T. Hino, S. Itoh, K. Nakano, N. Nakayama, A. Ishibashi, and M. Ikeda, *Electron. Lett.* **32,** 552 (1996).

[14] S. Guha, H. Cheng, M. A. Haase, J. DePuydt, J. Qiu, B. J. Wu, G. E. and Hofler *Appl. Phys. Lett.* **63** 2723 (1994).

[15] G. C. Hua, N. Otsuka, D. C. Grillo, Y. Fan, J. Han, M. D. Ringle, R. L. Gunshor, M. Hovinen, and A. V. Nurmikko, *Appl. Phys. Lett.* **65** 1331 (1994).

[16] L. H. Kuo, L. Salamanca-Riba, B. J. Wu, J. M. DePuydt, G. M. Haugen, H. Cheng, S. Guha, and M. A. Haase. *Appl. Phys. Lett.* **65** 1230 (1994).

[17] A. Nurmikko and R. L. Gunshor, *Semicon. Sci. Technol.* **12**, 1337 (1997).

[18] L. F. Eastman, and U. K. Mishra, *Spectrum IEEE* **39**, 28 (2002).

[19] A. P. Zhang, F. Ren, T. J. Anderson, C. R. Abernathy, R. K. Singh, P. H. Holloway, S. J. Pearton, D. Palmer, and G. E. McGuire, *Crit. Rev. Sol. State Mater. Sci.* **27**, 1 (2001).

[20] O. I. Mićić, S. P. Ahrenkiel, D. Bertram, and A. J. Nozik, *Appl. Phys. Lett.* **75**, 478 (1999).

[21] Y. Xie, Y. Qian, W. Wang, S. Zhang, and Y. Zhang, *Science* **272**, 1926 (1996).

[22] K. Sardar, C. N. R. Rao, *Adv. Mater*. **16**, 425 (2004).

[23] K. Tachibana, T. Someya, and Y. Arakawa, *Appl. Phys. Lett*. **74**, 383 (1999).

[24] J. Ristić, E. Calleja, A. Trampert, S. Fernández-Garrido, C. Rvera, U. Jahn, and K. H. Ploog, *Phys. Rev. Lett.* **94**, 146102 (2005).

[25] M. R. Greenberg, G. A. Smolyakov, J. C. Jones, S. D. Bunge, T. J. Boyle, and M. Osinski, "Synthesis and Characterization of InP and InN Colloidal Nanocrystals," in *Conference on Lasers and Electro-Optics/Quantum Electronics and Laser Science Conference and Photonic Applications Systems Technologies*, Technical Digest (CD) (Optical Society of America, 2006), paper CTuN5.

[26] J. Choi, and E. G. Gillan, *J. Mater. Chem*. **16**, 3774 (2006).

[27] A. C. Frank, R. A. Fischer, *Adv. Mater*. **10**, 961 (1998).

[28] W. Y. Ching, and B. N. Harmon, *Phys. Rev. B* **34**, 5305 (1986).

[29] I. Gorczyca and N. E. Christensen, *Solid State Commun*. **80**, 335 (1991).

[30] M. Leszczynski, in *Properties, Processing and Applications of Gallium Nitride and Related Semiconductors*, edited by J. H. Edgar, S. T. Strite, I. Akasaki, H. Amano, and C. Wetzel (INSPEC, London, UK, 1999), p.3.

[31] M. J. Paisley and R. F. Davis, *J. Cryst. Growth* **127**, 136 (1993).

[32] S. Strite, et al., *J. Cryst. Growth* **127**, 204 (1993).

[33] M. J. Paisley, Z. Sitar, J. B. Posthill, and R. F. Davis, *J. Vac. Sci. Technol. A* **7**, 701 (1989).

[34] S. Dhara, P. Magudapathy, R. Kesavamoorthy, S. Kalavathi, K.G.M. Nair, G.M. Hsu, L.C. Chen, K.H. Chen, K. Santhakumar, and T. Soga, *Appl. Phys. Lett*. **87**, 261915 (2005).

[35] V. Yu. Davidov, A. A. Klochikhin, V. V. Emtsev, S. V. Ivanov, V. V. Vekshin, F. Bechstedt, J. Furthmüller, H. Harima, A. V. Mudryi, A. HAsimoto, A. Yamamoto, J. Aderhold, J. Graul, and E. E. Haller, *Phys. Stat. Sol. B* **230**, R4 (2002).

[36] J. Wu, W. Walukiewicz, K. M. Yu, J. W. Ager III, E. E. Haller, H. Lu, W. J. Schaff, Y. Saito, and Y. Ninishi, *Appl. Phys. Lett.* **80**, 3967 (2002).

[37] K.C. Lo, H.P. Ho, K.Y. Fu, P.K. Chu, K.F. Li, and K.W. Cheah, *J. Appl. Phys*. **95**, 8178 (2004).

[38] Y.G. Li, A.T.S. Wee, C.H.A. Huan, and J.C. Zheng, *Appl. Surf. Sci*. **174**, 275 (2001).

[39] S. Nakamura and G. Fasol, "The Blue Laser Diode", (Springer Verlag, Berlin, 1997).

[40] S. Nakamura, Mater. *Res. Soc. Symp. Proc.* **482**, 1145 (1998).

[41] O. Jani, I. Ferguson, C. Honsberg, and S. Kurtz, *Appl. Phys. Lett*. **91**, 132117 (2007).

[42] J. Hu, L. Yang, and M. W. Shin, *J. Phys. D: Appl. Phys*. **41**, 035107 (2008).

[43] G. Zorpette, *Spectrum IEEE* **39**, 70 (2002).

[44] J. J. Wierer, Jr., D. Aurelien, and M. M. Megens, *Nature Photonics* **3**, 136 (2009).

[45] M. T. Hardy, D. F. Feezell, S. P. DenBaars, and S. Nakamura, *Mat. Today* **14**, 408 (2011).

[46] G. Ramírez-Flores, H. Navarro-Contreras, A. Lastras-Martínez, R. C. Powell, and J. E. Greene, *Phys. Rev. B* **50**, 8433 (1994).

[47] Z. Sitar, M. J. Paisley, J. Ruan, J. W. Choyke, and R. F. Davis, *J. Mater. Sci. Lett.* **11**, 261 (1992).

[48] P. Das and D. K. Ferry, *Solid-State Electron.* **19**, 851 (1976).

[49] H.J. Kim, T.G. Andersson, J.-M. Chauveau, and A. Trampert, *J. Appl. Phys*. **94**, 7193 (2003).

[50] H.J. Kim, T.G. Andersson, J.-M. Chauveau, and A. Trampert, *Appl. Phys. Lett*. **81**, 3407 (2002).

[51] N. F. Gardner, J. C. Kim, J. J. Wierer, Y. C. Shen, and M. R. Krames, *Appl. Phys. Lett*. **86**, 111101 (2005).

[52] Z. L. Wang, *Adv. Mater*. **19**, 889 (2007).

[53] B. Monemar, *J. Mat. Sci. Mater. Electr.* **10**, 227 (1999).

---

[54] V. Yu. Davydov, A. A. Klochikhin, V. V. Emtsev, S. V. Ivanov, V. V. Vekshin, F. Bechstedt, J. Furthmüller, H. Harima, A. V. Mudryi, A. Hashimoto, A. Yamamoto, J. Aderhold, J. Graul, and E. E. Haller, *Phys. Stat. Sol. B* **230**, R4 (2002).

[55] J. Wu, W. Walukiewicz, K. M. Yu, J. W. Ager III, E. E. Haller, H. Lu, W. J. Schaff, Y. Saito, and Y. Nanishi, *Appl. Phys. Lett*. **80**, 3967 (2002).

[56] N. Puychevrier and M. Menoret, *Thin Solid Films* **36**, 141 (1976).

[57] K. L. Westra and M. J. Brett, *Thin Solid Films* **192**, 227 (1990).

[58] F. Bechstedt, J. Furthmüller, M. Ferhat, L. K. Teles, L. M. R. Scolfaro, J. R. Leite, V. Yu. Davydov, O. Ambacher, and R. Goldhahn, *Phys. Stat. Sol. (a)* **195**, 628 (2003).

[59] C. L. Hsiao, T. W. Liu, C. T. Wu, H. C. Hsu, G. M. Hsu, L. C. Chen, W. Y. Shiao, C. C. Yang, A. Gällström, P. O. Holtz, C. C. Chen, and K. H. Chen, *Appl. Phys. Lett*. **92** 111914 (2008).

[60] J. G. Lozano, F. M. Morales, R. García, D. González, V. Lebedev, Ch. Y. Wang, V. Cimalla, and O. Ambacher, *Appl. Phys. Lett*. **90**, 091901 (2007).

[61] X. Xu, P. Specht, R. Armitage, J. C. Ho, E. R. Weber, and C. Kisielowski, *Appl. Phys. Lett*. **87**, 092102 (2005).

[62] C. Nie, R. Zhang, Z. L. Xie, X. Q. Xiu, B. Liu, D. Y. Fu, Q. J. Liu, P. Han, S. L. Gu, Y. Shi, and Y. D. Zheng, *Chin. Phys. Lett.* **25**, 1780 (2008).

[63] D. González, J. G. Lozano, M. Herrera, N. D. Browning, S. Ruffenach, O. Briot, and R. García, *J. Appl. Phys*. **105**, 013527 (2009).

[64] Y. K. Huang, C. P. Liu, Y. L. Lai, C. Y. Wang, Y. F. Lai, and H. C. Chung, *Appl. Phys. Lett.* **91**, 091921 (2007).

---

[65] K. Santhakumar, R. Kesavamoorthy, K. G. M. Nair, P. Jayavel, D. Kanjilal, V. Sankara Sastry, and V. Ravichandran, *Nucl. Inst. Meth. Phys. Res. B* **212**, 521 (2003).

[66] A. P. Alivisatos, *Science* **271**, 933 (1996).

[67] R. Eisberg and R. Resnick, *Quantum physics of atoms, molecules, solids, nuclei, and particles* (John Wiley & Sons, Inc., New York, 1985).

[68] X.-Q. Shen, S. Tanaka, S. Iwai, and Y. Aoyagi, *Appl. Phys. Lett.* **72**, 344 (1998).

[69] C. Adelmann, J. Simon, G. Feuillet, N. T. Pelekanos, B. Daudin, and G. Fishman, *Appl. Phys. Lett.* **76**, 1570 (2000).

[70] F. Widmann, J. Simon, B. Daudin, G. Feuillet, J. L. Rouvière, N. T. Pelekanos, and G. Fishman, *Phys. Rev. B* **58**, 15989 (1998).

[71] G. Bastard, E. E. Mendez, L. L. Chang, and L. Esaki, *Phys. Rev. B* **26**, 1974 (1982).

[72] A. C. Ford, J. C. Ho, Y. –L. Chueh, Y. –C. Tseng, Z. Fan, J. Guo, J. Bokor, and A. Javey, *Nanoletters* **9**, 360 (2009).

[73] P. Ramvall, S. Tanaka, S. Nomura, P. Riblet, and Y. Aoyagi, *Appl. Phys. Lett*. **73**, 1104 (1998).

[74] J. Zhang, L. D. Zhang, X. F. Wang, C. H. Liang, and X. S. Peng, *J. Chem. Phys*. **115**, 5714 (2001).

[75] S. Chichibu, T. Azuhata, T. Sota, and S. Nakamura, *Appl. Phys. Lett*. **69**, 4188 (1996).

[76] J. Tersoff, *Phys. Rev. Lett.* **81**, 3183 (1998).

[77] J. Tersoff and F. K. LeGoues, *Phys. Rev. Lett*. **72**, 3570 (1994).

[78] S. Naritsuka, T. Kondo, H. Otsubo, K. Saitoh, Y. Yamamoto, and T. Maruyama, *J. Cryst. Growth* **300**, 118 (2007).

[79] T. Kondo, K. Saitoh, Y. Yamamoto, T. Maruyama, and S. Naritsuka, *Phys. Stat. Sol. A* **203**, 1700 (2006).

[80] T. Maruyama, H. Otsubo, T. Kondo, Y. Yamamoto, and S. Naritsuka, *J. Cryst. Growth* **301-302**, 486 (2007).

[81] A. S. Özcan, Y. Wang, G. Ozaydin, K. F. Ludwig, A. Bhattacharyya, T. D. Moustakas, and D. P. Siddons, *J. Appl. Phys*. **100**, 084307 (2006).

[82] M. Nirmal, B. Dabbousi, M. Bawendi, J. Macklin, J. Trautman, T. Harris, and L. Brus, *Nature* **383**, 802 (1996).

[83] P. Fransuzov, M. Kuno, B. Jankó, and R. A. Marcus, *Nat. Phys*. **4**, 519 (2008).

[84] T. D. Krauss, and J. J. Peterson, *J. Phys. Chem. Lett.* **1**, 1377 (2010).

[85] K. T. Shimizu, R. G. Neuhauser, C. A. Leatherdale, S. A. Empedocles, W. K. Woo, and M. G. Bawendi, *Phys. Rev. B*. **63**, 2053161 (2001).

[86] P. A. Frantsuzov, S. Volkán-Kacsó, and B. Jankó*, Phys. Rev. Lett.* **103,** 207402 (2009).

[87] G. Margolin, V. Protasenko, M. Kuno, and E. Barkai, *J. Phys. Chem. B* **110**, 19053 (2006).

[88] Y. Fu, J. Zhang, and J. R. Lakowicz, *Chem. Phys. Lett.* **447**, 96 (2007).

[89] A. W. Wood, X. Weng, Y. Q. Wang, and R. S. Goldman, *Appl. Phys. Lett*. **99**, 093108 (2011).

[90] X. Weng, S. J. Clarke, W. Ye, S. Kumar, A. Daniel, R. Clake, J. Holt, J. Sipowska, A. Francis, V. Rotberg, and R. S. Goldman, *J. Appl. Phys*. **92**, 4012 (2002).

[91] G. S. Nolas and H. J. Goldsmid, *Thermal Conductivity: Theory, Properties, and Applications*, T. M. Tritt, Ed., Kluwer Academic/Plenum, New York, 2004, p. 106.

[92] G. D. Mahan and J. O. Sofo, *Proc. Natl. Acad. Sci. U.S.A.* **93**, 7436 (1996).

[93] M. S. Dresselhaus, G. Chen, M. Y. Tang, R. Yang, H. Lee, D. Wang, Z. Ren, J. P. Fleurial, and P. Gogna, *Adv. Mater.* **19**, 1043 (2007).

[94] L. D. Hicks and M. S. Dresselhaus, *Phys. Rev. B* **47**, 12727 (1993).

[95] L. D. Hicks and M. S. Dresselhaus, *Phys. Rev. B* **47**, 16631 (1993).

[96] L.D. Hicks, T.C. Harman, X. Sun, and M.S. Dresselhaus, *Phys. Rev. B* **53**, R10493 (1996).

[97] S.V. Faleev and F. Léonard, *Phys. Rev. B* **77**, 214304 (2008).

[98] M. Zebarjadi, K. Esfarjani, A. Shakouri, J. –H. Bahk, Z. Bian, G. Zeng, J. Bowers, H. Lu, J. Zide, and A. Gossard, *Appl. Phys. Lett.* **95**, 202105 (2009).

[99] A. Yadav, K. Pipe, W. Ye, and R. S. Goldman, *J. Appl. Phys.* **105**, 093711 (2009).

[100] V. M. Fomin, and P. Kratzer, *Phys. Rev. B* **82**, 045318 (2010).

[101] R. Venkatasubramanian, E. Siivola, T. Colpitts, and B. O'Quinn, *Nature* **413**, 597-602 (2001).

[102] A. I. Boukai, Y. Bunimovich, J. Tahir-Kheli, J. K. Yu, W. A. Goddard III, and J. R. Heath, *Nature* **451**, 168 (2008).

[103] R. Srinivasan and K. Ramachandran, *Cryst. Res. Technol.* **43**, 953 (2008).

[104] M. Zebarjadi, K. Esfarjani, Z. Bian, A. Shakouri, *Nano Lett.* **11**, 225 (2011).

[105] A. A. Balandin, O. L. Lazarenkova, *Appl. Phys. Lett.* **82**, 415 (2003).

[106] A. Yadav, K. P. Pipe, W. Ye, and R. S. Goldman, *J. Appl. Phys.* **105**, 093711 (2009).

[107] M. Miyamura, K. Tachibana, and Y. Arakawa, *Appl. Phys. Lett*. **80**, 3937 (2002).

[108] S. C. Davies, D. J. Mowbray, Q. Wang, F. Ranalli, and T. Wang, *Appl. Phys. Lett.* **95**, 101909 (2009).

[109] D. González, J. G. Lozano, M. Herrera, N. D. Browning, S. Ruffenach, O. Briot, and R. García, *J. Appl. Phys*. **105**, 013527 (2009).

[110] B. Daudin, F. Widmann, G. Feuillet, C. Adelmann, Y. Samson, M. Arlery, and J. L. Rouviere, *Mater. Sci. Eng. B,* **50**, 8 (1997).

[111] A. Meldrum, R. F. Haglund, Jr., L. A. Boatner, and C. W. White, *Adv. Mater*. **13**, 1431 (2001).

[112] E. Rimini, "Ion implantation: basics to device fabrication" (Kluwer Acad. Pub. Boston, MA, 1995).

[113] C. W. White, A. Meldrum, J. D. Budai, S. P. Withrow, E. Sonder, R. A. Zuhr, D. M. Hembree, M. Wu, D. O. Henderson, *Nucl. Instrum. Methods B* **148**, 991 (1999).

[114] K. H. Heinig, B. Schmidt, A. Markwitz, R. Grötzschel, M. Strobel, S. Oswald, *Nucl. Instrum. Methods B* **148**, 969 (1999).

[115] T. Shimizu-Iwayama, M. Oshima, T. Niimi, S. Nakao, K. Saitoh, T. Fujita, N. Itoh, *J. Phys.: Condens. Matter* **5**, 375 (1993).

[116] X. Weng, W. Ye, S. J. Clarke, R. S. Goldman, V. Rotberg, A. Daniel, and R. Clarke, *J. Appl. Phys*. **97**, 064301 (2005).

[117] X. Weng, S. J. Clarke, W. Ye, S. Kumar, A. Daniel, R. Clake, J. Holt, J. Sipowska, A. Francis, V. Rotberg, and R. S. Goldman, *J. Appl. Phys*. **92**, 4012 (2002).

[118] X. Weng, R. S. Goldman, V. Rotberg, N. Bataiev, and L. J. Brillson, *Appl. Phys. Lett.* **85**, 2774 (2004).

---

[119] M. Mikulics, M. Marso, P. Kordos, S. Stancek, P. Kovac, X. Zheng, S. Wu, and R. Sobolewski, *Appl. Phys. Lett.* **83**, 1719 (2003).

[120] Q. Xie, A. Madhukar, P. Chen, and N. P. Kobayashi, *Phys. Rev. Lett.* **75**, 2542 (1995).

[121] W. Zhou, B. Xu, H. Z. Xu, F. Q. Liu, J. B. Liang, Z. G. Wang, Z. Z. Zhu, and G. H. Li, *J. Electron. Mater.* **28**, 528 (1999).

[122] D. L. Huffaker, G. Park, Z. Zou, O. B. Shchekin, and D. G. Deppe, *Appl. Phys. Lett.* **73**, 2564 (1998).

[123] F. Heinrichsdorff, A. Krost, N. Kirstaedter, M. Mao, M. Grundmann, D. Bimberg, A. O. Kosogov, and P. Werner, *Jpn. J. Appl. Phys.*, Part 1 **36**, 1129 (1995).

[124] F. Heinrichdorff, M. H. Mao, N. Kirstaedter, A. Krost, and D. M. Bimberg, *Appl. Phys. Lett.* **71**, 22 (1997).

[125] D. J. Eaglesham and M. Cerullo, *Phys. Rev. Lett.* **64**, 1943 (1990).

[126] L. A. Kim, P. O. Anikeeva, S. A. Coe-Sullivan, J. S. Steckel, M. G. Bawendi, and V. Bulovic, *Nanoletters* **8**, 4513 (2008).

[127] C. A. Leatherdale, C. R. Kagan, N. Y. Morgan, S. A. Empedocles, M. A. Kastner, M. G. Bawendi, *Phys. Rev. B* **62**, 2669 (2000).

[128] D. S. Ginger, N. C. Greenham, *J. Appl. Phys.* **87**, 1361 (2000).

[129] Schlamp, M. C.; Peng, X.; Alivisatos, A. P. *J. Appl. Phys.* **82**,5837 (1997).

[130] A. Portavoce, R. Hull, M. C. Reuter, F. M. Ross, *Appl. Phys. Lett*. **82**, 1093 (2003).

[131] J.F. Groves, Y. Du, I. Lyubinetsky, D.R. Baer, *Superlattices and Microstructures* **44** (4-5), 677-685 (2008)

[132] J. Ahopelto, H. Lezec and Y. Ochiai, A. Usui, H. Sakaki, *Appl. Phys. Lett*. **64**, 499 (1994)

[133] N. Nitta, M. Taniwaki, *Nuc. Inst. Meth. Phys. Res. B* **206,** 482-485 (2003).

[134] A. Meldrum, R. F. Haglund, Jr., L. A. Boatner, and C. W. White, *Adv. Mater*. **13**, 1431 (2001).

[135] A. D. Yoffe, *Adv. Phys.* **42**, 173 (1993).

[136] E. A. Davis, S. F. J. Cox, R. L. Lichti, and C. G. Van de Walle, *Appl. Phys. Lett*. **82**, 592 (2003).

[137] G. Tränkle, H. Leier, A. Forchel, H. Haug, C. Ell, and G. Weimann, *Phys. Rev. Lett*. **58**, 419 (1987).

[138] R. C. Miller, D. A. Kleinman, W. T. Tsang, and A. C. Gossard, *Phys. Rev. B* **24**, 1134 (1981).

[139] G. Steude, B. K. Meyer, A. Göldner, A. Hoffmann, F. Bertram, J. Christen, H. Amano, and I. Akasaki, *Appl. Phys. Lett.* **74**, 2456 (1999).

Chapter 2

Experimental Procedures

2.1 Overview

This chapter describes the experimental procedures used for the synthesis and characterization of the nanostructures studied in this thesis. For these experiments, epitaxial GaAs (InAs) films grown on (001) GaAs (InAs) were broad-area irradiated N^+ ions. Following broad-area irradiation, the samples were furnace annealed (FA) flowing N_2 atmosphere, or rapid thermal annealed in Ar gas. Plan-view TEM samples were prepared using mechanical polishing and chemical etching. Cross-sectional TEM specimens were prepared using conventional mechanical polishing. TEM imaging and electron diffraction were carried out in a JEOL 3011 operating at 300 kV. XEDS mapping was performed in a JEOL 2010 TEM operating at 200 kV.

For directed matrix seeding experiments, trenches were milled into the surface of selected samples using an FEI Nova Nanolab Dualbeam FIB operating at 30 keV. Cross-sectional TEM samples oriented perpendicular to the length of the FIB-milled trenches were prepared using FIB liftout techniques.[1] TEM imaging and diffraction were carried out in a JEOL 2010F TEM operating at 200kV.

2.2 Broad-Area Ion Implantation

The GaAsN and InAsN nanostructures described in this dissertation were synthesized using N ion implantation in GaAs or InAs, respectively, followed by rapid thermal annealing (RTA) or furnace annealing (FA). The 100 keV 300ºC ion implantation experiments were performed at the Michigan Ion Beam Laboratory (MIBL), using a Varian CF3000 200 keV ion implanter and the 75 keV (300 ºC) and 77 K ion implantations were performed at Los Alamos National Laboratory by Dr. Yongqiang Wang.

Figure. 2.1 presents a schematic of the broad-area ion implanters used in these studies. The major components are the ion source, a mass separation system, the accelerating column, and a scanning system.[2] The ion source contains the species to be implanted and an ionizing system to ionize the species. In the case of nitrogen, a plasma is created with high-purity nitrogen gas which is ionized by electrons thermally emitted from tungsten filaments. Ions are extracted from the source by a small accelerating voltage and then accelerated into the mass separation system. Here, a spatial separation of ions subjected to the Lorentz force occurs due to differences in their masses and charges. The desired ion species are separated from the other species, such as residual air, hydrocarbons from vacuum pumps, and other impurities, which are removed. The ion beam is then directed into the accelerating column and accelerated by a static electric field. Since the target area to be implanted is often larger than the ion beam size, it is necessary to scan the ion beam over the whole implantation area. This is realized by electrostatic fields between the X-Y deflector plates. At the target, the ion beam finally

impinges on the wafer. The ion implanter at Los Alamos is capable of cooling down or heating up the target over a wide range of temperatures.

For all samples discussed in this thesis, implantation into ~1 µm thick GaAs or InAs films (Si-doped) grown by molecular-beam epitaxy on (001) GaAs and InAs, respectively, was performed. The films were implanted with 100 keV nitrogen ions at a fluence of 5.0×10^{17} cm^{-2} or 75 keV at a fluence of 2.5×10^{17} cm^{-2}. To minimize channeling, a ~7° ion beam angle of incidence with respect to the sample surface normal was utilized. During implantation, the substrate temperature was maintained at 300°C and 77 K for GaAs and InAs, respectively, as determined by a J-type thermocouple attached to the back of the sample holder.

2.3 Thermal Annealing

FA experiments described in this thesis were carried out using a Lindberg/Blue quartz tube furnace. The RTA experiments were carried out using a JetFirst – 150 RTA system at the Solid-State Electronic Laboratory (SSEL) of Electrical Engineering and Computer Science Department in the University of Michigan.

A schematic of the FA system is shown in Fig. 2.2. During FA, the sample is placed between two GaAs anneal caps and held on a quartz sample boat. The boat is then loaded into a quartz tube equipped with a gas inlet and placed inside the furnace. A gas line is connected and ambient gas pressure is adjusted externally. The sample can be heated to a maximum of 1100°C, monitored using a thermocouple mounted outside the quartz tube under the sample, and another inserted into the quartz tube ~ 2 cm from the

sample. Implanted-plus-FA samples used in this thesis were annealed in flowing nitrogen gas at 500-750°C for 10 min.

Figure 2.3 presents a diagram of the RTA system. During RTA, the sample is supported on a Si wafer held on thin quartz pins in thermal isolation inside a cell containing a controllable gas ambient. A tungsten-halogen lamp heats the sample through transparent windows coupled with highly reflective mirrors. The sample can be heated to ~1000°C for a time interval of 1-20 s. RTA samples in this thesis were annealed in flowing Ar gas at 500-900°C for 30 s.

2.4 Transmission Electron Microscopy Sample Preparation

Both plan-view and cross-sectional TEM were used to examine the microstructure of GaAsN and InAsN nanostructures. Plan-view TEM samples were prepared by chemical etching from the backside (substrate side), and cross-sectional samples were prepared using mechanical polishing or FIB lift-out. All three TEM sample preparation methods are described below.

2.4.1 Chemical Etching (Plan-view)

Figure 2.4 presents a schematic of the chemical etching process for preparing plan-view TEM samples. For chemical etching, the samples were cleaved into ~3 x 3 mm squares and polished to ~200 μm with 600 grit silicon carbide paper (from South Bay Technology Inc.) from the backside. Each sample was then mounted epilayer-side

down on a glass slide using Crystalbond^{TM} from Electron Microscopy Sciences. Next, the backside of the sample was covered with a layer of Crystalbond^{TM}. Small holes with a diameter of ~0.5 mm were melted into the wax using a Weller 12 W soldering iron powered through a Variac adjusted to 20% power. Finally, the glass slide was immersed in NH_4OH/H_2O_2 (4:1) solution to etch the GaAs substrate until perforation through the epilayer was visible under 10x optical magnification. Continued etching following perforation resulted in overetching, in which the etchant leaked through the perforation and eroded the surface layer. Figure 2.5(a) presents an optical microscope view of an etched sample with a well-defined edge of the perforation, indicating that the surface layer has not been etched. In Fig. 2.5(b), the etchant has begun to erode the surface layer, evidenced by the jagged perforation edge and extensive surface discoloration.

2.4.2 Mechanical Polishing (Cross-section)

Cross-sectional TEM (XTEM) samples were prepared by mechanical polishing followed by Ar ion milling at 77K, as shown schematically in Fig. 2.6. For these samples, two pieces of ~1.5 x 3 mm were glued together epilayer side to epilayer side using Epoxy Technology H22 silver epoxy. This epoxy is a mixture of the silver-filled resin (H22 part A) and a small amount of hardener (H22 part B). Teflon tape was used to wrap the sample preparation surface to prevent the sample epoxy from curing on the heated surface. The epoxied samples were cured for 30 minutes at 150°C on a hot plate. Such a low curing temperature was chosen in order to avoid any additional sample annealing. After cooling in air, the samples were mechanically polished in cross-section

using 600, 800 and 1000 grit SiC papers in sequence. Following polishing of one side, the sample was mounted polished side down on a 3 mm diameter slotted Mo grid (with a slot size of 1 x 2 mm) using the silver epoxy and curing process described above. The sample was then mechanically polished on the reverse side using the process described above until the sample reached a thickness of 75-100 μm, as determined with a Mitutoyo upright dial gauge. Finally, the samples were ion milled to perforation using a Gatan ion miller. To minimize ion damage during milling, the samples were cooled to 77 K and low angles of incidence (3-5°) and low beam energies (3-5 kV) were used.

2.4.3 FIB lift-out (Cross-section)

FIB lift-out samples were prepared using an FEI Nova 200 Nanobeam and FEI Quanta 3D. Schematics of the 9 steps of the FIB lift-out process are presented in Figs. 2.7(a-i). We start by thinning ~2 μm wide membrane with a 30 keV, 5.0 nA ion beam. The current and voltage are gradually reduced as the membrane is thinned to a final width of 50-120 nm. The steps are as follows:

First, using the SEM imaging capabilities of the Nova and/or the Quanta, the area of interest was located, as shown in Fig. 2.7(a). Then, the area of interest was coated with e-beam-deposited Pt (~200 nm) to prevent milling or multiple image scans from damaging the surface of the cross-sectional TEM specimen (Fig. 2.7(b)). On both sides of the Pt, leaving a 2 μm wide membrane of material in the center, two trenches were milled. The two trenches were approximately 20 μm wide, 14 μm long, and 10 to 15 μm deep (Fig. 2.7(c)). This material removal step is typically performed at 30 keV, 5.0 nA.

A lower beam current, typically 1.0 nA, is used to further thin the membrane to ~1 μm (Fig. 2.7(d)). Next, the entire sample is tilted to 45 to 60°. Two vertical and one horizontal cuts are made through the membrane, framing the area of interest, as shown in Fig. 2.7(e). The vertical cuts stop short of the sample surface to provide structural strength and stability to the membrane. The beam current and energy are reduced to 10 kV and 0.12 nA, and the membrane is ion polished on both sides to a nominal thickness of approximately 0.3 μm. A tungsten needle is then brought into contact with the membrane and a layer of e-beam-deposited Pt is used to secure the tip of the needle to the membrane (Fig. 2.7(f)). The material in the top two corners of the membrane holding it to the sample are then milled away, leaving the membrane on the tip of the needle (Fig. 2.7(g)). The sample is then moved to a copper TEM lift-out sample half-grid and attached using e-beam-deposited Pt (Fig. 2.7(h)). The Pt connection between the membrane and the tungsten needle tip is then severed using the FIB beam, leaving the cross-sectional sample mounted on the TEM grid as shown in Fig. 2.7(i). Finally, the sample is polished again, with beam energy and current of 10 kV and 50 pA, bringing the membrane to a thickness of 50 to 120 nm.

2.5 Transmission Electron Microscopy

To study the evolution of the GaAs:N and InAs:N microstructures, transmission electron microscopy (TEM) was utilized on both GaAsN and InAsN nanostructures. We used diffraction contrast imaging and high-resolution TEM (HRTEM), which are

described below. All TEM experiments were conducted at the Michigan Electron Microbeam Analysis Laboratory (EMAL), using JEOL 3011 and 2010F microscopes.

Conventional diffraction contrast TEM imaging was conducted using a JEOL 3011 or 2010FX transmission electron microscope operating at 300 and 200 keV, respectively. The microscope was often aligned in dark-field mode, in which only one set of diffracted beams is used for imaging. A schematic of the dark-field alignment is shown in Fig. 2.8. The objective aperture was then inserted to select the direct beam (000) to form bright field (BF) images or select the diffracted beam (hkl) to form dark field (DF) images. The contrast of the images is therefore produced by differences in intensities of electrons scattered into the diffracted beam from various parts of the sample and is consequently called "diffraction contrast". The typical diffraction planes used for imaging were the {220} reflections of GaAs (InAs), but {111} GaN (InN) reflections were also used. A detailed description of diffraction analysis techniques is presented in Appendix A.

To obtain HRTEM images, the sample was tilted so that the incident beam was aligned along the <110> zone axis. The objective aperture was then inserted and positioned to select multiple beams to form the HRTEM images. The contrast of the images is called "phase contrast", which is due to the fact that the electrons leaving the bottom of the sample have small phase differences arising from scattering inside the sample. The images were captured with Gatan Digital Micrograph through a CCD camera.

2.6 X-Ray Energy Dispersive Spectroscopy

The chemical composition of implanted and annealed samples was examined qualitatively by X-Ray Energy Dispersive Spectroscopy (XEDS), in a JEOL 2010 TEM operating at 200 keV. During electron beam irradiation, incident electrons may eject inner-shell electrons from the sample. An outer-shell electron may subsequently relax to the lower-energy state and emit an X-ray with energy equal to this difference in electronic energy levels. Thus, the emitted X-ray is characteristic of the unique atomic structure of the excited atom, and the number of X-rays emitted in a given scan time related to the concentration of that element in the sample. In this case, a Si(Li) diode under reverse bias was used to detect the energies of emitted X-rays.

To determine the chemical composition as a function of depth, we assume a uniform thickness of the sample in the vicinity of the XEDS measurement. The atomic percentages of each element C_A and C_B can be related to the measured intensities (I_A, I_B) by the Cliff-Lorimer equation,[3]

$$\frac{C_A}{C_B} = k_{AB} \frac{I_A}{I_B} \tag{2.1}$$

where k_{AB} is the Cliff-Lorimer factor. To calculate k_{AB}, we use XEDS data collected in regions of pure InAs, typically at 250-300 nm depths below the surface. Once k_{AB} is calculated, the measured ratio of I_A/I_B in the nanostructured regions can be used to calculate the relative atomic percentages of each element, C_A and C_B.

2.7 Channeling Rutherford Backscattering Spectrometry

Channeling-Rutherford backscattering spectrometry (RBS) was utilized to determine the depth-dependence of lattice disorder in as-implanted and post-annealing samples. In this technique, a collimated beam of charged particles (in our case, 2 MeV He++, i.e. α-particles) is directed at the sample surface. Backscattered particles were detected by a solid-state particle detector subtending a solid angle $\Omega \approx 5$ mili-steradians, as shown in Fig. 2.9. The total number of detected ions, or yield, was measured by a charge integrator connected to a 300 μm-thick B-implanted silicon charged-particle detector (ULTRA series, Ortec9). A Faraday cup was used near the sample to generate an electric field, preventing spurious charge counts from sputtered electrons at the sample surface.

In the channeling condition, the sample is aligned so that the incident beam is parallel to a channel in the crystal, as shown in Fig. 2.10(a). The particle is steered through a row of atoms in a crystalline lattice by undergoing only small-angle scattering within the channel. Rutherford scattering occurs when the incident positively-charged particle undergoes large-angle scattering from Coulomb repulsion from atomic nuclei of the sample atoms. Thus, some fraction of the particles will be dechanneled due to lattice defects, impurities, strain fields, and thermal vibrations. An example of a particle/lattice-defect interaction that results in dechanneling is shown schematically in Fig. 2.10(b) for point defects.

The energy of the backscattered particle is characteristic of the target atom that it collides with. Assuming an elastic collision, the ratio of incoming and outgoing projectile energies is dependent only on the masses of the particle and target atom and the angle of collision. This ratio is defined as the kinematic factor K:

$$K = \frac{E_1}{E_0} = \left[\frac{(M_2^2 - M_1^2(\sin\theta)^2)^{1/2} + M_1 \cos\theta}{M_1 + M_2} \right] \tag{2.2}$$

where M_1 and M_2 are the projectile and target atom masses, E_1 and E_0 are outgoing and incoming projectile energies, and θ is the scattering angle. Since the atomic weights of Ga and As are similar (Z = 31 and 33, respectively), the energy difference of α-particles backscattered by Ga versus As is expected to be negligible. Thus, the profile represents an average damage depth profile from backscattering from either Ga or As.

In RBS, the yield Y of the backscattered α-particles at a given scattering angle θ is:[4]

$$Y = \sigma(\theta) \cdot \Omega \cdot Q \cdot N_s \tag{2.3}$$

where $\sigma(\theta)$ is the scattering cross section at the scattering angle θ, Q is the total number of incident ions, Ω is the detector solid angle, N_s is the number of target atoms per unit area. Therefore, the ratio between the yield of the α-particles backscattered by N, Y_N, and that from Ga, Y_{Ga} is

$$\frac{Y_N}{Y_{Ga}} = \frac{\sigma_N}{\sigma_{Ga}} \cdot \frac{N_s(N)}{N_s(Ga)} \tag{2.4}$$

where σ_N and σ_{Ga} are the scattering cross sections of nitrogen and Ga, and $N_s(N)$ and $N_s(Ga)$ are the numbers of nitrogen and Ga atoms per unit area, respectively. The scattering cross section σ is approximately proportional to $(Z_1 Z_2)^2$, where Z_1 and Z_2 are the atomic numbers of the incident and target elements.[5] Thus from Eq. 2.4,

$$\frac{Y_N}{Y_{Ga}} = \frac{(Z_{He} Z_N)^2}{(Z_{He} Z_{Ga})^2} \cdot \frac{N_s(N)}{N_s(Ga)} = \left(\frac{Z_N}{Z_{Ga}} \right)^2 \cdot \frac{N_s(N)}{N_s(Ga)} \approx 0.05 \frac{N_s(N)}{N_s(Ga)} \tag{2.5}$$

where Z_{He}=2, Z_N=7, and Z_{Ga}=31 are the atomic number of He, N, and Ga, respectively. Therefore, the yield of the α-particles backscattered by nitrogen is much smaller than the yield from Ga, or other heavy elements like In and As, especially when the nitrogen concentration is low. Therefore RBS does not provide information on N depth profile due to its relatively small mass.

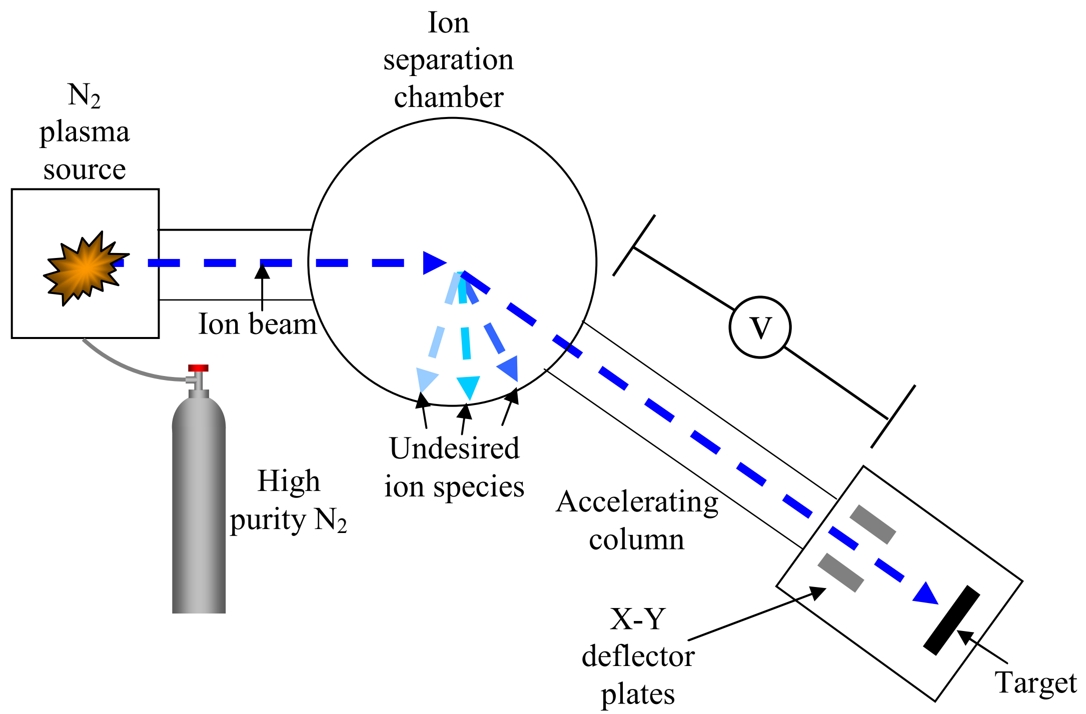

Fig. 2.1 Schematic of a typical ion implanter.

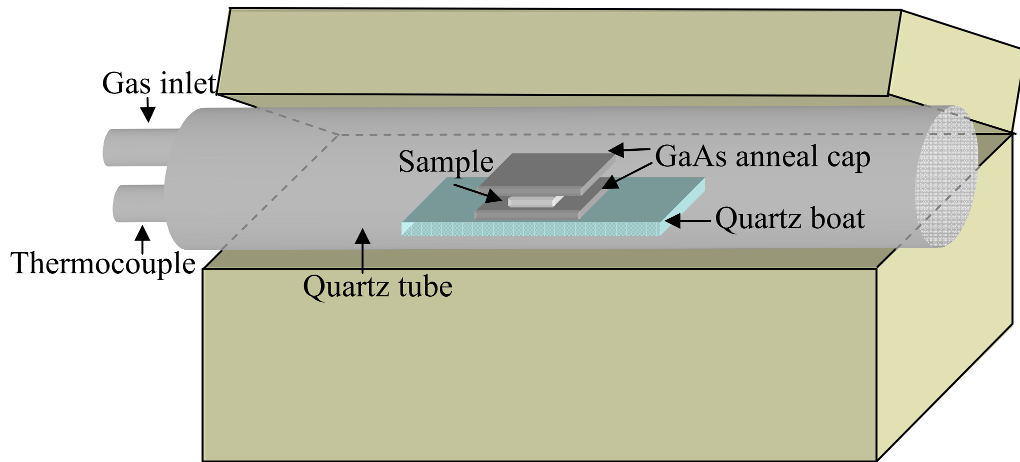

Fig. 2.2 Diagram of the furnace annealing setup. The sample sits between GaAs annealing caps on a quartz boat. The entire boat setup sits within a quartz tube purged with flowing gas controlled externally.

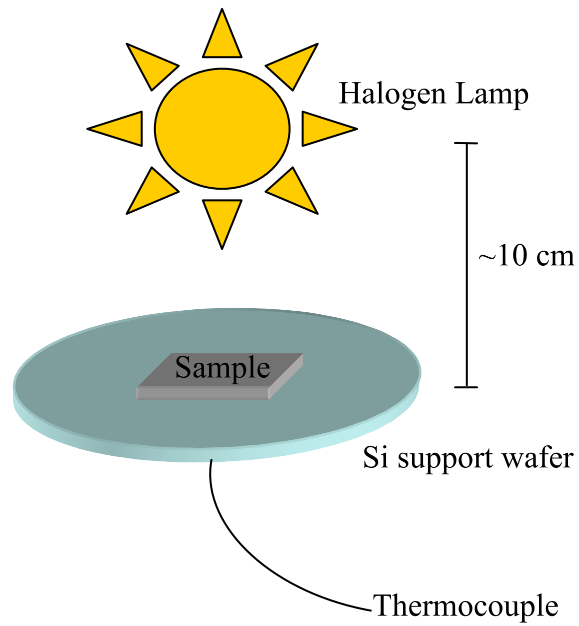

Fig. 2.3 Diagram of the rapid thermal annealing setup. The sample sits on a silicon wafer with a thermocouple contact on the underside. The chamber is purged with flowing nitrogen or argon gas and the sample is heated by a halogen lamp housed inside a quartz window.

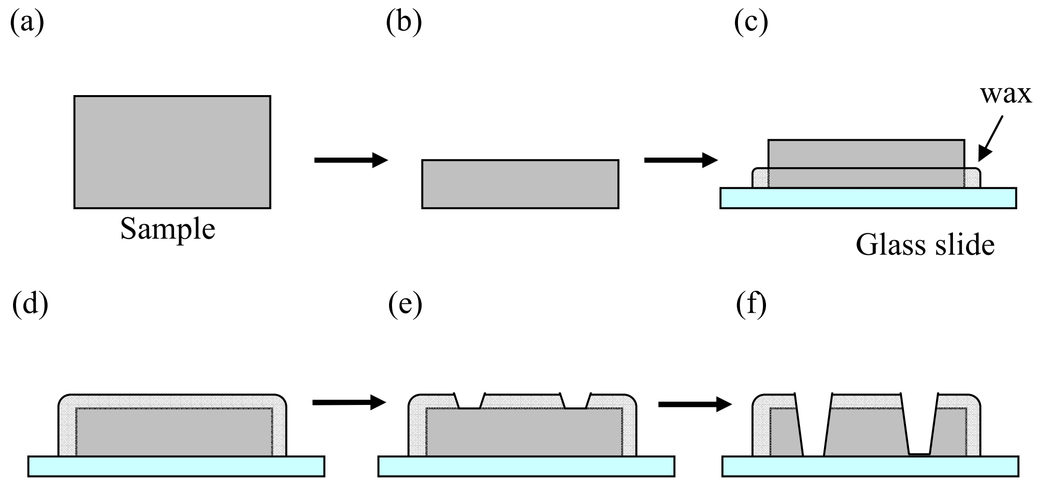

Fig. 2.4 Schematic of plan-view TEM specimens prepared by chemical etching. (a) The original sample is (b) polished from the back to a thickness of ~200 μm before (c) mounting film side down on a glass side using Crystalbond™. (d) The back of the sample is then covered in wax and a soldering iron is used to (e) melt holes in the wax coating. The sample is then dipped in solution and (f) etched until there is a perforation on the film side of the sample.

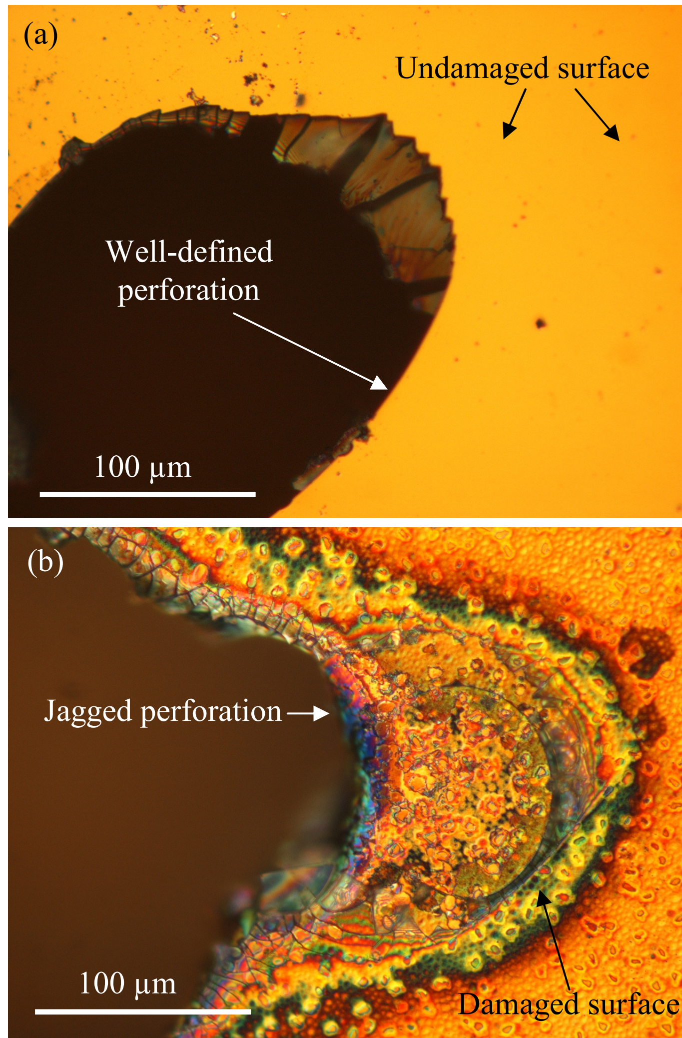

Fig. 2.5 Optical microscope views of chemically etched GaAs:N showing (a) an etched hole where etching was stopped after perforation, leaving a smooth edge along the hole and an undamaged surface. In (b), an etched hole was not removed from the etchant following perforation, resulting in a jagged hole edge and a partially etched, damaged surface layer.

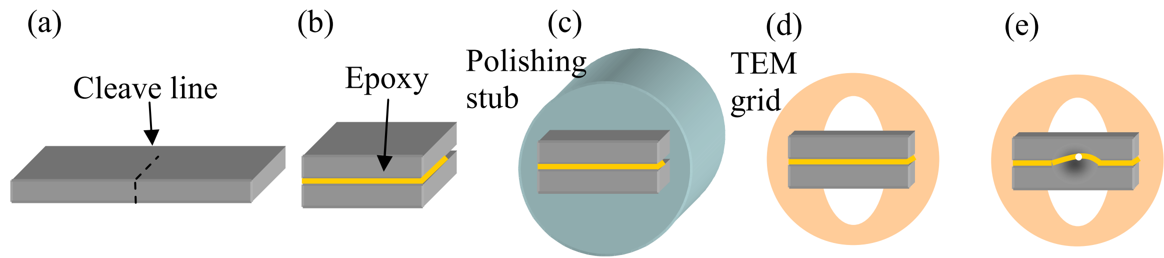

Fig. 2.6 Schematic of cross-sectional TEM polishing. The sample is (a) cleaved into two equal parts and (b) glued film side together using epoxy. The Sample is then (c) mounted on a polishing stub and polished on one side before (d) mounting on a TEM grid and polishing the opposite side to a final thickness of 75-100 µm. The sample is then (e) placed in an Ar ion miller and milled until a perforation is formed in the center of the sample.

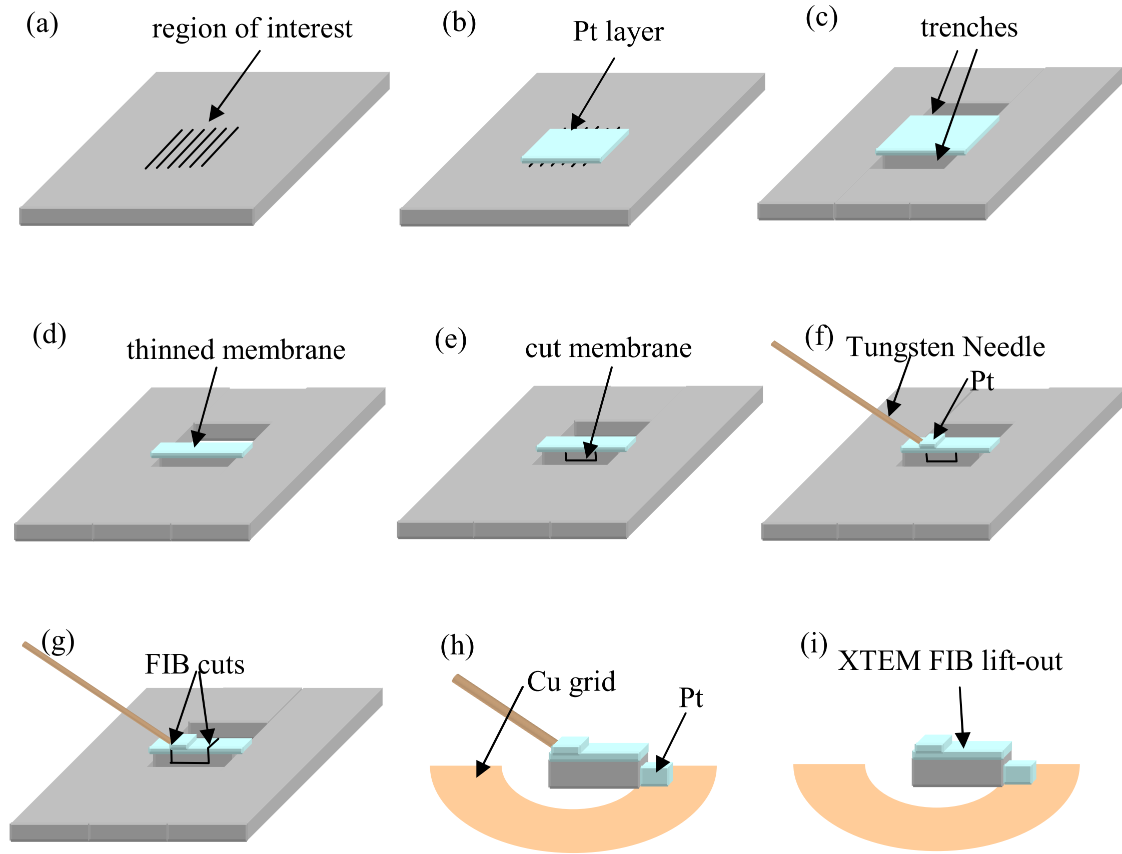

Fig 2.7 Schematic of FIB lift-out TEM sample preparation. An area of interest (a) is identified and then (b) a protective layer of Pt is deposited on the area of interest. The FIB is then used to mill trenches away from the sides of the Pt, as well as to (d) thin the area of interest. The FIB is then used to (e) cut notches spanning the area of interest, but leaving enough material to maintain contact between the sample and the bulk material. A tungsten needle is then brought in and (f) attached to the sample using Pt deposition. The FIB is then used to (g) cut notches to free the sample from the bulk material. The sample can then be lifted out on the needle and (h) deposited on a TEM half-grid using Pt deposition, where it is then (i) disconnected from the needle using the FIB beam.

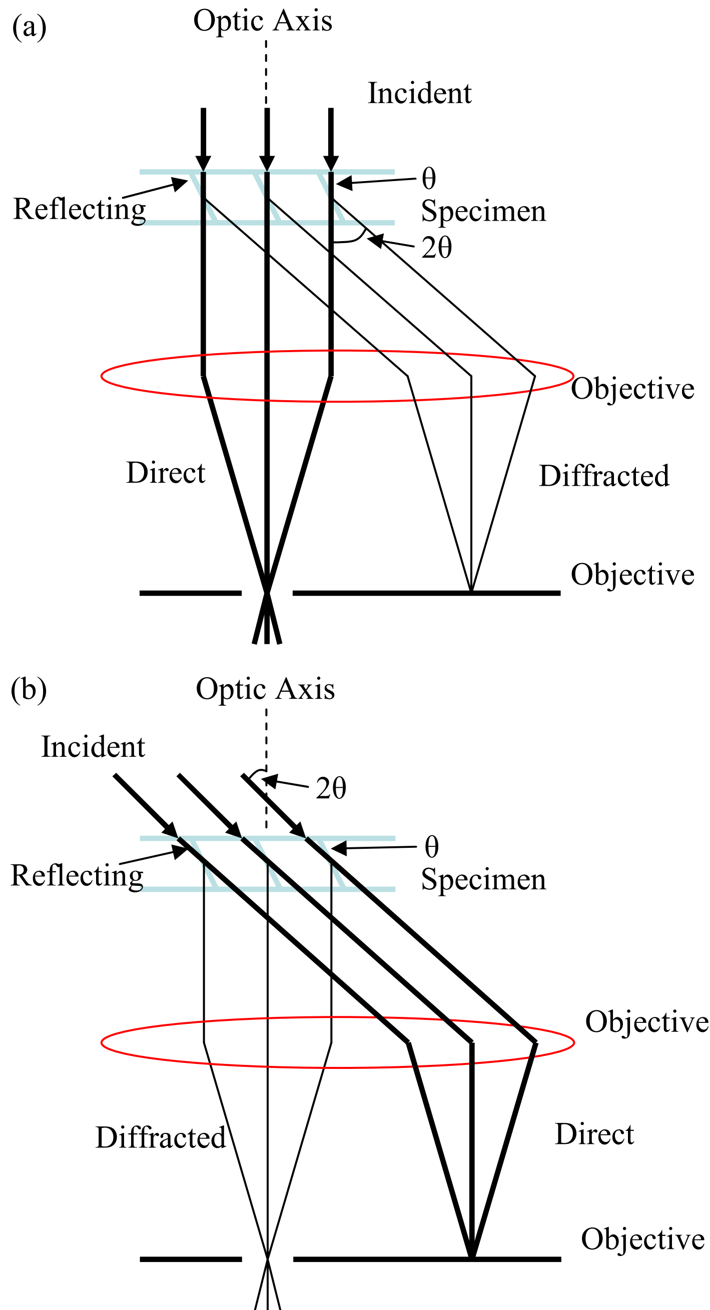

Fig. 2.8 Ray diagrams showing how the objective lens/aperture are used in combination to produce (a) a BF image from the direct beam and (b) a centered dark field image where the incident beam is tilted so that the scattered beam remains on axis. (Adapted from Ref. 3)

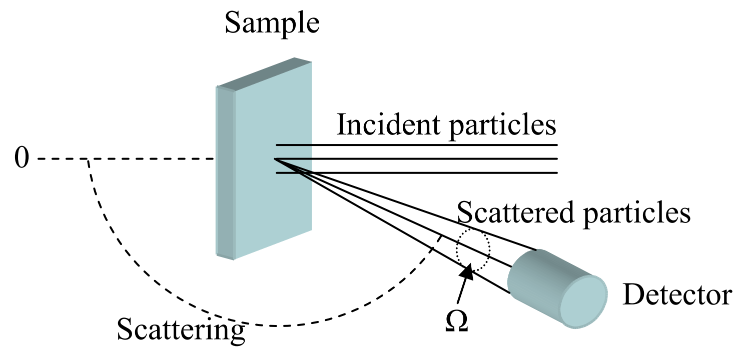

Fig. 2.9 Geometry of a backscattering experiment, illustrating the collection of backscattered particles in a solid angle Ω.

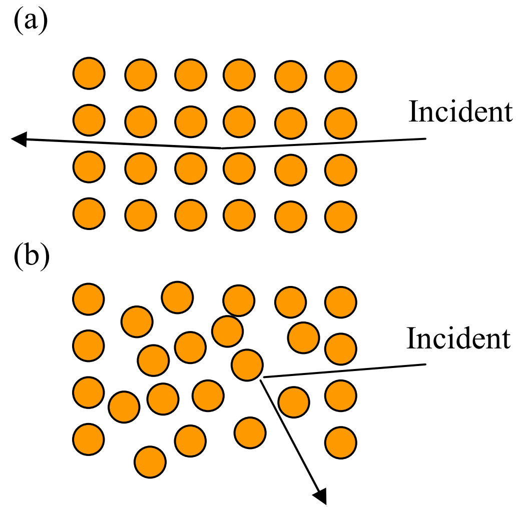

Fig. 2.10 Channeling in (a) a perfect crystal, for which the incident ion undergoes only small-angle scattering within the channel. Dechanneling may occur when the incident ion interacts with lattice defects, as shown in (b).

2.8 References

[1] L. A. Gianuzzi, J. L. Drown, S. R. Brown, R. B. Irwin, F. A. Stevie, *Micros. Res. & Tech*. **41** 285-290 (1998).

[2] M. Nastasi, J. W. Mayer, and J. K. Hirvonen, eds. *Ion-solid Interactions: Fundamentals and Applications* (Cambridge University Press, Cambridge, UK, 1996), Chapter 2.

[3] D. B. Williams and C. Barry Carter, eds. *Transmission Electron Microscopy* (Springer Science+Business Media, Inc. New York, 1996), Chapter 35.

[4] T. L. Alford, L. C. Feldman, and J. W. Mayer, *Fundamentals of Nanoscale Film Analysis* (Springer, New York, 2007), p. 17.

[5] L. R. Doolittle, *Nucl. Inst. Meth. Phys. Res. B* **9**, 344 (1985).

Chapter 3

Formation Mechanisms of Embedded InN Nanocrystals

3.1 Overview

This chapter describes our investigations of the formation of embedded InN nanocrystals using ion-beam-synthesis of InAs:N, similar to matrix seeded growth[1] of GaN nanostructures.[2,3] This chapter begins with background information on studies of InN nanostructure nucleation. Next, the experiments used to characterize nanocrystal structure are described. We then discuss the effect of annealing temperature on nanocrystal size and phase at nucleation. For our lowest rapid thermal annealing (RTA) temperatures, ZB InN nanocrystals are observed. As the RTA temperature is increased, the average nanocrystal size increases, and the formation of larger nanocrystals with WZ structure is consistent with the predictions of a thermodynamic model for the nanoscale-size-dependence of nucleation of ZB and WZ InN.[4] The nucleation of ZB InN at lower anneal temperatures is likely due to the lower surface energy of the ZB phase in comparison to the WZ phase for small nanocrystal radii. The chapter concludes with a summary.

3.2 Background

Due to its low electron effective mass,[5] high electron mobility,[6] and high room temperature drift velocity,[7] InN is perhaps the most promising group III-N material for solid state devices including long-wavelength light-emitters and detectors, high-performance electron devices, and high-efficiency solar cells. Recently, interest in InN has been renewed due to reports of a low bandgap energy of 0.65-0.8 eV[8,9] in lieu of the previously accepted value of 1.7-2.2eV for wurtzite (WZ) InN.[10,11] Interestingly, the band gap of zincblende (ZB) InN is predicted to be 0.58 eV,[12] slightly below that of WZ InN, providing an opportunity for extending nitride based light-emitting diodes (LEDs) to the near infrared.

ZB InN formation has been reported in 2D crystals[13,14,15] and nanowires.[16] InN nanostructures have been produced by metal-organic vapor-phase epitaxy (MOVPE), but these structures suffer from instabilities at ambient conditions, resulting in a gradual WZ to ZB phase transformation and the formation of group-III oxides.[17] Ion beams have been used to nucleate embedded WZ and ZB InN nanocrystals using N implantation into InP[18] and In and N co-implantation into Si,[19] respectively. Although N implantation into InAs has been examined,[20] the formation of InN nanocrystals embedded in InAs and the conditions for selective phase formation of ZB vs. WZ InN have not been reported.

3.3 Experiments

Following broad-area N-implantation of InAs, as described in Chapter 2, the samples were rapid thermal annealed (RTA) in argon gas at 500, 550, or 600°C for 30s. Cross-sectional transmission electron microscope (TEM) specimens were prepared using conventional mechanical polishing, followed by argon ion milling at 77 K. Dark-field images were obtained using the InAs {220} polycrystalline reflections and in some cases, the ZB InN {111} polycrystalline reflection. We note that WZ InN reflections were too weak for dark-field imaging. All SAD patterns were calibrated to the InAs substrate {110}.

3.4 Nitrogen Incorporation

We first consider the depth distribution of vacancy concentration and implanted N concentration following broad-area implantation. Figure 3.1 contains plots of vacancy concentration and N concentration vs. depth, as predicted by SRIM simulations of N implanted into InAs.[21] For 100-keV N^+ implantation, these SRIM simulations predict maximum vacancy and N concentrations at depths of 125 and 200 nm, respectively, indicated by arrows. The vacancy (nitrogen) concentration spans depths of 0 to 300 (0 to 350) nm.

Figure 3.2(a) presents a typical cross-sectional HAADF STEM image following implantation and RTA. EDX maps of In, As, and N were collected from regions ~540 x 420 nm. To determine the depth distribution of N, we assume a uniform sample thickness and estimate a Cliff-Lorimer factor[22] for InAs, k_{InAs}, from EDX data collected in regions of pure InAs, typically at depths from 250 to 300 nm below the surface. Details of this

calculation are available in Appendix B. A line-cut of EDX data from the surface to a depth of 300 nm reveals that the atomic percentage of N is highest in the top ~50 nm of the surface (Fig. 3.2(b)). For depths >50 nm, the N atomic % is negligible, indicating that after RTA, N incorporation is limited to the surface layer. Any N originally below the surface layer has likely segregated and agglomerated, forming gas bubbles, labeled with circles in Fig. 3.2(a), as discussed elsewhere.[23,24] Thus, it appears that the implanted N species has diffused toward the surface following RTA, similar to reports of InAs:Mg (ref. 25) and InAs:Fe (ref. 26).

3.5 Nanocrystal Formation

Figure 3.3 presents dark-field TEM images showing an overview of InAs:N (a) as-implanted and following RTA at (c) 500, (e) 550, and (g) 600°C. Most of the TEM images show evidence of 2 layers: (1) a surface layer whose thickness increases with annealing temperature, and (2) a crystalline middle layer with extended twinning, consistent with the HAADF STEM image presented in Fig. 3.1. The corresponding SAD patterns, shown in Figs. 3.3(b), 3.3(d), 3.3(f), and 3.3(h), respectively, reveal the formation of randomly-oriented nanocrystals within the surface layer. During annealing of the implanted InAs layer, there is a competition between nanocrystal nucleation at the surface and InAs recrystallization near the substrate. For low temperature RTA, recrystallization of InAs dominates, and the near-substrate layer expands. For high temperature RTA, N-incorporation dominates and the surface layer expands. Due to the volatility of group V elements at temperatures above 500°C,[27] as well as the reduced

thermal stability of InAs at temperatures nearing the melting point of InAs (942°C),[28] the expansion of the nitride nanocrystal layer is more significant than the recrystallization of InAs at higher temperatures. Indeed, at annealing temperatures in the range 650-700°C, a reduction in thermal stability of InAs was explained by significant Fe outdiffusion.[26]

For the as-implanted InAs:N, the dark-field TEM image presented in Fig. 3.3(a) reveals an apparently amorphous 200-nm surface layer. The width of this layer is consistent with the distribution of vacancies predicted by SRIM (Fig. 3.1). The SAD pattern corresponding to the surface layer, shown in Fig. 3.3(b), exhibits diffuse rings, confirming significant damage in the surface layer. However, high resolution TEM (HRTEM) images of the interface between the damaged layer and the host InAs matrix (Fig. 3.4(a)) indicate the presence of several grains within an amorphous matrix. These grains are crystalline InAs remnants which have maintained the tetrahedral coordination of the crystalline InAs.

Following RTA at 500°C, dark-field TEM imaging, presented in Fig. 3.3(c), reveals two layers: a 20-30 nm polycrystalline surface layer and a crystalline middle layer with extended defects. In the surface layer, bright spots indicate the formation of embedded nanocrystals with 5-20 nm separation. Both the crystallite formation and N incorporation appear to be confined to the surface layer, indicating that N incorporation is limited to the nanocrystals embedded in the surface. SAD collected from both the surface and middle layers is shown in Fig. 3.3(d). The diffraction spots are likely associated with misaligned InN nanocrystals within the surface layer. HRTEM of the nanocrystal region (Fig. 3.4(b)) indicates crystallite lattice parameters of 2.95 and 2.59 Å, within 4.8% of the {111} and {200} interplanar spacings of ZB InN.

We have also examined the influence of higher RTA temperatures on nanocrystal formation in N-implanted InAs. Figures 3.3(e) and 3.3(g) present dark-field TEM images of InAs:N following RTA at 550°C and 600ºC, respectively. For 550°C (600°C) RTA, the thickness of the polycrystalline surface layer has increased to ~50 nm (~80nm).

HRTEM from the vicinity of the surface-middle layer interface, shown in Fig. 3.4(c), reveals a single-crystalline middle layer with extended defects, while the surface layer consists of randomly oriented nanocrystals. SAD and HRTEM imaging indicate a density of twinning in the nanocrystals $< 19.4\ \mu m^{-2}$.

3.6 Nanocrystal Phase Analysis

Identification of nanocrystals was performed using SAD and HRTEM collected from the surface layers, presented in Figs. 3.3(f,h) and Figs. 3.3(d,e,f), respectively. Comparisons of the interplanar spacings determined by SAD and the powder diffraction standards from InAs and InN are shown in Table 3.1. For RTA at 550ºC, d-spacings of 2.85 and 2.48 Å are observed, corresponding to ZB InN phases. For RTA at 600ºC, d-spacings of 3.03, 2.59, 2.40, and 2.10 Å are apparent, within 3-4% {100} and {101}interplanar spacings of WZ InN, the {200} interplanar spacing of ZB InN, and the {102} interplanar spacing of WZ InN. These distortions are significantly lower than the 39% (22%) distortion for WZ (ZB) InN nanocrystals coherent with InAs, suggesting the formation of semi-coherent InAs/InN interfaces. The {002} reflection of WZ InN is likely missing due to the low density of WZ InN nanocrystals, as evidenced by the spotty and incomplete rings of SAD in Fig. 3.3(h). The nucleation of WZ InN is further

supported by the fact that the 2.59 and 2.10 Å rings lie between the {111} and {200} ZB InN reflections, and the {220} and {113} InAs reflections, respectively.

The nucleation of InN nanocrystals is confirmed by HRTEM studies (Figs. 3.4(d,e)), which reveal average lattice fringe spacings of 2.89 and 2.53 Å, within 2.4% of the {111} and {200} interplanar spacings of ZB InN. In addition, for the nanocrystals in Fig. 3.4(f), the average lattice fringe spacings are 2.83 and 2.61 Å, within 3.3% of the {002} and {101} interplanar spacings of WZ InN.

3.7 Nanocrystal Size Distribution

To consider the effect of nanocrystal nucleation size on the formation of WZ vs. ZB InN, a distribution of nanocrystal sizes, estimated from several dark-field TEM images, is presented in Fig. 3.5. We note that overexposed portions of the image were not included in the size analysis. We fit the size distributions with a Poisson log-normal regression for nanocrystal nucleation frequency as a function of radius and use the maximum likelihood estimation method to calculate the most probable nanocrystal radius.[29] With increasing RTA temperature, the maximum likelihood radius (MLR) increases from 1.3±0.2 nm (550°C RTA, Fig. 3.5(a)) to 2.6±0.4 nm (600°C RTA, Fig. 3.5(b)). Although the distribution of sizes includes several nanocrystals with radii as large as 3.9 nm (550°C RTA) and 8 nm (600°C RTA), the surface layer contains a larger number of nanocrystals with smaller radii, leading to a reduced MLR.

3.8 Mechanisms of Nanocrystal Nucleation

We now describe a thermodynamic model to consider the influence of nanocrystal size on the nucleation of ZB and WZ InN. The crystallites form in an amorphous matrix; thus, strain is not expected to play a role in their nucleation. Therefore, we assume an unstrained spherical solid nucleating from a liquid. We use the radial dependence of the InN surface energy, σ_{InN}, to estimate the size-dependence of the free energy for nucleation of ZB and WZ InN. A detailed calculation of free energy for the formation of nanocrystalline InN is presented in Appendix C.

The resulting difference in free energies, ΔG_{ZB}-ΔG_{WZ}, as a function of nanocrystal radius, is presented in Fig. 3.6. For 600°C (550°C) RTA, ZB InN is favored when $r <$ 6.25 Å (6.50 Å). For larger r, WZ InN is favored, consistent with literature reports for the relative stability of bulk WZ vs. ZB InN.[30,31] Indeed, with an increase in RTA temperature to 600°C, the MLR has increased, and both ZB and WZ GaN nanocrystals are apparent. For small r, the reduction in free energy of the ZB phase in comparison with the WZ is driven by a minimization of σ_{InN}. Figure 3.7 presents a model of (a) ZB and (b) WZ InN with the close packed surface planes indicated in pink (dark grey). Indeed, σ_{InN} is minimized by adoption of the ZB crystal structure, which has a higher density of low energy {111} surface planes in comparison with the WZ structure. Once the enthalpy and interfacial energies are known for nanoscale InN, a more complete prediction of the size-dependence of WZ vs. ZB nanocrystal formation is expected to be possible.

3.9 Conclusions

In summary, we have examined the formation of embedded InN nanocrystals using ion implantation followed by RTA. N implantation leads to the formation of a 200 nm, N-rich, amorphous surface layer. After RTA, randomly oriented nanocrystals are observed within the top 20-80 nm of the amorphized N-rich surface layer. The remainder of the N-rich surface layer forms a crystalline middle layer containing twin defects. RTA at 500 and 550ºC leads to the selective formation of ZB InN nanocrystals. Following RTA at 600ºC, the average nanocrystal size has increased, and both ZB and WZ InN nanocrystals are observed. These results are consistent with the predictions of a thermodynamic model for the influence of nanocrystal size on the nucleation of ZB and WZ InN.

d-spacing (Å) (experimental)		Powder diffraction standard (Å)		
550°C RTA	600°C RTA	ZB InN (hkl)	WZ InN (hkl)	InAs (hkl)
3.47	3.50			3.50 (111)
3.02	3.03		3.06 (100)	3.03 (200)
2.85		2.86 (111)	2.85 (002)	
	2.59		2.69 (101)	
2.48	2.40	2.47 (200)		
2.13	2.16			2.14 (220)
	2.10		2.09 (102)	
1.82	1.82			1.83 (113)

Table 3.1 Interplanar spacings of InAs:N following RTA at 550 and 600°C, determined from SAD, in comparison with the powder diffraction data for InAs and InN.

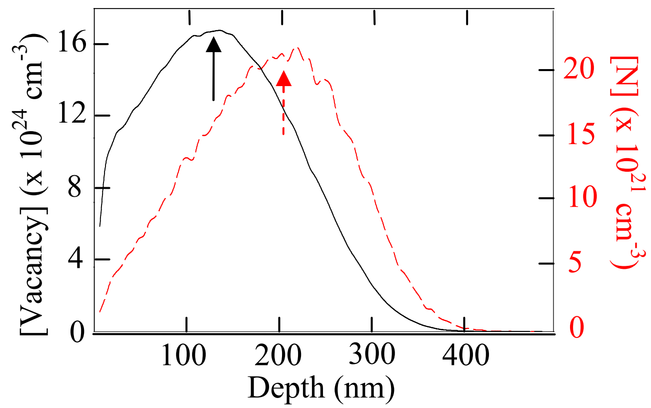

Fig. 3.1 SRIM simulation of vacancy and nitrogen concentrations as a function of depth for 100-keV N implantation into InAs. The vacancy concentration (solid) spans depths of 0 to ~300 nm, with a maximum at a depth of ~125 nm (solid arrow). The nitrogen concentration (dashed) spans depths of 0 to ~350 nm, with a maximum at a depth of ~200 nm (dashed arrow). The distribution of vacancies is consistent with the width of the amorphous layer following implantation.

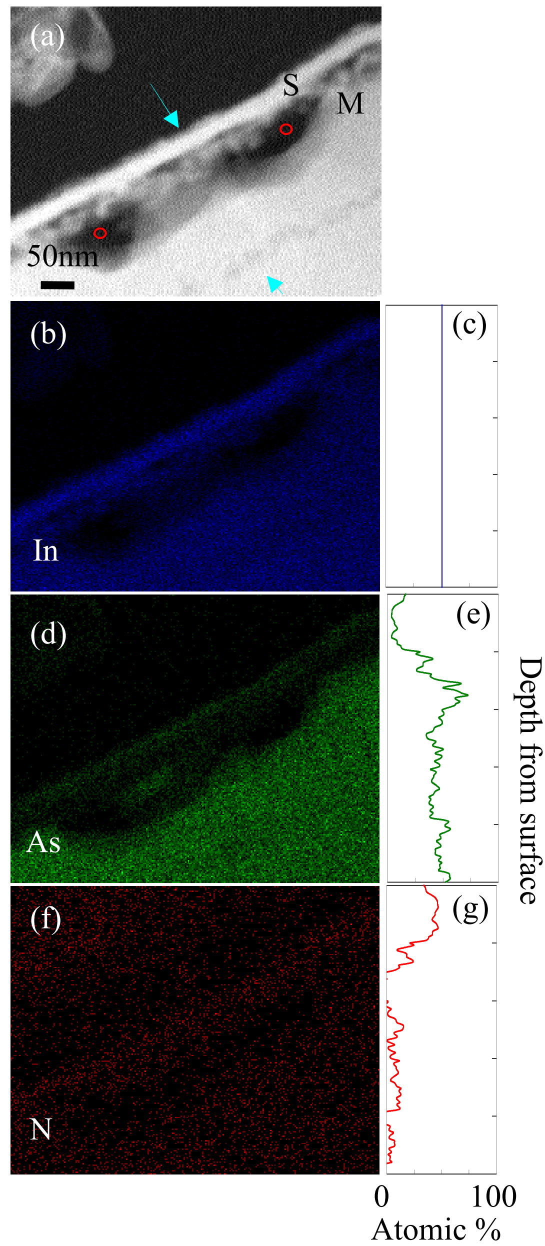

Fig. 3.2 (a) Cross-sectional HAADF STEM image and corresponding 2D XEDS spectral maps of a typical iplanted-plus-RTA sample with a nanocrystal-rich surface layer (S) and crystalline middle layer (M). Using the line-cut indicated in (a), with the y-coordinate expanded by 63%, the atomic ratios are presented for (c) In, (e) As, and (g) N. Popped Nitrogen bubbles are labelled with circles.

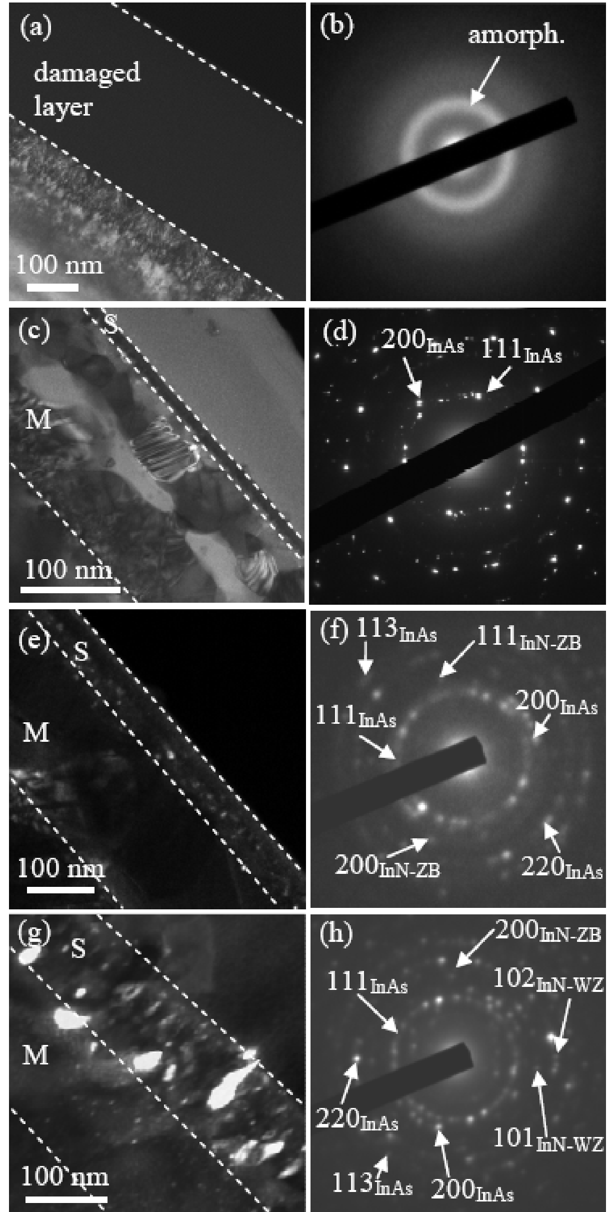

Fig. 3.3 Dark-field TEM images of (a) as-implanted InAs:N layers and InAs:N layers following RTA at (c) 500ºC, (e) 550ºC, and (g) 600ºC. The corresponding SAD patterns, collected from the damaged layer of (a) and surface (S) layer of (c), (e), and (g) are presented in (b), (d), (f), and (h), respectively.

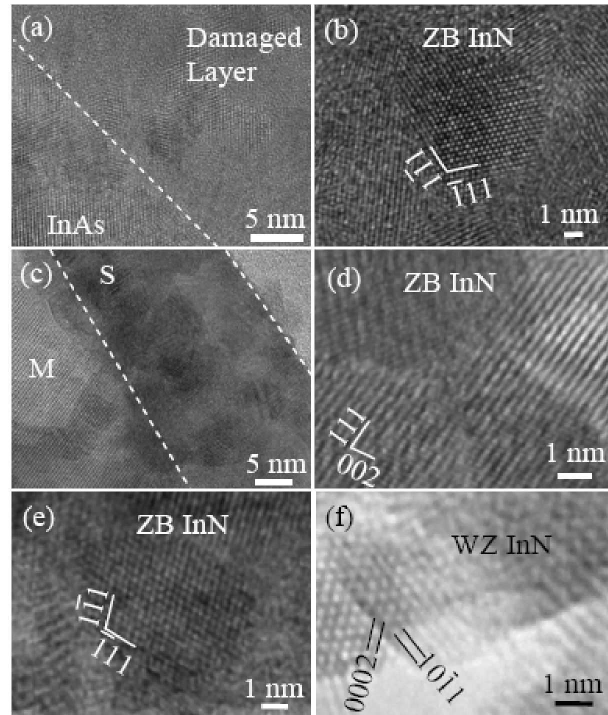

Fig. 3.4 HRTEM images of InAs:N layers (a) as-implanted and InAs:N layers following RTA at (b) 500°C, (c,d) 550°C, and (e,f) 600°C. For (a) the as-implanted layers, remnant grains of InAs in an amorphous matrix are apparent near the substrate layers. Following RTA at (b) 500°C and (c,d) 550ºC, polycrystalline nanostructures, with lattice parameters similar to ZB InN, within an amorphous matrix, are apparent in the surface (S) layers. Following RTA at 600ºC, both (e) ZB InN and (f) WZ InN nanocrystals have nucleated within the surface layer.

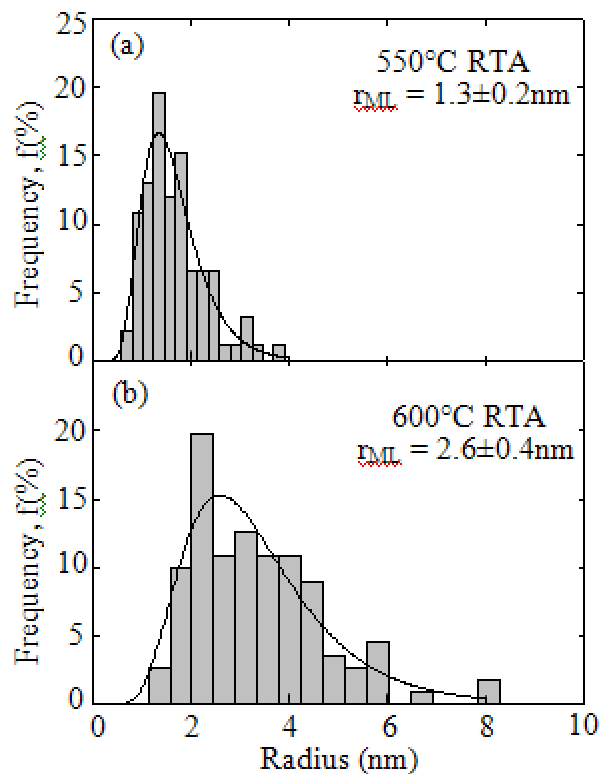

Fig. 3.5 Size distributions of the crystallites in implanted-plus-RTA InAs:N for RTA at (a) 550ºC and (b) 600ºC, estimated from analysis of dark-field TEM images. The size distribution was fit with a Poisson regression, overlayed on the distribution. A maximum likelihood estimate of nanocrystal radius gives r_{ML} values of 1.3 and 2.6 nm, respectively.

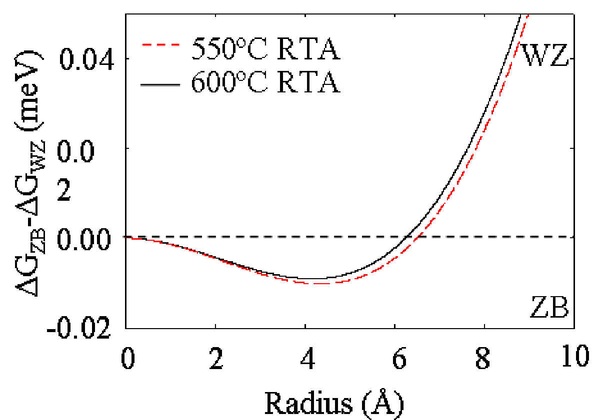

Fig. 3.6 Plot of the difference between the free energies of formation for WZ and ZB InN following RTA at 550°C (dashed line) and 600°C (solid line). For radii less than 6.5 Å (6.25 Å), the ZB phase is thermodynamically favored, while the WZ phase is favored for larger radii.

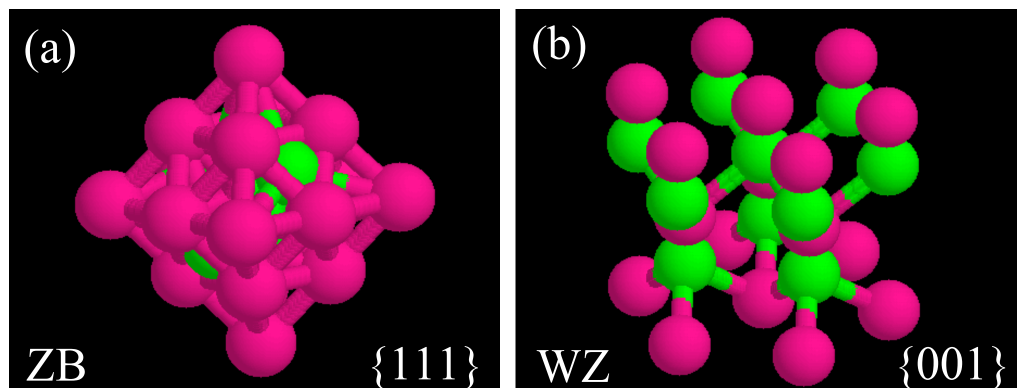

Fig. 3.7 Models of (a) ZB and (b) WZ GaN. Close packed surface planes are indicated in pink. There is a higher density of close packed {111} surface planes for ZB nanocrystals in comparison to the {001} close packed surface planes of WZ

3.10 References

[1] X. Weng, W. Ye, S. J. Clarke, R. S. Goldman, V. Rotberg, A. Daniel, and R. Clarke, *J. Appl. Phys*. **97**, 064301 (2005).

[2] X. Weng, S. J. Clarke, W. Ye, S. Kumar, R. S. Goldman, A. Daniel, R. Clarke, J. Holt, J. Sipowska, A. Francis, and V. Rotberg, *J. Appl. Phys.* **92**, 4012 (2002).

[3] X. W. Lin, M. Behar, R. Maltez, W. Swider, Z. Liliental-Weber, and J. Washburn, *Appl. Phys. Lett.* **67**, 2699 (1995).

[4] See supplementary material for details of size distribution and thermodynamic model for nucleation of ZB and WZ InN nanocrystals.

[5] J. Wu, W. Walukiewicz, W. Shan, K. M. Yu, J. W. Ager III, E. E. Haller, H. Lu, and W. J. Schaff, *Phys. Rev. B* **66**, 201403 (2002).

[6] V. W. L. Chin, T. L. Tansley, and T. Osotchan, *J. Appl. Phys*. **75**, 7365 (1994).

[7] S. K. O'Leary, B. E. Foutz, M. S. Shur, U. V. Bhapkar, and L. F. Eastman, *J. Appl. Phys*. **83**, 826 (1998).

[8] V. Yu. Davydov, A. A. Klochikhin, V. V. Emtsev, S. V. Ivanov, V. V. Vekshin, F. Bechstedt, J. Furthmüller, H. Harima, A. V. Mudryi, A. Hashimoto, A. Yamamoto, J. Aderhold, J. Graul, and E. E. Haller, *Phys. Stat. Sol. B* **230**, R4 (2002).

[9] J. Wu, W. Walukiewicz, K. M. Yu, J. W. Ager III, E. E. Haller, H. Lu, W. J. Schaff, Y. Saito, and Y. Nanishi, *Appl. Phys. Lett*. **80**, 3967 (2002).

[10] N. Puychevrier and M. Menoret, *Thin Solid Films* **36**, 141 (1976).

[11] K. L. Westra and M. J. Brett, *Thin Solid Films* **192**, 227 (1990).

[12] F. Bechstedt, J. Furthmüller, M. Ferhat, L. K. Teles, L. M. R. Scolfaro, J. R. Leite, V. Yu. Davydov, O. Ambacher, and R. Goldhahn, *Phys. Stat. Sol. (a)* **195**, 628 (2003).

[13] C. L. Hsiao, T. W. Liu, C. T. Wu, H. C. Hsu, G. M. Hsu, L. C. Chen, W. Y. Shiao, C. C. Yang, A. Gällström, P. O. Holtz, C. C. Chen, and K. H. Chen, *Appl. Phys. Lett*. **92** 111914 (2008).

[14] J. G. Lozano, F. M. Morales, R. García, D. González, V. Lebedev, Ch. Y. Wang, V. Cimalla, and O. Ambacher, *Appl. Phys. Lett*. **90**, 091901 (2007).

[15] X. Xu, P. Specht, R. Armitage, J. C. Ho, E. R. Weber, and C. Kisielowski, *Appl. Phys. Lett*. **87**, 092102 (2005).

[16] C. Nie, R. Zhang, Z. L. Xie, X. Q. Xiu, B. Liu, D. Y. Fu, Q. J. Liu, P. Han, S. L. Gu, Y. Shi, and Y. D. Zheng, *Chin. Phys. Lett.* **25**, 1780 (2008).

[17] D. González, J. G. Lozano, M. Herrera, N. D. Browning, S. Ruffenach, O. Briot, and R. García, *J. Appl. Phys*. **105**, 013527 (2009).

[18] K. Santhakumar, R. Kesavamoorthy, K. G. M. Nair, P. Jayavel, D. Kanjilal, V. Sankara Sastry, and V. Ravichandran, *Nucl. Inst. Meth. Phys. Res. B* **212**, 521 (2003).

[19] Y. K. Huang, C. P. Liu, Y. L. Lai, C. Y. Wang, Y. F. Lai, and H. C. Chung, *Appl. Phys. Lett.* **91**, 091921 (2007).

[20] X. Weng, W. Ye, S. J. Clarke, R. S. Goldman, V. Rotberg, A. Daniel, and R. Clarke, *J. Appl. Phys*. **97**, 064301 (2005).

[21] J. F. Ziegler, J. P. Biersack, and U. Littmark, *The Stopping and Range of Ions in Matter*: Web site: http://www.srim.org/. SRIM 2006.

[22] D. Williams and C. B. Carter, in *Transmission Electron Microscopy: a Textbook for Materials Science*, (Springer Science+Business Media, Inc., New York, 1996), p.600.

[23] R. R. Collino, B. B. Dick, F. Naab, Y. Q. Wang, M. D. Thouless, and R. S. Goldman, *Appl. Phys. Lett.* **95**, 111912 (2009).

[24] X. Weng, W. Ye, J.C. Mabon, and R. S. Goldman, *J. Vac. Sci. Technol. B* **22**(3), 989 (2004).

[25] S. J. Pearton, A. R. Von Neida, J. M. Brown, K. T. Short, L. J. Oster, and U. K. Chakrabarti, *J. Appl. Phys.* **64**, 629 (1988).

[26] H. Ullrich, A. Knecht, H. Kräutle, W. Schlaak, and D. Bimberg, *J. Appl. Phys*. **72**, 3514 (1992).

[27] W. Wesch, *Nucl. Inst. Meth. Phys. Res. B* **68**, 342 (1992).

[28] P. S. Dutta, and T. R. Miller, *J. Electronic. Mater*. **29**, 956 (2000).

[29] P. R. Bevington, in *Data Reduction and Error Analysis for the Physical Sciences*, (McGraw-Hill, Inc., New York, 1969), p.110.

[30] M. Leszczynski, in *Properties, Processing and Applications of Gallium Nitride and Related Semiconductors*, edited by J.H. Edgar, S.T. Strite, I. Akasaki, H. Amano, and C. Wetzel (INSPEC, London, UK, 1999), p.3.

[31] C. Caetano, L. K. Teles, M. Marques, A. Dal Pino, Jr., and L. G. Ferreira, *Phys. Rev. B* **74**, 045215 (2006).

Chapter 4

Formation of GaN-rich Nanocrystals in Nitrogen Implanted GaAs

4.1 Overview

This chapter opens with background information, including applications of GaAsN. Next, the experimental details of these investigations are described. We then discuss the influence of broad-area implantation energy on the nucleation of ZB and/or WZ GaN nanocrystals. The bulk of this chapter is devoted to our studies of the influence of annealing temperature and annealing time on the formation and growth of GaN. The correlation between nanocrystal nucleation size and nanocrystal phase are investigated. We find that with increasing nanocrystal size, there is a transformation from ZB to WZ GaN. Furthermore, we present a TTT diagram for the transformation of zincblende and wurtzite GaN in ion-implanted GaAs. The chapter concludes with a summary.

4.2 Background

GaN and related compounds have been studied for potential applications in light-emitting diodes (LEDs) operating through the visible spectrum, and as electronic devices suited for high temperature, high power, and high frequency applications.[1,2] GaN

generally grows in a stable wurtzite (WZ) phase, but a metastable zincblende (ZB) phase has been reported under certain growth conditions.[3,4] WZ GaAsN has potential applications toward short-wavelength lasers,[5,6] while ZB GaAsN is promising for optical communications (λ 1.3-1.55 μm) and integration with Si-based technologies.

GaN nanostructure formation has been reported following ion implantation plus rapid thermal annealing (RTA) or furnace annealing (FA). High energy (100-keV) N implantation into GaAs results in an amorphous layer, with or without crystalline remnants.[7] Following RTA at 750-850°C for 30 s, ZB GaN nanocrystals are nucleated in the amorphous regions.[8] For FA > 2 min, the formation of Ga-N bonds,[2,9,10,11,12,13] the nucleation of WZ GaN,[1,14,15] and/or WZ and ZB GaN[3,4,16,17] have been reported, as summarized in Table 4.1. In addition, a plot of the annealing time and temperature dependence of ZB and/or WZ GaN nucleation is presented in Fig 4.1. From this plot, it is apparent that the range of temperatures and annealing durations for which nucleation of WZ GaN, and the transition from the ZB to the WZ phase occur, are not well defined. Therefore, we have examined the mechanisms for formation and transformation of ion-beam-synthesized GaN nanocrystals. We find that post-implantation RTA at 600 and 650ºC leads to the formation of polycrystalline GaAs and GaN-rich nanocrystals, respectively. Longer anneals at 650ºC leads to the nucleation of wurtzite GaN.

4.3 Experimental Details

Following broad-area N-implantation of GaAs, the samples were annealed either via RTA in argon gas for 30 s at 650°C or 900°C, or FA in a quartz tube furnace for 10

min. Cross-sectional TEM specimens were prepared using conventional mechanical polishing, followed by argon ion milling at 77 K, or in some cases, using FIB lift-out.[18] Plan-view TEM specimens were prepared by chemical etching, as described in Chapter 2.

4.4 Role of Implantation Energy

Figure 4.2 presents dark-field TEM images showing an overview of GaAs:N following implantation-plus-RTA at (a) 75 keV with a fluence of 2.5×10^{17} cm^{-2} and (c) 100 keV with a fluence of 5.0×10^{17} cm^{-2}. The TEM images show evidence of 3 layers: (1) a surface layer, (2) a 175 (220) nm-thick nanocrystal layer, and (3) a near-substrate layer. The corresponding SAD patterns for 75 and 100 keV implantations, shown in Figs. 4.2(b) and 4.2(d), respectively, indicate that RTA induces the formation of randomly-oriented grains within the nanocrystal layer. The nanocrystals have a MLR of 1.04±0.53 nm (75 keV) and 1.37±0.36 nm (100 keV), indicating that the implantation energy does not significantly affect the size of the nucleated nanocrystals.

Identification of nanocrystals was performed using SAD collected from the nanocrystal layers following 75 keV and 100 keV implantation-plus-RTA, as shown in Figs. 4.2(b) and 4.2(d), respectively. The interplanar spacings determined by SAD and the powder diffraction standards from GaAs and GaN are summarized in Table 4.2. For all nanocrystal layers, interplanar spacings within 1.8% of the {111}, {220}, and {311} planes of GaAs are observed. Additionally, for 100 keV (75 keV) nanocrystal layers, interplanar spacings within 2.5% of the {111} and {220} ({111}) planes of ZB GaN are observed. For the 75 keV case, the {220} reflection of ZB GaN is likely missing due to a

relatively low density of GaN nanocrystals. The nanostructures have been shown to preferentially nucleate at implantation damage sites.[19,20] Since SRIM simulations predict a factor of 2 lower maximum vacancy concentration for 75 keV (~1.0x10^{25} cm^{-3}) in comparison to that of 100 keV N^+ implantation (~1.9x10^{25} cm^{-3}), a lower density of nanocrystals in the 75 keV implanted-plus-RTA sample is expected.[20] Preferential nucleation of ZB GaN is indicated by the presence of the {111} reflections of ZB GaN, while the {110} reflections of WZ GaN are absent.

4.5 Temperature-dependence of GaN Nucleation

Dark-field TEM of GaAs:N following RTA at (a) 600°C, (c) 650ºC, and (e) 900ºC is presented in Fig. 4.4. A ~200 nm nanocrystal layer below a thin surface layer is observed. The corresponding SAD patterns, shown in Figs. 4.4(b), 4.4(d) and 4.4(f), respectively, indicate that RTA induces the formation of randomly-oriented grains within the nanocrystal layer. Comparisons of the interplanar spacings determined by SAD with the powder diffraction standards from GaAs and GaN are presented in Table 4.2. For the 600ºC (650ºC) implanted-plus-RTA sample, interplanar spacings within 0.9% of the {111}, {220}, and {311} ({220} and {400}) planes of GaAs are observed. Additionally, for both the 650°C and 900°C RTA implanted-plus-RTA samples, interplanar spacings within 2.2% of the {111}, {220}, and {311} planes of ZB GaN are observed. Hence, initial nucleation of GaN has occurred between 600ºC and 650°C. Furthermore, GaAs reflections are not observed in the 900ºC sample, indicating that at higher temperatures,

the nucleation of GaN dominates over the nucleation of GaAs. A similar observation was discussed for N-implanted InAs in Chapter 3, which has also appeared in the literature.[22]

4.6 Annealing Time-dependence of GaN Nucleation

We also consider the effect of longer annealing times achieved by FA on nanocrystal nucleation and growth. Figure 4.5 presents dark-field TEM of N-implanted GaAs following FA for 10 min at 650°C. SAD collected from an area including both the implanted layer and the substrate is presented in Fig 4.5(b). Interplanar spacings within 0.8% of the {101}, {110}, and {103} planes of WZ GaN are observed. This is in contrast to the observation of ZB GaN following RTA at 650°C, as discussed above. Thus, it is likely that the longer annealing time has enabled the transformation of ZB GaN to WZ GaN.

4.7 Mechanisms for ZB vs. WZ GaN Nucleation

It is interesting to note that the ZB phase has formed following both 75 and 100 keV implantation-plus-RTA, although WZ is predicted to be the most stable thermodynamically.[21] As we discussed in Chapter 3 and reported in the literature,[20,22] for small radii, the reduction in free energy of the ZB phase in comparison with the WZ phase is driven by a minimization of the surface energy. Figure 4.6 presents a model of (a) ZB and (b) WZ GaN with the close-packed surface planes indicated in pink (dark grey). Indeed, the surface energy is minimized by adoption of the ZB crystal structure,

which has a higher density of low energy {111} surface planes in comparison with the low energy {001} surface planes of WZ GaN.

To consider the effect of nanocrystal size at nucleation on the formation of WZ vs. ZB GaN, a plot of GaN nanocrystal radius at nucleation, r^{nuc}, as a function of RTA temperature is presented in Fig. 4.7. For RTA at 650°C, ZB GaN is nucleated with r^{nuc} = 0.92 ± 0.22 nm. For 800 and 900°C RTA, r^{nuc} increases to 1.37 ± 0.36 nm and 1.25 ± 0.32 nm, respectively, within error of previously reported values.[8] Thus, averaging with previously reported values, it appears that the maximum RTA-induced GaN nanocrystal size at nucleation, $r^{\max}$, is ~1.75 nm. Since the WZ GaN phase has not been observed in RTA reports to date, $r^{\max}$ is likely below that required for transformation to WZ GaN nucleation, r^{trans}. However, WZ (ZB) GaN was observed at FA (RTA) temperatures of 650°C. Therefore, it is likely that FA provides a sufficient annealing time for the observed GaN nanocrystal nucleation radius, r^{FA}, to grow larger than r^{trans}. Indeed, r^{FA} values greater than 12.5 nm have been reported for WZ GaN,[4] significantly larger than $r^{\max}$.

4.8 TTT Diagram

We next consider the nucleation and growth of the ZB GaN nanocrystals using a generalized Johnson-Mehl-Avrami equation. The time between two fractions of transformation, f_1 and f_2, is obtained from the activation energy for diffusion, E_d=1.0 eV (ref. 8), at a temperature, T, using the relation[23]

$$\ln(t_{f_2} - t_{f_1}) = \frac{E_d}{RT} + C \quad (4.1)$$

where C is a constant and R is the gas constant. We define f_1 and f_2 as the initial nucleation of ZB GaN, and the 100% nucleation of ZB GaN, respectively. At $r^{\max}$, we assume that the transformation fraction has reached f_2.

In Fig. 4.8, we plot annealing temperature vs. annealing time for nucleation of WZ GaN, indicated by triangles, using data from this paper, plus those listed in Table 4.1 (plotted in Fig. 4.1). For the transformation to WZ GaN, we fit the T vs. time data to Eq. 4.1 using a logarithmic regression. The half-nose shape indicates a competition between the driving force for nanocrystal nucleation, which increases with decreasing temperature, and atomic mobility, which decreases with decreasing temperature.

The nanocrystal nucleation rate is then expressed as

$$\frac{dN}{dt} = K\left[\exp(\frac{\Delta G}{kT})\exp(\frac{E_n}{kT})\right] \quad (4.2)$$

where K is a temperature-independent constant related to the number of atoms on the nanocrystal surface, ΔG is the activation free energy, and E_n is the activation energy for nucleation. We assume time-independent variables, integrate Eq. 4.2 over time, and solve for ln(t) as a function of the total number of nuclei, N:

$$\ln(t) = \ln(\frac{N}{K}) + \frac{\Delta G - E_n}{kT} \quad (4.3)$$

The nanocrystal growth rate is then expressed as

$$\frac{dV}{dt} = C\exp(-\frac{E_d}{kT}) \quad (4.4)$$

where E_d is the activation energy for diffusion and C is a pre-exponential. Assuming a time-independent E_d and C, we integrate Eq. 4.4 over time and solve for ln(t) as a function of the total nanocrystal volume, V:

$$\ln(t) = \ln(\frac{V}{C}) + \frac{E_d}{kT} \quad (4.5)$$

We now compare the expressions for NC nucleation (Eq. 4.3) and growth (Eq. 4.5) of WZ and ZB GaN. Since the NC nucleation energy is determined by the Ga-N bond energy, we assume that differences in E_n for ZB and WZ GaN are negligible. For both ZB and WZ NCs, nucleation and growth occur within an amorphous GaAsN matrix; thus, E_d, the activation energy for diffusion, is assumed to be equivalent (1.0 eV) in both cases.[20] We consider the nucleation of similarly-sized ZB and WZ GaN NCs, such that $\Delta G_{ZB} \cong \Delta G_{WZ}$ at the ZB-WZ phase transition. Since the competition between nucleation and growth determines the curvature of the NC time-temperature-transformation, we consider identical curvatures for both the WZ GaN and ZB GaN f_2 transformations. In Fig. 4.8, we plot the data point for f_2 following annealing at 750°C for 30 s, indicated by a circle. We then plot the f_2 curve for temperatures ranging 600-850°C with the same curvature as that of the WZ transformation curve.

We now consider the ZB f_1 curve. We define f_1^{650} as the initial nucleation of ZB GaN following annealing at 650°C, the lowest annealing temperature that results in ZB GaN nucleation. f_1^{650} occurs for annealing time $t_{f_1}^{650}$ = 30 s, and we use f_2 to calculate $t_{f_2}^{650}$ = 85 s. Using Eq. 4.1, we calculate a value of C = -12.7. We then calculate values

of t_{f_1} for temperatures ranging 600-850°C using Eq. 4.1, and plot the ZB f_l curve in Fig. 4.8.

Annealing paths for RTA at 650 and 750°C, and a FA curve for 650°C are overlaid on the plot (dashed lines) in Fig. 4.8. For RTA at 650°C for 30 s followed by quenching to RT, ZB GaN (square) is nucleated, but only partially transformed prior to the quench to RT, during which polycrystalline-GaAs nucleates. For RTA at 750°C for 30 s, ZB GaN nucleation begins at ~20 s and transforms to 100% ZB (square) prior to the quench to RT. In the case of FA at 650°C for 10 min, WZ GaN is nucleated prior to the quench. For longer FA durations, a more complete WZ transformation occurs, as observed in the literature.[4] Additional time-temperature-phase data is needed for a complete set of ZB and WZ time-temperature-transformation curves.

4.9 Conclusions

In summary, we have examined the nucleation and transformation of ZB and WZ GaN nanocrystals in GaAs prepared via matrix-seeded growth. Post implantation RTA at 600 to 900ºC leads to the formation of polycrystalline GaAs and ZB GaN, with a maximum nanocrystal radius, r^{max}~1.75 nm. For FA, we observe a transformation to WZ GaN. We have developed a TTT diagram which describes the nucleation and growth of ZB GaN and the transformation to WZ GaN. Once the annealing times and temperatures are known, a complete description for the nucleation and transformation of GaN over a wide range of temperatures and annealing times may be achieved. Our

methods may also be readily integrated with other materials systems that crystallize in the WZ and/or ZB structures.

Table 4.1 Literature reports on N ion irradiation of GaAs, followed by thermal annealing at various temperatures for times ranging from 30 s to 120 min.

[ref. #] Author	Method of Growth	Anneal Conditions (°C)	Nitride Formation
[7] X. Weng, *et al*.	N^+ irradiation	750-850 for 30 s	ZB GaN
[8] X. Weng, *et al*.	N^+ irradiation	800 for 30 s	ZB GaN
[10] DeLouise	N^+ irradiation	200-500	GaN – unknown phase
[24] DeLouise	N^+ irradiation	200-500	GaN – unknown phase
[25] Makimoto, *et al*.	Nitridation of MBE GaAs	530-645 for 90 min	ZB GaN
[4] Lin, *et al*.	N^+ irradiation	850-950 for 10-120 min	ZB and WZ GaN
[16] Hullavarad, *et al*.	Nitridation of MBE GaAs	500 for 10-90 min	ZB and WZ GaN
[14] Boudart, *et al*.	N^+ irradiation	500-950 for 5 min	WZ GaN at 650-850°C
[2] Li, *et al*.	N^+ irradiation	300-600 for 5-90 min	Ga-N bonding
[11] Hecht, *et al*.	N^+ irradiation	300 for 6.5 min	GaN - unknown phase
[12] Ho, *et al*.	N^+ irradiation	850 for 2 min	GaN – unknown phase
[13] Meškinis, *et al*.	Nitridation of MBE GaAs	650 for 15 min	GaN – unknown phase
[1] Lo, *et al*.	N^+ irradiation	800-1000 for 2 min	WZ GaN at 800, 850°C
[3] Dhara, *et al*.	N^+ irradiation	900 for 15 min	ZB and WZ GaN
[17] Bae, *et al*.	N^+ irradiation	700 for 60 min	ZB and WZ GaN
[15] Baranwal, *et al*.	N^+ irradiation	850 for 30 min	WZ GaN
[9] Majlinger, *et al*.	N^+ irradiation	350-400 for 60 min	Ga-N bonding

Table 4.2 Interplanar spacings measured by SAD of GaAs:N following implantation at ion energies of 75-keV and 100-keV, and RTA at 800°C, in comparison to powder diffraction standards.

d-spacing (Å) (experimental)						Powder Diffraction Standard (Å)		
75 - keV	100 - keV	600°C RTA	650°C RTA	900°C RTA	650°C furnace	ZB GaN (hkl)	WZ GaN (hkl)	GaAs (hkl)
3.26	3.26	3.29						3.26 (111)
2.62	2.59		2.62	2.60		2.60 (111)		
					2.46		2.44 (101)	
2.03	2.01	1.99	2.08		2.07			2.00 (220)
1.73	1.71	1.71			1.72			1.70 (311)
	1.55		1.59	1.59	1.58	1.59 (220)	1.59 (110)	
			1.46		1.46		1.46 (103)	1.41 (400)
			1.33	1.36		1.36 (311)		1.30 (331)

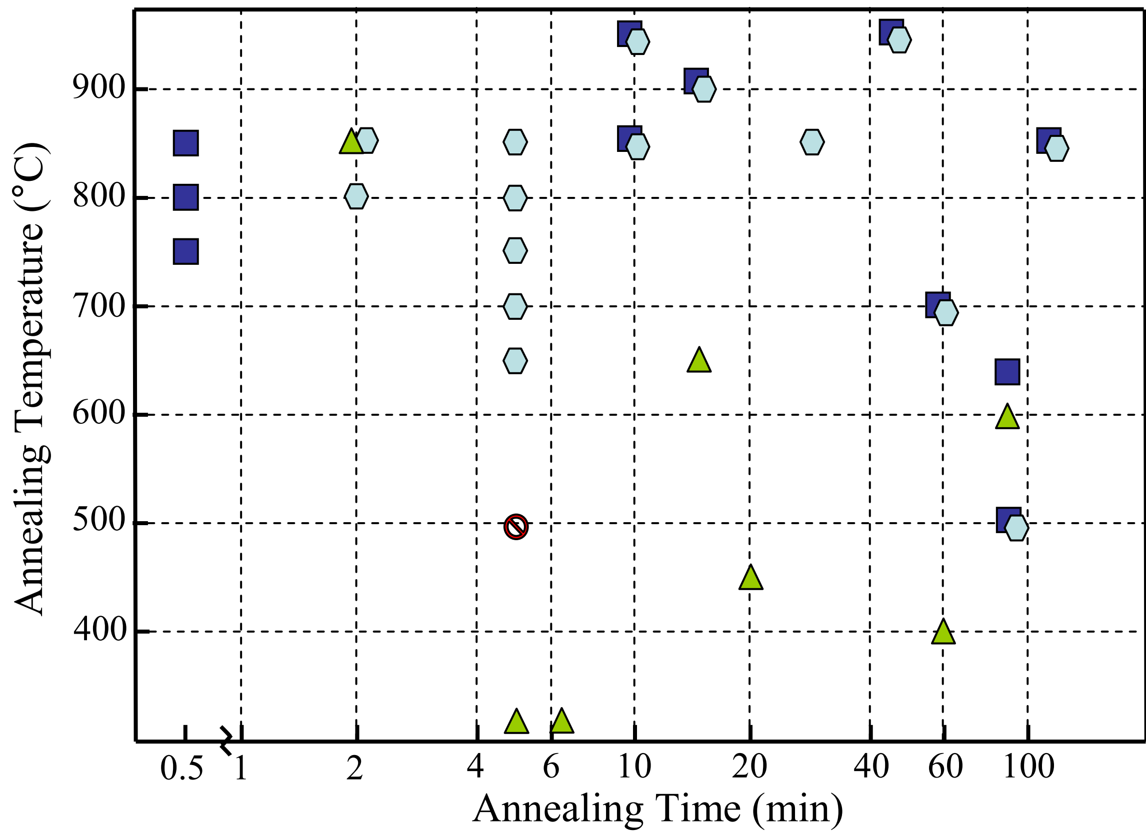

Fig. 4.1 Annealing time vs. annealing temperature for N ion-implanted GaAs, compiled from the references in Table 4.1. Short (30s) anneals at high temperatures lead to the nucleation of ZB GaN (square). Following high temperature annealing for longer annealing times (>1 min), WZ GaN (hexagon) is observed. In some FA studies, Ga-N bonding is reported (triangle) without identification of a phase.

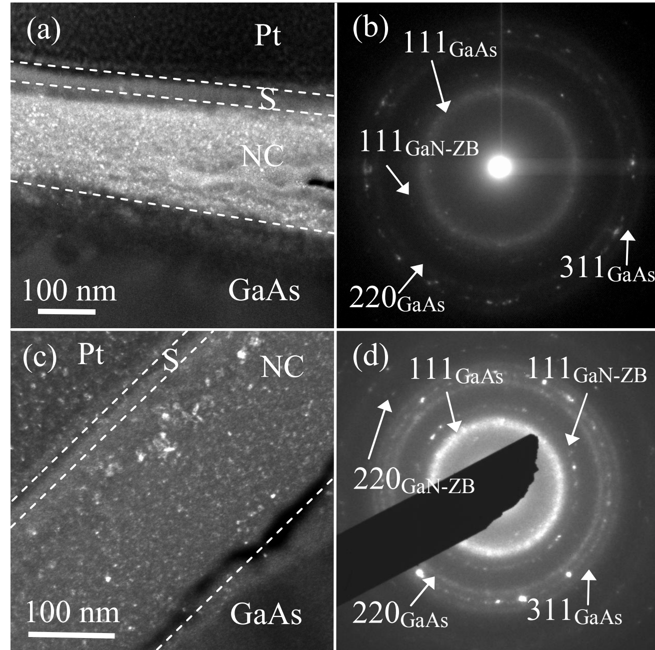

Fig. 4.2 Dark-field TEM images of annealed GaAs:N layers implanted at (a) a dose of 2.5×10^{17} and ion energy of 75 keV and (c) a dose of 5.0×10^{17} and ion energy of 100 keV. The corresponding SAD patterns collected from the nanocrystal (NC) layer of (a) and (c) are presented in (b) and (d), respectively.

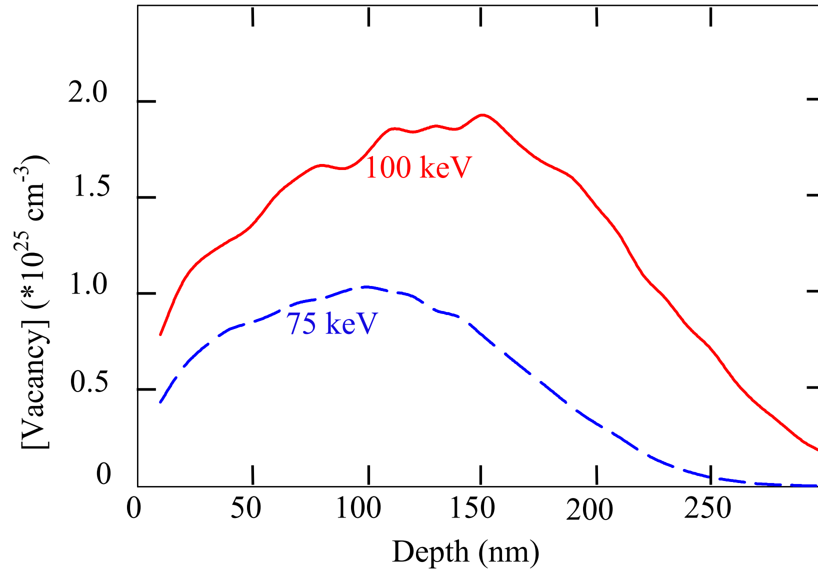

Fig. 4.3 SRIM simulations of vacancy concentration vs. implantation depth following N^+ implantation at 100-keV (solid) and 75-keV (dashed). The predicted maximum vacancy concentration for 100-keV implantation is approximately twice that for 75-keV implantation.

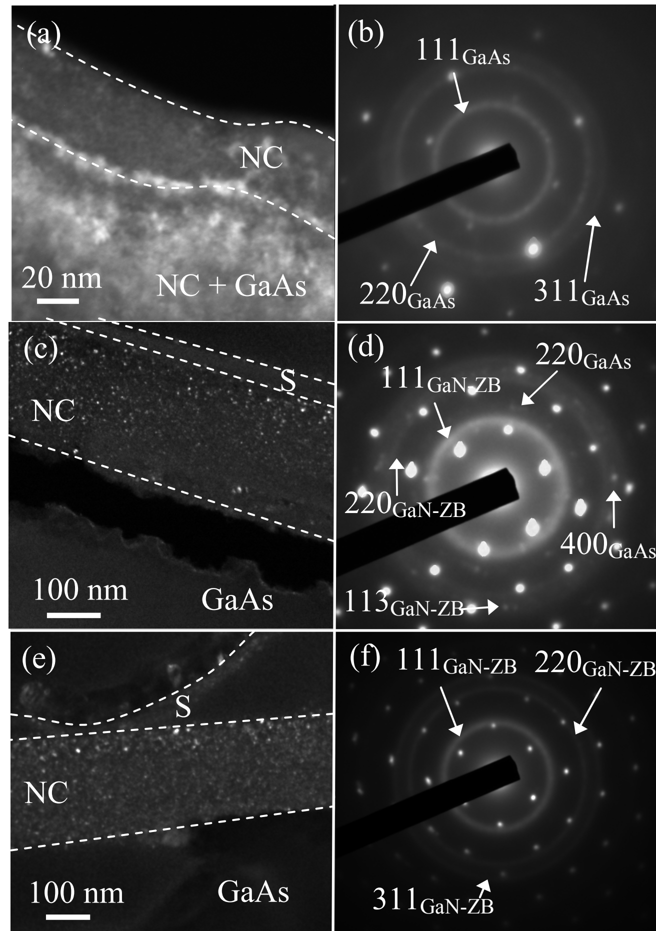

Fig. 4.4 Dark-field TEM images of implanted-plus-annealed GaAs:N layers following RTA for 30 s at (a) 600ºC (c) 650ºC and (e) 900ºC. The corresponding SAD patterns collected from the nanocrystal (NC) layer of (a), (c), and (e) are presented in (b), (d), and (f), respectively.

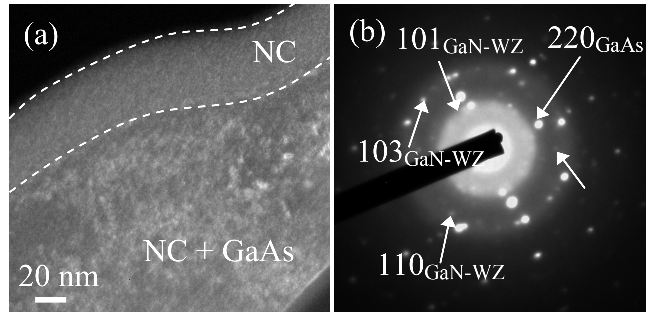

Fig. 4.5 Dark-field TEM of GaAs:N following furnace annealing at 650ºC for 10 minutes. The corresponding SAD pattern, presented in (b), indicates nucleation of WZ GaN.

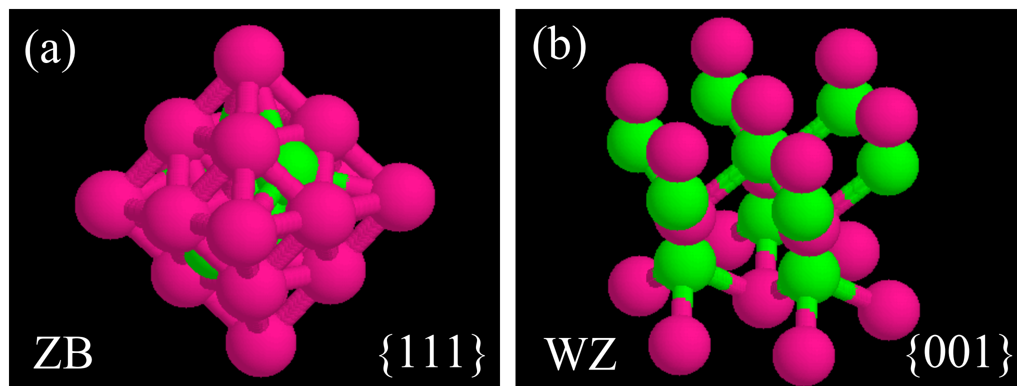

Fig. 4.6 Models of (a) ZB and (b) WZ GaN. Close packed surface planes are indicated in pink. A higher density of close packed {111} surface planes for ZB nanocrystals in comparison to the {001} close packed surface planes of WZ is apparent.

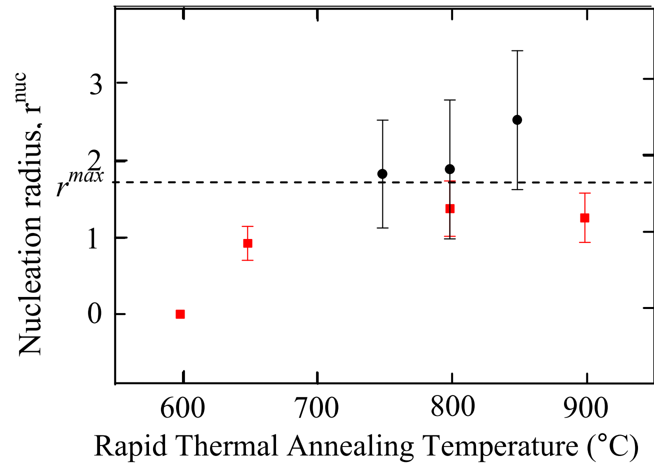

Fig. 4.7 Plot of GaN nanocrystal size at nucleation vs. annealing temperature for rapid thermal annealed GaAs:N. Data contained in this thesis (squares) and data from Ref. 8 (circle) suggests that size increases with anneal temperature from 650 to 800°C, reaching a maximum size of 1.75 nm, as shown by the dashed line.

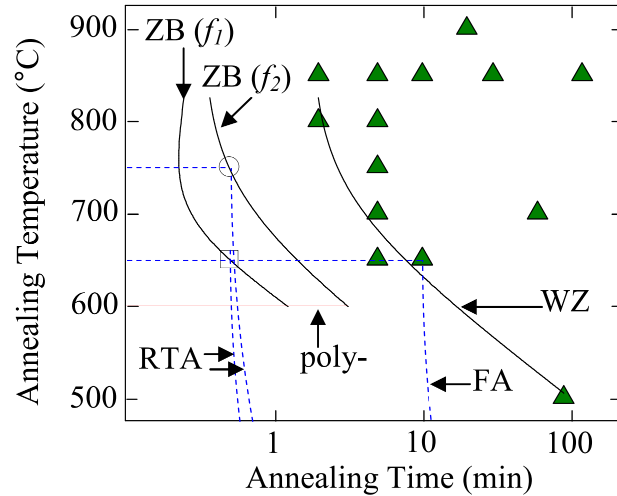

Fig. 4.8 TTT diagram for ZB and WZ GaN formation based upon literature reports and data contained in this thesis. WZ GaN nucleation is indicated by triangles. Annealing paths for select RTA and FA temperatures are overlaid for comparison (dashed lines). For RTA at 650°C for 30 s, formation of ZB GaN (square) is observed. During the subsequent quench to RT, formation of polycrystalline GaAs is also observed. For RTA at 750°C for 30 s, formation of ZB GaN begins at 14 s; polycrystalline GaAs is not observed following the quench to RT. In the case of FA at 650°C for 10 min, formation of WZ GaN is observed and subsequent quenching to RT does not lead to the formation of polycrystalline GaAs.

4.10 References

[1] K.C. Lo, H.P. Ho, K.Y. Fu, P.K. Chu, K.F. Li, and K.W. Cheah, *J. Appl. Phys*. **95**, 8178 (2004).

[2] Y.G. Li, A.T.S. Wee, C.H.A. Huan, and J.C. Zheng, *Appl. Surf. Sci*. **174**, 275 (2001).

[3] S. Dhara, P. Magudapathy, R. Kesavamoorthy, S. Kalavathi, K.G.M. Nair, G.M. Hsu, L.C. Chen, K.H. Chen, K. Santhakumar, and T. Soga, *Appl. Phys. Lett*. **87**, 261915 (2005).

[4] X.W. Lin, M. Behar, R. Maltez, W. Swider, Z. Liliental-Weber, and J. Washburn, *Appl. Phys. Lett*. **67**, 2699 (1995) .

[5] H.J. Kim, T.G. Andersson, J.-M. Chauveau, and A. Trampert, *J. Appl. Phys*. **94**, 7193 (2003).

[6] H.J. Kim, T.G. Andersson, J.-M. Chauveau, and A. Trampert, *Appl. Phys. Lett*. **81**, 3407 (2002).

[7] X. Weng, W. Ye, S. J. Clarke, V. Rotberg, A. Daniel, R. Clarke, and R. S. Goldman, *J. Appl. Phys.* **97**, 064301 (2005).

[8] X. Weng, S. J. Clarke, W. Ye, S. Kumar, A. Daniel, R. Clarke, J. Holt, J. Sipowska, A. Francis, V. Rotberg, and R. S. Goldman, *J. Appl. Phys*. **92**, 4012 (2002).

[9] Z. Majlinger, A. Bozanic, M. Petravic, K. J. Kim, B. Kim, and Y. W. Yang, *J. Appl. Phys.* **104**, 063527 (2008).

[10] L. A. Delouise, *J. Vac. Sci. Technol. A* **11**, 609 (1993).

[11] J. D. Hecht, F. Frost, D. Hirsch, H. Neumannm A. B. Preobrajenski, T. Chassé, and A. Schindler, *J. Appl. Phys.* **90**, 6066 (2001).

[12] A. H. P. Ho, D. T. K. Kwok, X. C. Zeng, C. Chan, and P. K. Chu, *Surf. Coatings Technol.* **136** (2001).

[13] Š. Meškinis, K. Šlapikas, M. Pucėta, S. Tamulevičius, and J. Matukas, *Vacuum* **77**, 79 (2004).

[14] B. Boudart, J. C. Pesant, J. C. de Jaeger, and P. A. Dhamelincourt, *J. Raman Spectrosc.* **31**, 615 (2000).

[15] V. Baranwal, R. Krishna, F. Singh, A. Tripathi, A. C. Pandey, and D. Kanjilal, *Appl. Surf. Sci*. **253**, 5317 (2007).

[16] S. S. Hullavarad, S. V. Bhoraskar, S. R. Sainkar, S. Badrinarayanan, A. B. Mandale, and V. Ganesan, *Vacuum* **55**, 121 (1999).

[17] I. T. Bae, W. Jiang, C. Wang, W. J. Weber, and Y. Zhang, *J. Appl. Phys.* **105**, 083514 (2009).

[18] L. A. Giannuzzi, J. L. Drown, S. R. Brown, R. B. Irwin, and F. A. Stevie, *Micros. Res. & Tech*. **41,** 285 (1998).

[19] X. Weng, W. Ye, J. C. Mabon, and R. S. Goldman, *J. Vac. Sci. Technol. B* **22**, 989 (2004).

[20] A. W. Wood, R. R. Collino, B. L. Cardozo, F. Naab, Y. Q. Wang, and R. S. Goldman, *J. Appl. Phys.* **110**, 124307 (2011).

[21] M. Leszczynski, in *Properties, Processing and Applications of Gallium Nitride and Related Semiconductors*, edited by J.H. Edgar, S.T. Strite, I. Akasaki, H. Amano, and C. Wetzel (INSPEC, London, UK, 1999), p.3.

[22] A. W. Wood, X. Weng, Y. Q. Wang, and R. S. Goldman, *Appl. Phys. Lett*. **99**, 093108 (2011).

[23] M. H. Niglari, C. M. Brakman, E. J. Mittemeijer, and S. Van ded Zwaag, *Metallurgical Mater. Trans. A* **26**, 765 (1995).

[24] L.A. Delouise, *J. Vac. Sci. Technol. A* **10**, 1637 (1992).

[25] T. Makimoto and N. Kobayashi, *Appl. Phys. lett*. 67, 548 (1995).

Chapter 5

Spatially Directed Formation of Embedded Zincblende GaN Nanocrystals

5.1 Overview

Ion beam synthesis approaches have been utilized to produce both ZB and WZ nitride nanocrystals.[1,2] However, a method for spatially directing the nucleation of nitride nanocrystals has not been reported. This chapter opens with background information on earlier approaches to spatially direct nanostructure nucleation via FIB processing. Next, the experimental details of these investigations are described. We then discuss the influence broad-area ion implantation combined with FIB irradiation on the nucleation of ZB vs. WZ GaN and vertical and lateral positioning of the GaN nanocrystals. The correlation between nanocrystal size at nucleation and nanocrystal phase are investigated, and a preference for ZB GaN nucleation is observed for small nanocrystal radii. The chapter concludes with a summary.

5.2 Background

To exploit the desired characteristics of both ZB and WZ GaN, an understanding of the mechanisms for selective phase nucleation is essential. The preference for ZB vs.

WZ GaN may be related to nanocrystallite strain,[3] the relative stability of the small size of WZ and ZB nanocrystals,[4] or the influence of short-to-medium range order in the host matrix. To date, the mechanisms of ZB vs WZ GaN nucleation in GaAs:N has not been explored experimentally.

In terms of lateral patterning of nanocrystals, focused ion beam (FIB) milling has been used to produce sites for selective nucleation of Ge islands on Si(001),[5] Cu_2O nanodots on $SrTiO_3(100)$,[6] and InP nanowires on GaAs(100).[7] In addition, it has been proposed that FIB-induced vacancy motion would enable void organization in broad-area implanted GaSb and InSb.[8] In this thesis, we report on the influence of combined broad-area and FIB irradiation, followed by rapid thermal annealing (RTA), on the phase selection and lateral patterning of nitride nanocrystals embedded in GaAs. Following N^+ implantation plus RTA, ZB GaN nanocrystals are observed to be centered about the depth of maximum ion damage. Additional Ga^+ FIB irradiation leads to selective lateral positioning of the nanocrystals in localized regions of highest vacancy concentration. The preferential nucleation of ZB GaN nanocrystals over the thermodynamically favored WZ phase of bulk GaN is consistent with the predictions of a thermodynamic model for the size-dependence of nucleation for ZB GaN.

5.3 Experimental Details

For these investigations, GaAs films were broad-area implanted using 75 or 100 keV N^+ ions, with a nominal fluence of 2.5×10^{17} or 5×10^{17} cm^{-2}, respectively. Following broad-area implantation, trenches with widths and depths of 25 to 50 nm and spacings of

150 to 200 nm were milled into the surface using a Ga^+ FIB operating at 30 kV. The samples were then annealed via RTA in argon gas at 800°C for 30 s, as described in Section 2.3. Cross-sectional TEM samples, oriented perpendicular to the length of the FIB-milled trenches, were prepared using FIB liftout[9] as shown in Fig. 5.1 and described in Section 2.4. The depth-dependence of lattice disorder was determined by channeling-Rutherford backscattering spectrometry (RBS) with a 2 MeV He^{++} beam.

5.4 Depth-Dependence of Ion Damage

We first consider the influence of vacancy concentration on the depth distribution of nitride nanocrystal formation in GaAs. Figures 5.2(a) and 5.2(b) present dark-field TEM images of typical layers formed by 75 and 100 keV implantation-and-RTA. Figures 5.2(a) and 5.2(b) also contain overlaid plots of depth versus vacancy concentration and N concentration, as predicted by SRIM. The cavities in the TEM images, labeled with arrows, are likely remnants of coalesced N gas bubbles at the depths of highest N concentration, similar to earlier reports.[10,11] Simulations of 75 keV (100 keV) N^+ implantation predict maximum vacancy and N concentrations at depths of 100 (150) and 160 (200) nm, respectively. For 100 keV as-implanted GaAs, the maximum vacancy concentration is ~1.9×10^{25} cm^{-3}, compared to ~1.0×10^{25} cm^{-3} for the case of 75 keV as-implanted GaAs. In both cases, a surface layer containing a high density of GaN-rich GaAsN nanostructures within an amorphous matrix, centered about the predicted depth of maximum vacancy concentration, is observed. This suggests that lattice damage

provides sites for nanocrystal nucleation, similar to the nucleation of InAs nanocrystals.[12,13,14]

To determine the influence of broad-area N^+ implantation energy and RTA on damage depth profiles, (001) channeling-RBS measurements were performed on 75 and 100 keV N^+ implanted GaAs. Figure 5.3 presents the normalized yield versus energy and depth for 75 and 100 keV as-implanted and implanted-and-RTA GaAs. For comparison, random and (001) channeling yields from GaAs are included in the plot. The ratio of the channeling RBS yield to the random yield (χ) is a measure of the fraction of ions which were dechanneled, presumably due to lattice disorder. For 100 keV (75 keV) as-implanted GaAs, the normalized yield contains a broad peak spanning depths from 0 to 300 nm (0 to 250 nm). The presence of this peak indicates an increase in lattice disorder in the range of depths including those of the highest vacancy concentration and the highest nitrogen concentration, indicated with brackets in Fig. 5.3. For depths to 300 nm, the normalized yield is an average of 32% higher for 100 keV in comparison with that of 75 keV as-implanted GaAs, suggesting a higher vacancy concentration following 100 keV implantation, consistent with the predictions of SRIM simulations discussed above. Following RTA, the normalized yield of the 100 keV (75 keV) implanted GaAs is reduced, indicating partial recovery of crystallinity. For 100 keV (75 keV) implanted GaAs, the normalized yield contains a local minimum from 0 to 150 nm (0 to 100 nm), consistent with the predicted depth of maximum vacancy concentration and the observed depth of nanocrystal formation. This indicates that the nanocrystal formation indeed takes place at the depth of highest vacancy concentration. We therefore endeavor to use FIB irradiation to create laterally directed seeding locations for nanocrystal formation.

This process of *directed* matrix seeding is shown schematically in Fig. 5.4. Following broad-area N^+ implantation (5.4(a)), the surface is FIB-irradiated in specific areas to increase the localized vacancy concentration (5.4(b)), and finally, the thermal annealing induces the formation of nanocrystals in the FIB-irradiated regions (5.4(c)).

5.5 Nucleation of ZB Nitride Nanocrystals

We also consider the nanoscale structure following broad-area implantation, FIB processing, and RTA. Figure 5.5 presents typical dark-field diffraction contrast TEM images after (a) 75 keV implanted-plus-FIB-and-RTA and (c) 100 keV implanted-plus-FIB-and-RTA. Both TEM images reveal a series of hills and valleys associated with the FIB-milled trenches, along with two distinct regions below the Pt layer: (1) a nanocrystal bilayer with a ~20 nm thick surface layer and a 250 nm thick nanocrystal middle layer, and (2) a near-substrate layer. For both implantation energies, nanocrystal formation within the bilayer occurs, similar to the nanocrystal layer formed via matrix-seeded growth.[11] Within the nanocrystal bilayer of the implanted-plus-FIB-and-RTA samples, the thickest layer contains nanocrystals in an amorphous matrix. The nanocrystals have an average radius of 1.04±0.53 (75 keV) and 1.37±0.36 (100 keV) nm.

Identification of nanocrystals was performed using SAD collected from the bilayer following 75 keV and 100 keV implantation-plus-FIB-and-RTA, as shown in Figs. 5.5(b) and 5.5(d), respectively. Both SAD patterns contain several spotty rings associated with the nanocrystals and a diffuse ring, presumably due to the amorphous regions. Comparisons of the interplanar spacings measured by SAD and the powder

diffraction standards from GaAs and GaN are shown in Table 5.1. For the 75 keV (100 keV) implanted-plus-FIB-and-RTA nanocrystal bilayer, d-spacings of 3.26, 2.00, 1.71, 1.41 and 1.30 Å (3.26, 2.00, 1.71, 1.39 and 1.31 Å) are observed, within 1.4% of the {111}, {220}, {311}, {400} and {331} interplanar spacings of GaAs. Additionally, d-spacings of 2.56 Å (2.59 and 1.62 Å) are apparent, within 1.9% of the {111} ({111} and {220}) interplanar spacings of ZB GaN. The {220} reflection of ZB GaN is likely missing for the 75 keV case due to the low density of GaN nanocrystals. Fewer nanocrystals are apparent following 75 keV implantation in comparison with that of 100 keV implantation plus RTA. It is likely that fewer nanocrystal nucleation sites were formed due to the lower vacancy concentration for the 75 keV case, as shown in Fig. 5.2. For both implantation energies, the {111} reflections of ZB GaN are evident while the {100} reflections of WZ GaN are absent, indicating a preferential nucleation of ZB. It is interesting to note that the ZB phase has formed following both 75 and 100 keV implantation-plus-FIB-and-RTA, although WZ is predicted to be the most stable thermodynamically.[15] The mechanisms for the nucleation of ZB GaN over WZ GaN will be discussed in Section 5.7.

5.6 Directed Seeding of GaN Nanocrystals

We next consider the influence of FIB irradiation on the spatially-directed nucleation of nanocrystals. Figure 5.5 presents typical dark-field diffraction contrast TEM images after (a) 75 keV implanted-plus-FIB-and-RTA and (c) 100 keV implanted-plus-FIB-and-RTA that reveal a nanocrystal bilayer. Within the narrowest layer of the

bilayer, it appears that many ~10-15 nm-sized agglomerations of nanocrystals have formed within a ~20 nm amorphous layer at the surface. The thickness of the amorphous layer is consistent with SRIM simulations of the depth of highest vacancy concentration introduced by 30 keV Ga^+ FIB irradiation, as shown in Fig. 5.6. The agglomerations of nanocrystals have nucleated near the FIB-irradiated trenches, suggesting a preference for nucleation in regions of increased vacancy concentration.

For both 75 and 100 keV broad-area implantation energies, we consider the influence of FIB irradiation on the percentage of preferentially aligned nanocrystals within the nanostructured bilayer. In the vicinity of the FIB-irradiated regions, similar densities of agglomerations of nanocrystals are apparent following implantation-plus-FIB-and-RTA for both implantation energies. However, a comparison of the FIB-irradiated regions reveals a lower density of randomly spaced nanocrystals in the 75 keV bilayer, presumably due to a lower vacancy concentration in that case. The comparison of vacancy concentrations for the 75 and 100 keV as-implanted GaAs is shown in Figs. 5.2(a) and 5.2(b), respectively. Since the 75 keV implantation leads to ~50% fewer vacancies in comparison to that of the 100 keV implantation, fewer available nucleation sites are expected to be available in that case. Thus, subsequent FIB irradiation is expected to provide the greatest selectivity for the 75 keV implanted-plus-FIB-and-RTA films.

5.7 Mechanisms for ZB GaN Nucleation

The proposed mechanism for nucleation following broad-area implantation, FIB processing, and RTA is shown schematically in Fig. 5.7. The implantation of GaAs with high energy N^+ ions produces a N super-saturated surface layer, as shown in Fig. 5.7(a). Subsequently, exposure of the GaAs:N surface to localized FIB irradiation introduces regions of increased vacancy concentration which act as nanocrystal nucleation sites (Fig. 5.7(b)). Following annealing, a nanostructured bilayer is formed at the surface, as shown in Fig. 5.7(c).

We examine the size-dependence of nanocrystal phase (ZB vs. WZ) by considering the free energy for the nucleation of ZB and WZ GaN. The nanocrystals form in an amorphous matrix; thus, strain is not expected to play a role in their nucleation. Therefore, we assume an unstrained spherical solid nucleating from a liquid. A detailed calculation of free energy for the formation of nanocrystalline GaN is presented in Appendix C.

The resulting difference in free energies, ΔG_{ZB}-ΔG_{WZ}, as a function of nanocrystal radius, is shown in Fig. 5.8. For implantation-plus-RTA, ZB GaN is favored when $r < 2.10$ Å. For small r, the reduction in free energy of the ZB phase in comparison with the WZ is driven by a minimization of the GaN surface energy. Indeed, the surface energy is minimized by adoption of the ZB crystal structure, which has a higher density of low energy {111} surface planes in comparison with the WZ structure. We note that a more complete calculation of the size-dependence of WZ vs. ZB nanocrystal formation is expected once the enthalpy and interfacial energies of nanoscale GaN are available.

5.8 Conclusions

In summary, we have examined the formation of nitride nanocrystals using a combination of broad-area implantation and FIB processing. GaN nanocrystals form in the regions of highest damage, both vertically and laterally, thus making lateral positioning possible by using FIB patterning to introduce localized regions of increased vacancy concentration. Following RTA, ZB GaN nanocrystals have nucleated instead of the thermodynamically favored WZ phase of bulk GaN. This is consistent with the predictions of a thermodynamic model for nucleation of nano-scale ZB GaN.

d-spacing (Å) (experimental)		Powder diffraction standards (Å)	
75-keV implant.	100-kev implant.	ZB GaN (hkl)	GaAs (hkl)
3.26	3.26		3.26 (111)
2.56	2.59	2.60 (111)	
2.00	2.00		2.00 (220)
1.71	1.71		1.70 (311)
	1.62	1.59 (220)	
1.41	1.39		1.41 (400)
1.30	1.31		1.30 (331)

Table 5.1 A comparison of the interplanar distances measured by selected area diffraction of GaAs:N following RTA at 550 and 600°C with the powder diffraction data for GaAs and GaN.

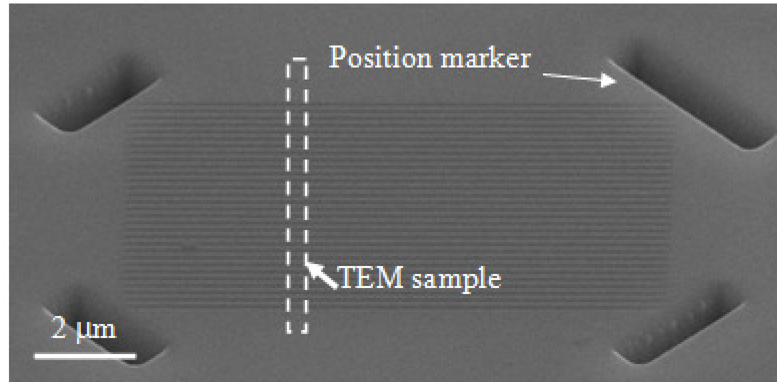

Fig. 5.1 SEM image of FIB-milled trenches in GaAs:N. The trenches act as regions of increased vacancy concentration. FIB liftout techniques were used to create cross sectional TEM samples perpendicular to the trenches (dotted line). Deep trenches were milled for position marking.

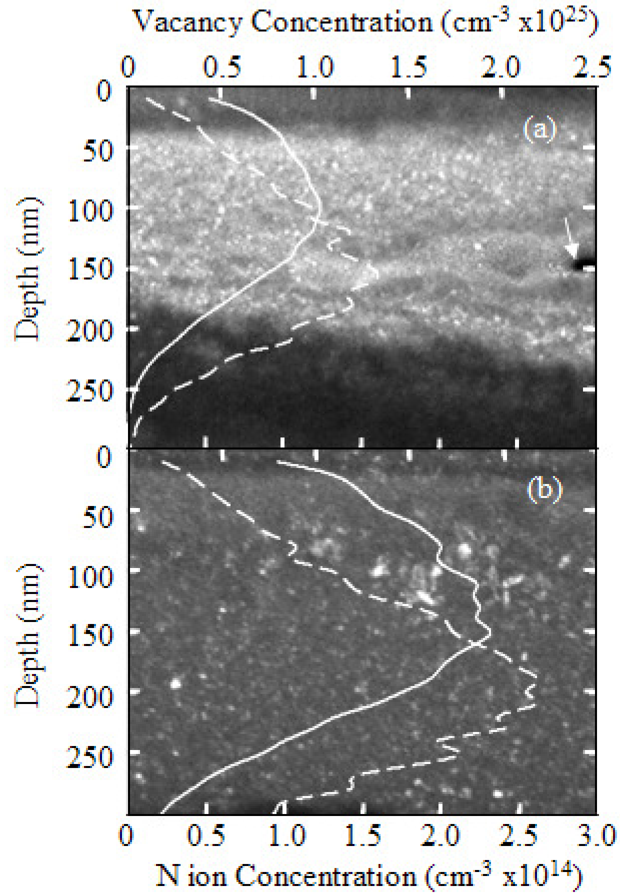

Fig. 5.2 SRIM simulations of the depth-dependence of vacancy and nitrogen concentrations for (a) 75 keV and (b) 100 keV N^+ ions implanted into GaAs overlaid onto dark-field TEM images of implanted-and-RTA GaAs. The regions of highest vacancy concentration (solid line) and highest nitrogen concentration (dashed line) from the simulation correspond to layers with crystallite formation and blistering, as shown in the underlying images.

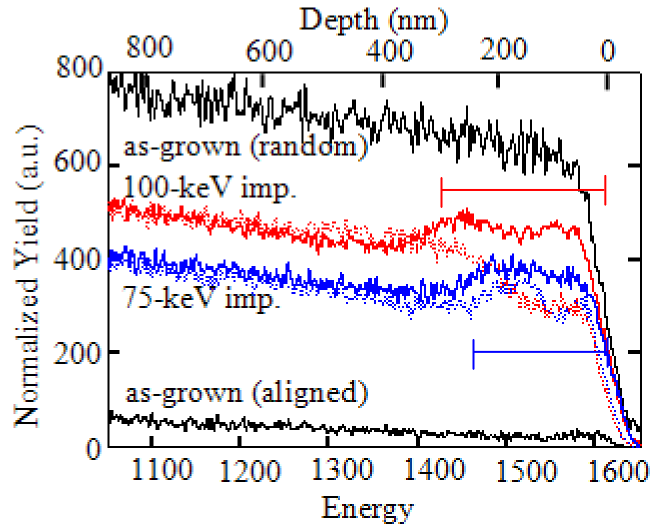

Fig. 5.3 Channeling-RBS spectra as a function of backscattered energy of GaAs layers, comparing 100 and 75 keV as-implanted (solid lines) and implanted-and-RTA (dashed lines) samples with GaAs in the random and (001) aligned configurations. For the 75 keV (100 keV) as-implanted layer, a broad peak which spans depths from 0 to 250 nm (0 to 300 nm), indicated by brackets, is observed. Following RTA, minima from 0 to 150 nm (0 to 100 nm) indicate partial recovery of the lattice damage, at depths corresponding to those where nanocrystal nucleation is observed.

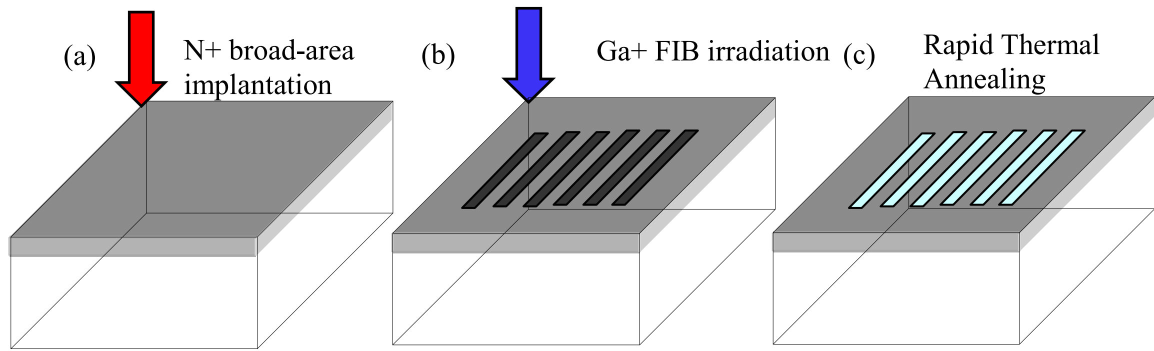

Fig. 5.4 Schematic of the directed matrix seeding process. N+ ions are broad-area implanted into the substrate to create a highly damaged, N-rich surface (a). Ga+ FIB irradiation is used to introduce regions of elevated vacancy concentration (b). Following thermal annealing, GaN is nucleated in the FIB irradiated regions (c).

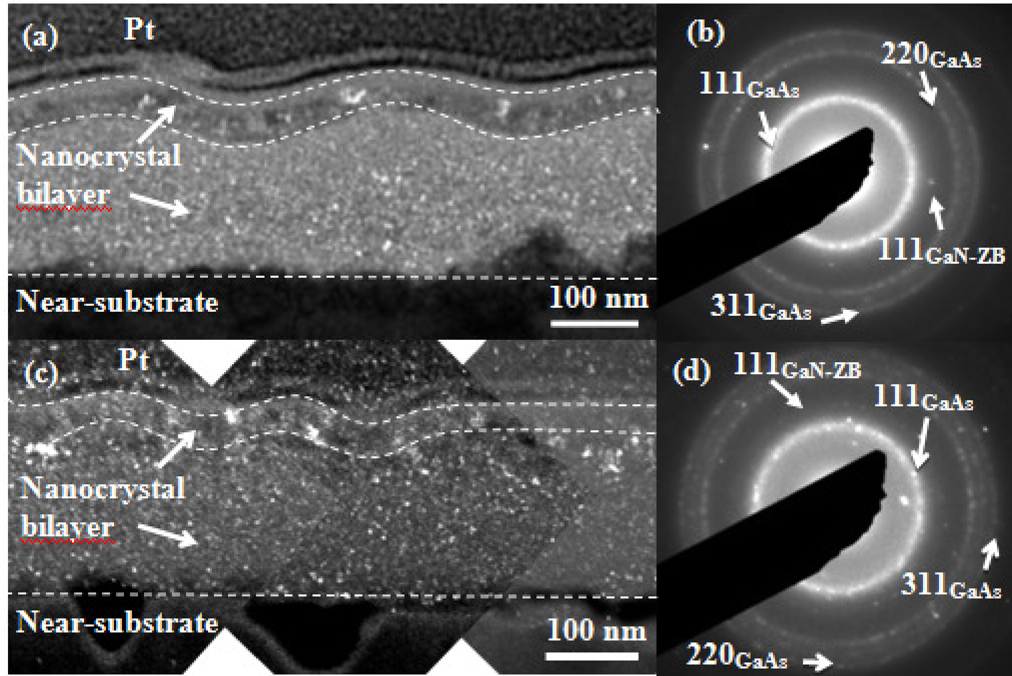

Fig. 5.5 Dark field TEM image of (a) 75 keV and (c) 100 keV implanted-plus-FIB-and-RTA GaAs. Polycrystalline nanocrystals with a clustering of crystallites near the bottom of the FIB milled trenches appear as bright spots in the TEM image. The SAD patterns collected from the polycrystalline layers of (a) and (c), shown in (b) and (d), reveal the formation of ZB GaN in both cases.

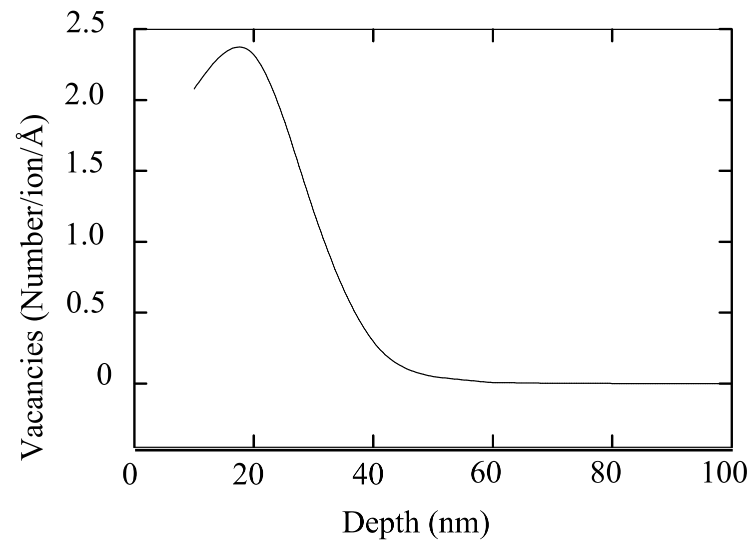

Fig. 5.6 SRIM simulations of 30-keV Ga implanted into GaAs. The vacancy concentration is centered about a depth of ~18 nm.

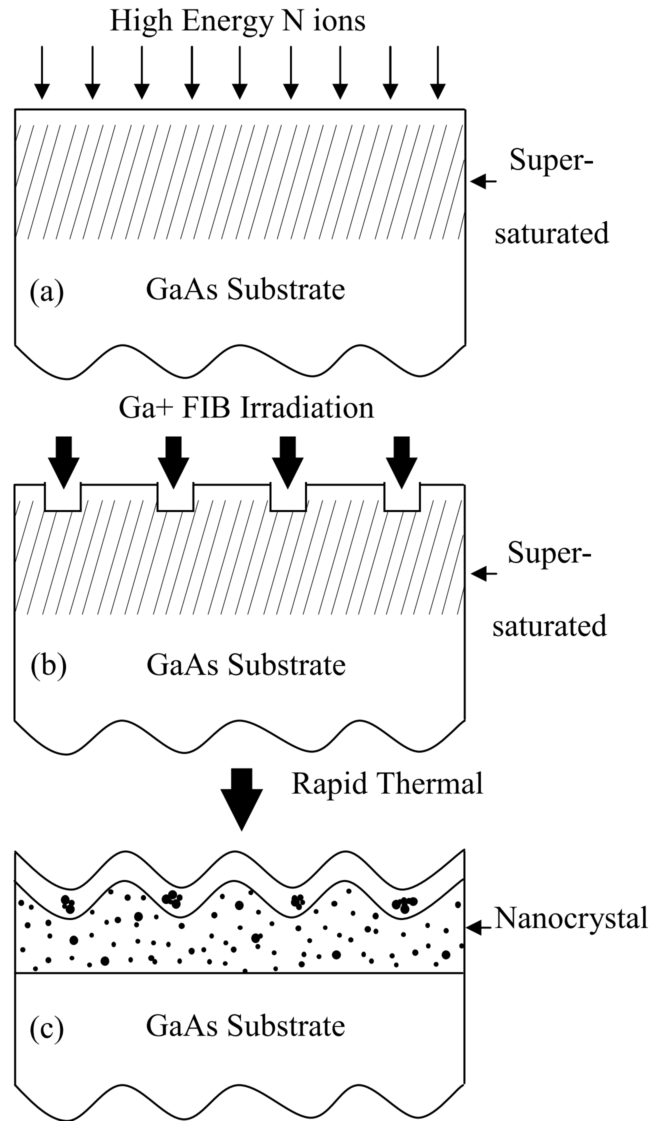

Fig. 5.7 Schematic of the directed matrix seeding process, consisting of (a) broad-area high energy nitrogen ion irradiation to produce a N super-saturated amorphous layer, (b) FIB irradiation to produce arrays of localized high vacancy concentration, and (c) rapid thermal annealing to enable spatially–directed nanocrystal nucleation.

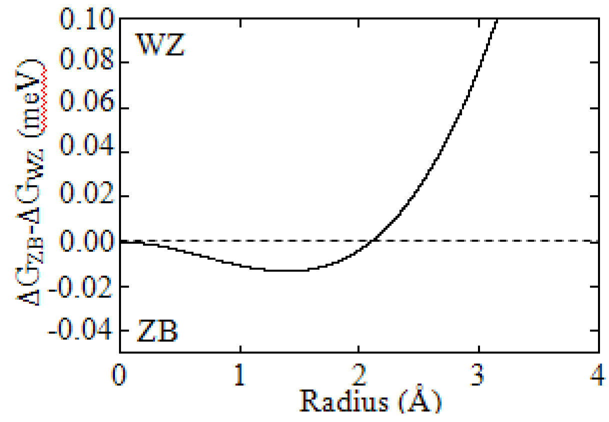

Fig. 5.8 Plot of the difference between the free energies of formation for WZ and ZB GaN following RTA at 800°C. For radii less than 2.10 Å, the ZB phase is thermodynamically favored, while the WZ phase is favored for larger radii.

5.9 References

[1] X. Weng, S. J. Clarke, W. Ye, S. Kumar, R. S. Goldman, A. Daniel, R. Clarke, J. Holt, J. Sipowska, A. Francis, and V. Rotberg, *J. Appl. Phys* **92**, 4012 (2002).

[2] X. W. Lin, M. Behar, R. Maltez, W. Swider, Z. Liliental-Weber, and J. Washburn, *Appl. Phys. Lett*. **67**, 2699 (1995).

[3] T. Ito, K. Shiraishi, and A. Taguchi, *J. Crys. Growth* **227-228**, 366 (2001).

[4] R. Banerjee, R. Jayakrishnan, and P. Ayyub, *J. Phys. Condens. Matter* **12**, 10647 (2000).

[5] M. Kammler, R. Hull, M. C. Reuter, and F. M. Ross, *Appl. Phys. Lett*. **82**, 1093 (2003).

[6] J. F. Groves, Y. Du, I. Lyubinetsky, and D. R. Baer, *Superlattices and Microstructures* **44** , 677 (2008).

[7] J. Ahopelto, H. Lezec and Y. Ochiai, A. Usui, and H. Sakaki, *Appl. Phys. Lett*. **64**, 499 (1994).

[8] N. Nitta and M. Taniwaki, *Nuc. Instr. Meth. Phys. Res. B* **206,** 482 (2003).

[9] L. A. Giannuzzi, J. L. Drown, S. R. Brown, R. B. Irwin, and F. A. Stevie, *Micros. Res. & Tech*. **41,** 285 (1998).

[10] R. R. Collino, B. B. Dick, F. Naab, Y. Q. Wang, M. D. Thouless, and R. S. Goldman, *Appl. Phys. Lett.* **95**, 111912 (2009).

[11] X. Weng, W. Ye, J. C. Mabon, and R. S. Goldman, *J. Vac. Sci. Technol. B* **22**, 989 (2004).

[12] H. D. Fonseca-Filho, C. M. Almeida, R. Prioli, M. P. Pires, P. L. Souza, *J. Appl. Phys.* **107**, 054313 (2010).

---

[13] H. D. Fonseca-Filho, R. Prioli, M. P. Pires, A. S. Lopes, P.L. Souza, and F. A. Ponce, *Appl. Phys. Lett* **90**, 013117 (2007).

[14] C. Taylor, E. Marega, E. A. Stach, G. Salamo, L. Hussey, M. Muñoz, and A. Malshe, *Nanotechnology* **19**, 015301 (2008).

[15] M. Leszczynski, in *Properties, Processing and Applications of Gallium Nitride and Related Semiconductors*, edited by J.H. Edgar, S.T. Strite, I. Akasaki, H. Amano, and C. Wetzel (INSPEC, London, UK, 1999), p.3.

Chapter 6

Summary and Suggestions for Future Work

6.1 Summary

In this thesis, the mechanisms for nucleation of embedded gallium (indium) nitride nanostructures were investigated. We examined the relative roles of implantation energy, annealing time, and annealing temperature on the nucleation and growth of nanocrystals. We presented a thermodynamic model for the size-dependant nucleation of ZB vs. WZ nanocrystals. In addition, we examined the lateral patterning of nanostructures using focused ion beam irradiation.

In Chapter 3, we examined the formation of InN nanocrystals embedded in InAs. Low temperature (77K) N ion implantation into InAs led to the formation of a 200 nm, N-rich, amorphous surface layer with crystalline InAs remnants. RTA up to 550°C led to the nucleation of zincblende InN nanocrystals with a maximum likelihood radius of 1.3±0.2 nm. RTA at 600°C led to nucleation of zincblende and wurtzite InN, with an increase in nanocrystal radius to 2.6±0.4 nm. These results were consistent with the predictions of a thermodynamic model for the nanoscale-size-dependence of zincblende and wurtzite InN nucleation. The thermodynamic model suggests the dominant influence of surface energy on nanocrystal structure for nanocrystals with radii up to ~2 nm.

In Chapter 4, the nucleation and growth of embedded GaN nanostructures was examined. We discussed the influence of parameters critical for controlling the kinetics, including annealing time and annealing temperature. For both high energy (100-keV) and low energy (75-keV) implantations, ZB GaN nucleation was observed. The damage depth distribution was simulated and compared to TEM images, and indicated a higher vacancy concentration for high energy implantations. For annealing temperatures of 650 and 900ºC, ZB GaN was observed following 30 s of annealing. The size of the nanostructures was examined and a maximum radius for pure ZB GaN formation was observed for annealing temperatures greater than 700ºC. Following annealing for 10 min at 650ºC, WZ GaN was observed, indicating that a phase transition from ZB to WZ GaN occurs if the annealing time is sufficiently long. A TTT diagram to describe the nucleation and coarsening of ZB and WZ GaN was developed and presented, allowing for predictions of the annealing conditions for ZB and/or WZ GaN formation at arbitrary temperatures.

In Chapter 5, we reported on the spatially selective formation of GaN nanocrystals embedded in GaAs. Broad-area N^+ implantation followed by RTA led to the formation of nanocrystals at the depth of maximum ion damage. With additional irradiation using a Ga^+ FIB, selective lateral positioning of the nanocrystals within the GaAs matrix was observed in isolated regions of increased vacancy concentration. Following RTA, the formation of ZB GaN is observed in the regions of highest vacancy concentration. There is a higher density of randomly spaced nanocrystals within the FIB-irradiated layer following 100 keV implantation, indicating a greater influence of FIB-irradiation on spatially-directed nucleation following 75 keV implantation. The

nucleation of zincblende nanocrystals over the wurtzite phase of bulk GaN is consistent with the predictions of a thermodynamic model for the nanoscale size-dependence of GaN nucleation.

6.2 Suggestions for Future Work

In Chapters 3-5, we presented methods for controlling the size, crystalline phase, and lateral position of InN and GaN nanocrystals. Embedded GaN or InN nanocrystals were formed via ion implantation followed by thermal annealing. Nanocrystals formed via this method have dimensions (3-5 nm) that are comparable to the sizes achievable with colloidal growth, but are embedded in a protective host matrix and can be laterally spaced, comparable to epitaxial growth methods. However, further work is needed to examine the effect of the nanostructure on the physical properties of the materials. In the following sections, we will discuss three suggestions for future work that will relate the structure of the materials to device performance and present a method of multi-dimensional fabrication. First, we will discuss thermal conductivity measurements of InN and GaN nanostructures. Then, we will discuss photoluminescence of InN and GaN nanocrystals. Finally, we will present a process of extending directed matrix seeding to multiple dimensions.

6.2.1 Thermal Conductivity of Nanostructured Ga(In)As:N

Low-dimensional heterostructures are predicted[1,2] to lead to materials with enhanced thermoelectric figure-of-merit, ZT, in comparison to that of bulk materials. ZT may be defined as:

$$ZT = \frac{S^2 T\sigma}{\kappa} \qquad (6.1)$$

where S is the Seebeck coefficient, σ is the resistivity, and κ is the thermal conductivity. Preliminary measurements of S and σ have been performed. S of as-grown GaAs samples range from 100 and 500 μVK^{-1}, for n ranging from 10^{16} cm^{-3} to 10^{19} cm^{-3} (ref. 3). Following implantation, S could only be measured for heavily-doped implanted-plus-RTA layers; however, the measured S for the heavily-doped-plus-RTA samples is slightly enhanced in comparison to that of the as-grown films. For Si-doped GaAs:N layers, implantation-plus-RTA increases the resistivity, ρ (ρ=1/σ), of two samples from ~0.001 to ~0.01 Ω-cm and ~0.004 to ~0.04 Ω-cm. For Te-doped GaAs:N layer, implantation-plus-RTA increases ρ from ~0.001 to ~0.1 Ω-cm, a much larger increase than that for the Si-doped case.[4] In order to fully characterize ZT, it is necessary to measure κ. In the case of GaAs:N nanocomposite layers, it is likely that phonon scattering due to both the disordered matrix as well as matrix/particle interfaces will contribute to a decrease in κ in comparison to that of the bulk. For example, the addition of ErAs particles to InGaAs layers has been shown to decrease κ by at least a factor of 2.[5]

We have begun studies on the thermal conductivity of GaAs:N nanocomposite films. However, to characterize the correlation between nanostructure and thermal properties, thermal conductivity measurements of both MBE-grown GaAs films and GaAs:N nanocomposite films are suggested. For this purpose, a pump/probe technique[6] shown in Fig. 6.1 is used. A metal film (~50-100 nm) is deposited as a transducer layer

on the sample surface. Then, an optical pulse (pump) laser signal is focused onto the sample surface. The energy of the pulse is deposited in a localized region of the sample surface (r ~15 μm), leading to a localized increase in the temperature. Stress is generated by thermal expansion of the material, and relaxes by generating an acoustic strain pulse. This strain pulse propagates according to the elastic properties of the material and, when an interface is reached, part of the pulse is transmitted and part is reflected according to the difference in the acoustic impedance (product of density and sound velocity) of the two materials. The reflected portion eventually returns to the surface, at which point the strain pulse can be converted back into an optically detectable signal by the piezo-optic effect.[7] The presence of strain alters the optical constants, introducing a change in the reflectivity, ΔR. This change in reflectivity can be monitored by a separate optical pulse (probe). The temperature change is then given by

$$\Delta T(z) = (1-R)\frac{Q}{C(\xi A)}\exp^{-z/\xi} \tag{6.2}$$

where R is the sample reflectivity, Q is the optical pulse energy, C is the specific heat per unit volume, A is the optical spot area, ξ is the optical absorption length, and z is the distance into the sample.[8] Values for the thermal conductivity, κ, can be obtained by

$$\kappa \left.\frac{\partial T_s(z,t)}{\partial z}\right|_{z=0} = -\frac{T_m(t) - T_s(0,t)}{R_K} \tag{6.3}$$

where $T_s(z,t)$ is the temperature of the sample film at depth z and time t, $T_m(t)$ is the temperature of the metal film, and R_K is the thermal-boundary resistance at the interface between the metal film and the sample.[9] Details of this derivation can be found in Appendix D.

To date, we have performed pump/probe reflectivity measurements on structures with 175-220 nm layers of N-saturated, highly damaged GaAs matrix. We have also performed measurements on a 220 nm layer consisting of ZB GaN nanocrystals within a highly damaged GaAs matrix. Preparation of these nanostructured films was discussed in Section 4.3. Preliminary thermal conductivity measurements of 75 keV as-implanted, 100 keV as-implanted, and 100 keV implanted-plus-RTA GaAs are presented in Fig. 6.2. Following implantation of GaAs at 75 keV (100 keV), the thermal conductivity is 18 W/mK (16 W/mK). Following annealing, the thermal conductivity increases to a value of 24 W/mK. Thus, the nanostructured films exhibit a thermal conductivity between that of bulk GaAs (55 W/mK) and that of amorphous GaAs (0.5 W/mK).

6.2.2 Photoluminescence of Ga(In)N Nanocomposites

The N-incorporation induced bandgap reduction of GaAs is attractive for applications including photovoltaics as well as long-wavelength light emitters and detectors.[10] For example, photomixers fabricated on N-implanted GaAs showed improvements in power output and responsivity in comparison to as-grown GaAs.[11] In recent years, several groups have explored the optical properties of ion-beam synthesized GaAs:N.[11,12,13,14,15] The PL and CL responses of GaAs:N layers consistent with the preparation described in Chapter 2 are presented in Refs. 15 and 16. PL features, including the ~1.5 eV emission associated with the fundamental band gap transition of GaAs, as well as a ~1.27 eV emission associated with nitride-rich nanocrystals are observed.

Reports on the PL response of InN nanoparticles are limited and do not describe the influence of nanoparticle size on the optical properties. InN nanoparticles synthesized on amorphous silica nanoparticles[17] or on TiO_2 (ref. 18) showed blue emission, although the origin of the emission was attributed to the interface between the InN nanoparticle and the host material rather than a fundamental property of the InN nanoparticles. Additional PL measurements on InN nanoparticles have exhibited broad emission peaks ranging from 1.92 to 2.19 eV, attributed to overlapping bands of ZB and WZ InN.[19] PL emission of InN nanorods was measured as a function of nanorod length with negligible change in the PL response for nanorod lengths of 0.25-1.8 μm.[20] However, the influence of the radial dimensions of the nanorods were not considered. There have been no reports of optical properties of ion-beam-synthesized InAs:N.

Studies of the PL response of InN and GaN nanocrystals as a function of nanocrystal size and phase, and studies in which the spot size of the laser is systematically varied are suggested. If the spot size of the focused point is comparable to the mean separation distance between the nanocrystals, the number of nanocrystals contributing to the PL response is limited and sharp luminescence lines with discrete photon energies are detected. If the distribution of the dots is dilute enough, response from a single nanoparticle may be detected.[21] Thus, the PL response of single nanoparticles and groups of nanoparticles (with some size distribution) can be compared. By varying the size and phase of the nanoparticles, a direct correlation between the nanoparticle structure and PL response can be observed. For the suggested PL measurements, a suitable laser and detector must be employed which can measure the bandgaps of ZB and WZ GaN; 3.2 and 3.39, respectively.

6.2.3 Directed Matrix Seeding in 3-D

In Chapter 5, we described a process for laterally controlling the distribution of nitride nanocrystals by introducing localized regions of increased vacancy concentration. However, the broad-area implantation techniques produce a nanocrystal layer spanning a depth of ~250 nm. On the other hand, the directed seeding was confined to a ~20 nm surface layer corresponding with the depth of FIB irradiation. The randomly spaced nanocrystals therefore span a depth ~10X greater than the spatially directed nanocrystals. Any effect on the properties arising from the ordered surface layer would likely by superseded by a much larger contribution from the random layer. Additionally, the directed seeding process described in this thesis has been achieved only for nanotrenches, limiting patterning applications to one dimension. It is therefore necessary to develop a procedure for introducing a multi-dimensional ordered array of nanocrystals without introducing a disordered layer beneath it. We suggest several approaches, outlined below: reducing the broad-area implantation energy, use of a plasma source FIB, and two dimensional FIB patterning integrated with 3-D growth techniques.

First, we consider reducing the broad-area implantation energy so that maximum vacancy and nitrogen concentration depths are comparable to the maximum vacancy concentration from FIB irradiation. Figure 6.3 presents a plot of FIB-induced vacancy concentration as a function of depth, as predicted by SRIM. The maximum vacancy concentration is at a depth of ~ 18 nm, with a FWHM spanning ~ 30 nm. In order to limit nanocrystal nucleation to these depths, broad area implantation should introduce a

distribution of N with similar depths. Figure 6.4 presents a plot of nitrogen concentration as a function of depth, as predicted by SRIM. As the implantation energy is reduced, the maximum concentration is at shallower depths, and the distribution is reduced. For 10 keV implantations, the [N] has a maximum at ~ 20 nm, with a FWHM spanning ~ 40 nm. This overlaps well with the vacancy concentration introduced by FIB irradiation, which would reduce unnecessary damage in the sample caused by broad-area irradiation at depths beyond the span of FIB-irradiation depths.

Next, we consider the use of a plama-source FIB as a N source. Plasma-source FIB technology is currently in development, with reports of Xe (refs. 22, 23) and Ar (ref. [24]) sources with 1.4 μm spot sizes and current densities of 600 mA/cm^2. Plasma-source FIBs offer an opportunity to combine N implantation with localized vacancy concentration. By using a FIB as a N implantation source, increased vacancy and N concentrations can be introduced simultaneously, as shown schematically in Fig. 6.5. The plasma source N FIB would be used to selectively pattern the surface of the Ga(In)As, with the resolution and current densities afforded by the FIB. Using this procedure, no further ion-beam processing is necessary. Following FIB implantation, the sample would then be annealed to nucleate nitride nanocrystals in the FIB-irradiated areas. Because the implantations could be performed in localized regions, this process also offers the ability to nucleate nanocrystals without damaging the entire sample and limit the introduction of N to only the nanocrystal nucleation sites.

Finally, we consider methods for extending directed matrix seeding to multiple dimensions. To date, the directed seeding process described in this thesis has been achieved for nanotrenches, limiting patterning applications to one dimension. However,

this process is readily expanded to 2-D, as presented in Fig. 6.6. Following broad-area implantation, the sample surface would be patterned using a Ga-source FIB. Following annealing, the FIB-irradiated regions act as seeding locations for nanocrystal nucleation. Because the nanocrystals are embedded, they are not subject to atmospheric degradation and can therefore be integrated with in-situ or ex-situ techniques to integrate 2-D patterns with 3-D growth techniques. An approach of in-situ FIB-MBE for 3-D directed matrix seeding is presented in Fig. 6.7. A Ga(In)NAs film is grown on the substrate using conventional MBE techniques. The surface is then FIB-irradiated using a UHV FIB mounted directly on the growth chamber.[a] The sample should then be annealed using a substrate heater to form nitride nanocrystals. The annealing time and temperature should be adjusted to those found in Chapters 3-5 for the selected growth of ZB or WZ nitride nanocrystals. The film growth, implantation and anneal sequence should then be repeated until the desired dimensions are achieved.

---

[a] For the case a FEI UHV Magnum 4.5" FIB mounted on a Riber 32P MBE system, mounting the FIB on the top 6" flange is recommended. However, modifications must be made to the existing Riber 32P cryopanel to allow placement of electron detector used for FIB imaging.

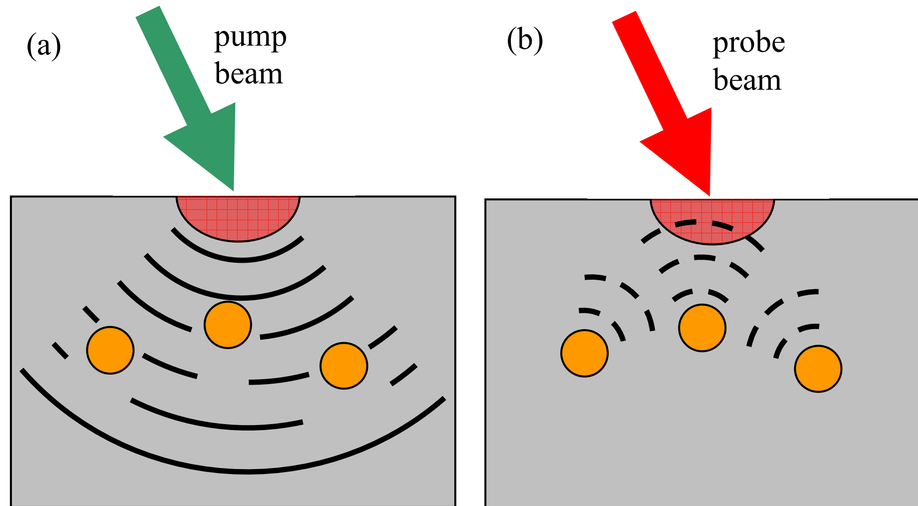

Fig. 6.1 Schematic of pump/probe thermal conductivity measurements. An optical signal (pump) hits the surface (a), creating a localized region of increased temperature (red). A stress pulse (black) is generated by the thermal expansion of the material. The pulse is (b) reflected off of interfaces in the material (orange), where it returns to the origin and the stress alters the reflectivity, which is measured with a probe beam.

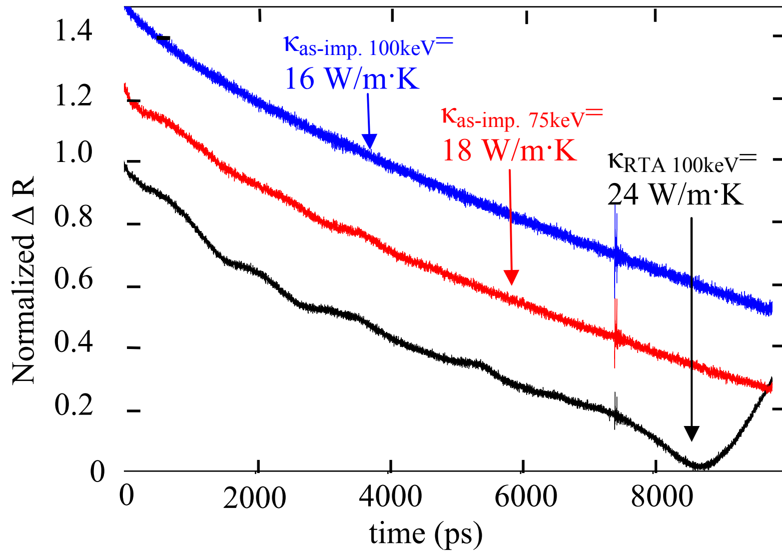

Fig. 6.2 Time-resolved thermoreflectance of GaAs:N obtained using a pump/probe technique. The thermal conductivity is lowest for high energy (100 keV) implantation, with a slight increase following RTA. All values are below those of bulk GaAs (55 W/mK).

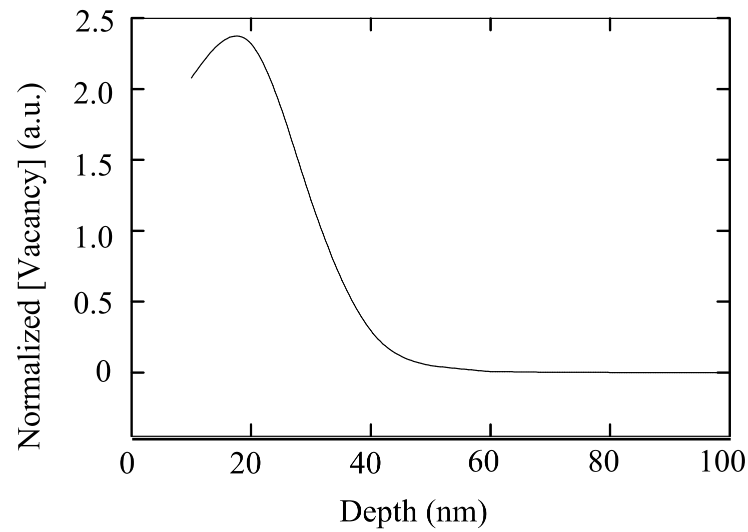

Fig. 6.3 SRIM simulation of vacancy concentration introduced by 30 keV Ga incident on GaAs. For 3-D growth, the vacancy distribution should span depths similar to the nitrogen distribution from broad-area implantation.

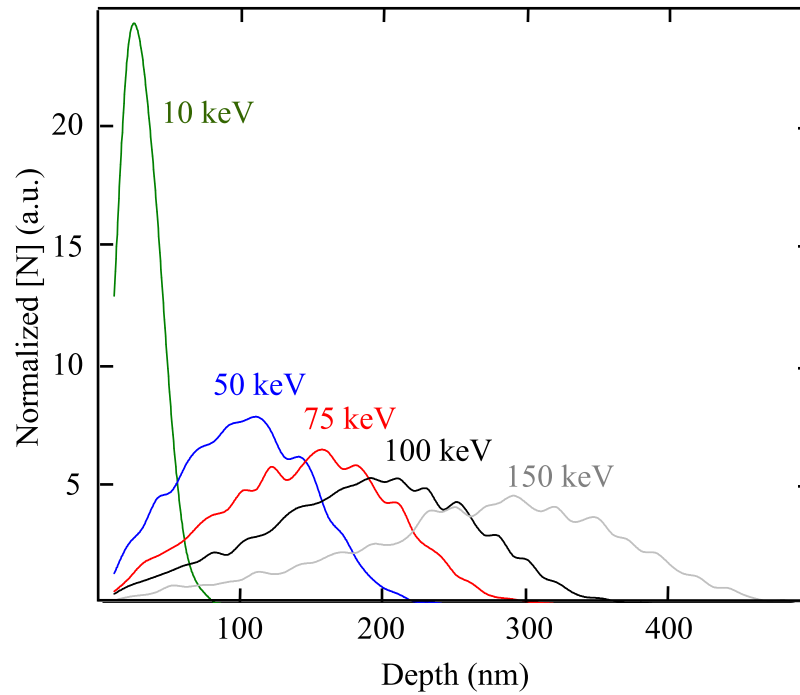

Fig. 6.4 SRIM simulation of N concentration as a function of depth for broad-area N implantation into GaAs for various implantation energies. As implantation energy is reduced, the depth distribution of [N] is reduced. For 10-keV implantation, the maximum [N] is at a depth of ~20 nm.

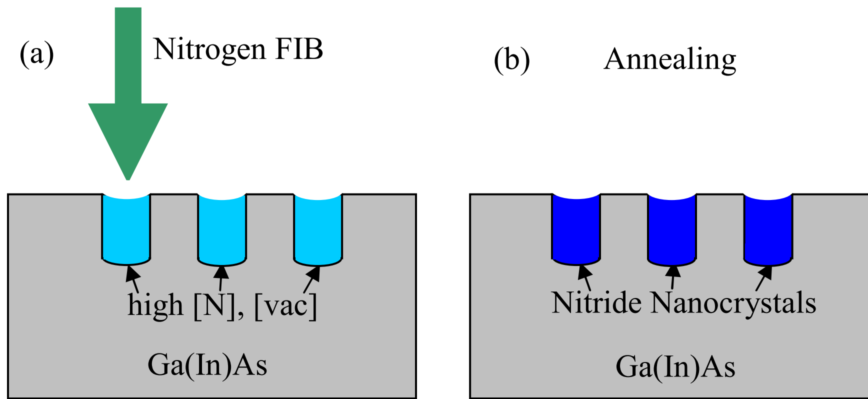

Fig. 6.5 Schematic of the proposed directed seeding process using plasma-source FIB processing. A N FIB (a) is used to selectively pattern a surface with regions of high nitrogen and vacancy concentrations. Thermal annealing (b) would then be used to nucleate nitride nanocrystals in the FIB-processed regions.

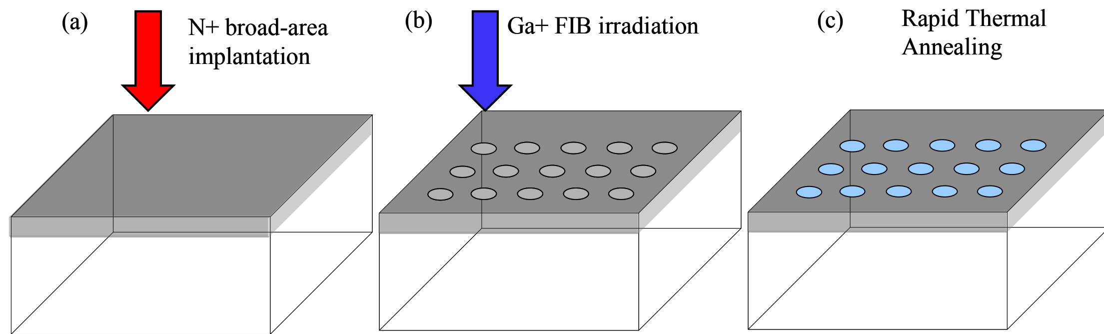

Fig. 6.6 Schematic of the 2-D directed matrix seeding process. N+ ions are broad-area implanted into the substrate to create a highly damaged, N-rich surface (a). Ga+ FIB irradiation is used to introduce a patterned surface of elevated vacancy concentration (b). Following thermal annealing, GaN is nucleated in the FIB irradiated regions (c).

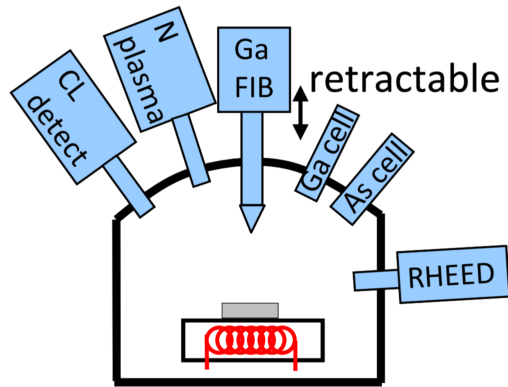

Fig. 6.7 Schematic of in-situ MBE/FIB experiment for nitride nanostructure growth. Conventional MBE growth is used to grow thin films of Ga(In)NAs. The sample is then processed using a UHV FIB mounted directly on the growth chamber and annealed using a substrate heater. This process can then be repeated to create multiple layers of nitride nanostructures.

6.3 References

[1] L. D. Hicks and M. S. Dresselhaus, *Phys. Rev. B* **47**, 12727 (1993).

[2] L. D. Hicks and M. S. Dresselhaus, *Phys. Rev. B* **47**, 16631 (1993).

[3] R. R. Collino, "Blister formation and layer transfer of N-implanted GaAs", Ph.D. thesis, University of Michigan, Ann Arbor, p. 111 (2010).

[4] R. R. Collino, "Blister formation and layer transfer of N-implanted GaAs", Ph.D. thesis, University of Michigan, Ann Arbor, p. 109 (2010).

[5] J. M. Zide, A. C. Gossard, W. Kim, S. Singer, A. Majumdar, R. Singh, Z. Bian, Y. Zhang, and A. Shakouri, *Appl. Phys. Lett*. **88**, 113502 (2006).

[6] G. A. Antonelli, B. Perrin, B. C. Daly, and D. G. Cahill, *MRS Bulletin* **31**, 607 (2006).

[7] J. Nye, *Physical Properties of Crystals* (Oxford University Press, Oxford, 1967).

[8] C. Thomsen, H. T. Grahn, H. J. Maris, and J. Tauc, *Phys. Rev. B* **34**, 4129 (1986).

[9] G. A. Antonelli, B. Perrin, B. C. Daly, and D. G. Cahill, *MRS Bulletin* **31**, 607 (2006).

[10] M. Kondow, T. Kitani, S. Nakatsuka, M. C. Larson, K. Nakahara, Y. Yazawa, M. Okai, and K. Uomi, *IEEE J. Sel. Areas Commun*. **3**, 719 (1997).

[11] M. Mikulics, M. Marso, I. Camara Mayorga, and R. Güsten, *Appl. Phys. Lett.* **87**, 041106 (2005).

[12] S. Dhara, P. Magudapathy, R. Kesavamoorthy, S. Kalavathi, K. G. M. Nair, G. M. Hsu, L. C. Chen, K. H. Chen, K. Santhakumar, and T. Soga, *Appl. Phys. Lett*. **87**, 261915 (2005).

[13] K. M. Yu, W. Walukiewicz, M. A. Scarpulla, O. D. Dubon, J. Wu, J. Jasinski, Z. Liliental-Weber, J. W. Beeman, M. R. Pillai, and M. J. Aziz, *J. Appl. Phys*. **94**, 1043 (2003).

[14] X. Weng, R. S. Goldman, V. Rotberg, N. Bataiev, and L. J. Brillson, *Appl. Phys. Lett.* **85**, 2774 (2004).

[15] X. Weng, S. J. Clarke, W. Ye, S. Kumar, R. S. Goldman, A. Daniel, R. Clarke, J. Holt, J. Sipowska, A. Francis, and V. Rotberg, *J. Appl. Phys.* **92**, 4012 (2002).

[16] R. R. Collino, "Blister formation and layer transfer of N-implanted GaAs", Ph.D. thesis, University of Michigan, Ann Arbor, p. 182 (2010).

[17] P. Munusamy, V. Mahalingam, and F. C. J. M. van Veggel, *Eur. J. Inorg. Chem*. **2008**, 3728 (2008).

[18] C. W. Wu, C. W. Lu, Y. P. Lee, Y. J. Wu, B. M. Cheng, and M. C. Lin, *J. Mater. Chem*. **21**, 8540 (2011).

[19] A. K. Mann, D. Varandani, B. R. Mehta, L. K. Malhotra, G. Mangamma, and A. K. Tyagi, *Bull. Mater. Sci.* **31**, 233 (2008).

[20] T. Stoica, R. J. Meijers, R. Calarco, T. Richter, E. Sutter, and H. Lüth, *Nanoletters* **6**, 1541 (2006).

[21] H. Czichos, T. Saito, L. R. Smith, and L. Smith, *Springer Handbook of Materials Measurement Methods* **978**, 549 (2006).

[22] A. Klumpp, P. Ramm, G. Franz, C. Rue, and L. Kwakman, *Interconnect Technology Conference and 2011 Materials for Advanced Metallization*, p. 1-3 (2011).

[23] N. S. Smith, W. P. Skoczylas, S. M. Kellogg, D. E. Kinion, P. P. Tesch, O. Sutherland, A. Aanesland, and R. W. Boswell, *J. Vac. Sci. Technol. B* **24**, 2902 (2006).

[24] P. Y. Nabhiraj, R. Menon, G. M. Rao, S. Mohan, R. K. Bhandari, *Vacuum Electronics Conference*, p. 395-396 (2011).

Appendices

Appendix A

Selected Area Electron Diffraction Analysis

Electrons impinging at a glancing angle θ to planes of atoms with interplanar spacing d are reflected if Bragg's equation is satisfied:[1,2]

$$2d \sin\theta = \lambda \tag{A.1}$$

where λ is the wavelength of the electrons. From Fig. A.1, it is apparent that the angle between the incident electron beam and the diffracted electron beam is 2θ. If the electron beam is incident on a polycrystalline specimen, the diffracted beams will form a cone with semi-angle 2θ, as shown in Fig. A.2. The beam will then ne incident on the TEM phosphor screen in a circle of radius R, such that

$$R / L = \tan 2\theta \tag{A.2}$$

where L is the distance between the specimen and the phosphor screen. The angle 2θ is only a few degrees when the accelerating voltage is on the order of tens of kilovolts.[1] Thus, we make the small angle approximation that $\sin\theta \approx \theta$ or $\tan 2\theta \approx \theta$. Solving Eq. A.1 and Eq. A.2 for θ and setting them equal to each other, we find

$$Rd = \lambda L \tag{A.3}$$

where λ and L are constants associated with the TEM. We can then solve for d by measuring R. We measure the radius of the ring R using the method described below.

The diffraction image is loaded into a graphics program which denotes pixel coordinate values. We used Microsoft Paint, although ImageJ offers similar capabilities using standard measurement units, although the resolution (0.01") is not as high as individual pixel coordinates using Paint. For each polycrystalline ring, several pixel coordinates are denoted for points on the ring, making sure to denote pixel coordinates from points along the entire circumference ring when possible. This procedure is repeated for each ring.

The pixel coordinates denoted must be converted to a radius. To do this, the center of the diffraction pattern is found. When there are single crystal diffraction spots in the image, this is accomplished by connecting diffraction spots along a line, and connecting diffraction spots along a line approximately parallel to the first, as shown in Fig. A.3(a). The intersection of these two lines is the center of the diffraction pattern and the pixel coordinates are denoted. When there are only polycrystalline rings in the diffraction pattern, the center of the image may be found by using the outermost diffraction ring to circumscribe a rectangle, as shown in Fig. A.3(b) The diagonals of the rectangle intersect at the center of the diffraction pattern and the pixel coordinates of the center are denoted.

The pixel coordinates from spot n along the polycrystalline ring (x_n,y_n) are then normalized with respect to the center coordinates (x_c,y_c) using the following relation:

$$(x_{norm}, y_{norm}) = (x_n - x_c, y_n - y_c) \, . \tag{A.4}$$

The radius, in units of pixels, are calculated using the following equation:

$$R = \sqrt{x_{norm}^2 + y_{norm}^2} \quad . \tag{A.5}$$

To obtain d from the radial values calculated from Eq. A.5, a known value of d must be used. When there are single crystal diffraction spots in the image, d can be obtained directly from standard values listed with the International Centre for Diffraction Data (ICDD). When there are only polycrystalline rings in the diffraction pattern, d and its associated R (related by Eq. A.3) can be obtained for a specific reflection from an image taken during the same TEM session using the same camera length and accelerating voltage. Because the right side of Eq. A.3 is constant, two arbitrary reflections in the diffraction pattern are related by the equation

$$R_1 d_1 = R_2 d_2 = \lambda L . \quad \text{(A.6)}$$

We define d_1 as the known value of d, we and solve for d_2:

$$d_2 = \frac{R_1 d_1}{R_2} \quad \text{(A.7)}$$

The crystal structure (e.g. ZB GaAs, ZB GaN, or WZ GaN) is then determined by comparing the calculated d spacings with the d spacings from ICDD. The observed reflections are then compared with (1) the predicted highest intensity reflections, also listed in ICDD, and (2) the predicted ordering of the rings with respect to each other. An example of the predicted intensities and ordering of diffraction reflections for ZB GaN is presented in Table A.1.

Table A.1 The d-spacings and predicted intensities and ordering of reflections for ZB GaN diffraction.

d (Å)	h	k	l	I (normalized)
2.599	1	1	1	100
2.250	2	0	0	6
1.592	2	2	0	17
1.358	3	1	1	12
1.300	2	2	2	4
1.126	4	0	0	1
1.033	3	3	1	3

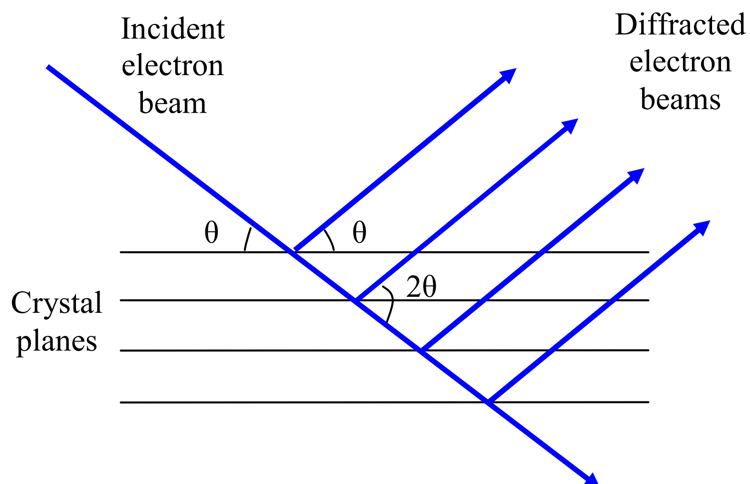

Fig. A.1 Schematic of electron diffraction from crystal planes. The incident electron beam impinges on the sample at angle θ. The diffracted beams are reflected at an angle 2 θ with respect to the incident beam. (Adapted from Ref. 1)

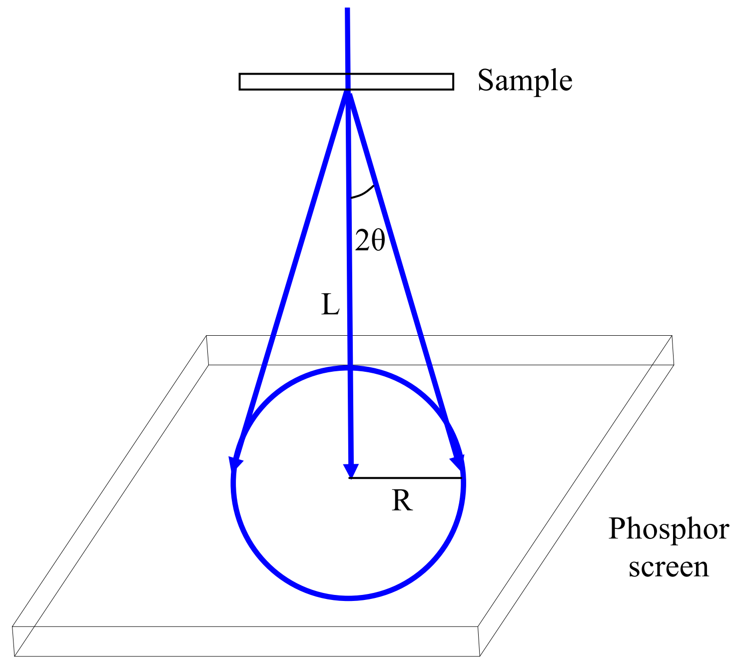

Fig. A.2 Schematic of polycrystalline electron diffraction. The incident electron beam is diffracted from the sample, forming a cone with semi-angle 2θ. The diffracted beams then form a circle of radius R on the phosphor imaging screen. (Adapted from Ref. 1)

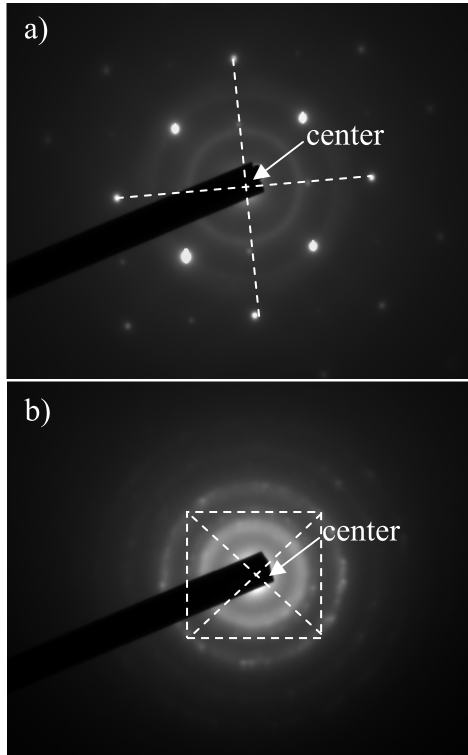

Fig. A.3 Examples of locating the center of a diffraction image (a) when single-crystal diffraction spots are visible and (b) when only polycrystalline rings are visible.

References

---

[1] T. B Rymer, *Electron Diffraction* (Methuen & Co. Ltd., London 1970) p.7.

[2] [2] D. B. Williams and C. Barry Carter, eds. *Transmission Electron Microscopy* (Springer Science+Business Media, Inc. New York, 1996), Chapter 35.

Appendix B

Calculation of Atomic Ratio Using the Cliff-Lorimer Factor

EDX maps of In, As, and N were collected from regions ~540 x 420 nm. To determine the depth distribution of N, we assume a uniform sample thickness and estimate a Cliff-Lorimer factor for InAs, k_{InAs}, from EDX data collected in regions of pure InAs, typically at depths from 250 to 300 nm below the surface.

The atomic percents of each element, C_A and C_B, can be related to the measured intensities by the Cliff-Lorimer equation: [1]

$$\frac{C_A}{C_B} = k_{AB}\frac{I_A}{I_B} \tag{B.1}$$

To determine the depth distribution of N, we assume a uniform sample thickness and calculate a Cliff-Lorimer factor for InAs, k_{InAs}, from EDX data collected in regions of pure InAs, typically at depths from 250 to 300 nm below the surface. For InAs, C_A=C_B = 0.5, and from Eq. B.1, k_{InAs} can be expressed as follows:

$$k_{InAs} = \frac{I_{As}}{I_{In}} \tag{B.2}$$

By averaging values of I_{As} and I_{In}, presented in Table B.1, for depths greater than 250 nm, we calculate a value of k_{InAs}=1.328.

We next assume a uniform distribution of In and calculate the relative atomic percents of As using the following equations:

$$C_{As} = \frac{0.5}{k_{InAs}} \cdot \frac{I_{As}}{I_{In}} \quad \text{(B.3)}$$

$$C_N = 1 - C_{In} - C_{As} \quad \text{(B.4)}$$

Measured values of I_{In}, I_{As}, I_N, and Calculated values of C_{As} and C_N are presented in Table B.1.

Table B.1 Measured values of XEDS signal intensity of In, As, and N with calculated values of the atomic percents of As and N.

Depth (nm)	I_N	I_{In}	I_{As}	I_{As}/I_{In}	C_{As}	C_N
0	5	86	38	0.44186	16.46128	33.53872
0.002	5	99	40	0.40404	15.05231	34.94769
0.005	5	123	47	0.382114	14.23545	35.76455
0.007	6	137	44	0.321168	11.96494	38.03506
0.01	8	168	31	0.184524	6.874336	43.12566
0.012	6	174	24	0.137931	5.138547	44.86145
0.014	8	187	20	0.106952	3.984435	46.01557
0.017	7	188	19	0.101064	3.765079	46.23492
0.019	5	180	16	0.088889	3.311508	46.68849
0.021	2	173	20	0.115607	4.306875	45.69313
0.024	2	140	23	0.164286	6.120376	43.87962
0.026	2	130	22	0.169231	6.304602	43.6954
0.029	2	104	24	0.230769	8.597184	41.40282
0.031	2	104	22	0.211538	7.880752	42.11925
0.033	5	101	14	0.138614	5.163985	44.83601
0.036	5	112	11	0.098214	3.658921	46.34108
0.038	4	118	13	0.110169	4.104305	45.89569
0.04	3	105	23	0.219048	8.160502	41.8395
0.043	4	104	24	0.230769	8.597184	41.40282
0.045	2	90	29	0.322222	12.00422	37.99578
0.048	2	87	35	0.402299	14.98743	35.01257
0.05	1	63	49	0.777778	28.9757	21.0243
0.052	1	61	42	0.688525	25.65062	24.34938
0.055	2	58	60	1.034483	38.5391	11.4609
0.057	2	60	63	1.05	39.11719	10.88281
0.059	2	71	62	0.873239	32.53207	17.46793
0.062	4	71	61	0.859155	32.00736	17.99264
0.064	3	72	54	0.75	27.94085	22.05915
0.067	3	77	56	0.727273	27.09416	22.90584
0.069	1	64	66	1.03125	38.41867	11.58133
0.071	1	65	67	1.030769	38.40076	11.59924
0.074	1	57	68	1.192982	44.44392	5.556077
0.076	1	43	66	1.534884	57.18127	-7.18127
0.078	0	43	76	1.767442	65.8451	-15.8451
0.081	1	52	70	1.346154	50.15024	-0.15024
0.083	1	51	82	1.607843	59.89934	-9.89934
0.086	1	46	83	1.804348	67.22001	-17.22
0.088	0	47	91	1.93617	72.13099	-22.131
0.09	0	50	82	1.64	61.09732	-11.0973
0.093	0	51	89	1.745098	65.01269	-15.0127
0.095	1	58	96	1.655172	61.66256	-11.6626
0.097	1	62	99	1.596774	59.48697	-9.48697

0.1	2	79	106	1.341772	49.987	0.012996
0.102	3	85	114	1.341176	49.96481	0.035188
0.105	5	95	128	1.347368	50.19549	-0.19549
0.107	4	108	134	1.240741	46.22313	3.776867
0.109	3	102	132	1.294118	48.21166	1.788339
0.112	3	108	143	1.324074	49.32767	0.672329
0.114	2	114	143	1.254386	46.73148	3.268522
0.116	2	136	154	1.132353	42.1852	7.814797
0.119	1	134	146	1.089552	40.59069	9.409314
0.121	1	140	133	0.95	35.39174	14.60826
0.124	1	151	143	0.94702	35.28072	14.71928
0.126	2	151	153	1.013245	37.7479	12.2521
0.128	3	141	165	1.170213	43.59565	6.404349
0.131	5	149	162	1.087248	40.50485	9.495145
0.133	4	149	182	1.221477	45.50545	4.494546
0.135	3	144	193	1.340278	49.93133	0.068668
0.138	2	156	180	1.153846	42.98592	7.014079
0.14	1	157	204	1.299363	48.40708	1.592924
0.143	3	158	198	1.253165	46.68598	3.314025
0.145	3	159	181	1.138365	42.40917	7.590829
0.147	3	152	187	1.230263	45.8328	4.167204
0.15	3	151	186	1.231788	45.88961	4.110394
0.152	3	160	166	1.0375	38.65151	11.34849
0.154	3	154	180	1.168831	43.54418	6.45582
0.157	5	163	183	1.122699	41.82557	8.174435
0.159	6	162	180	1.111111	41.39385	8.60615
0.162	6	163	173	1.06135	39.54002	10.45998
0.164	6	157	173	1.101911	41.0511	8.948901
0.166	6	155	183	1.180645	43.9843	6.015696
0.169	5	157	197	1.254777	46.74605	3.253951
0.171	2	164	190	1.158537	43.16066	6.839339
0.174	1	170	187	1.1	40.97991	9.020088
0.176	3	176	176	1	37.25447	12.74553
0.178	3	173	181	1.046243	38.97721	11.02279
0.181	3	179	179	1	37.25447	12.74553
0.183	1	165	174	1.054545	39.28653	10.71347
0.185	2	152	168	1.105263	41.17599	8.824012
0.188	5	149	153	1.026846	38.25459	11.74542
0.19	7	137	151	1.10219	41.06149	8.938509
0.193	6	150	153	1.02	37.99955	12.00045
0.195	5	136	158	1.161765	43.28092	6.719077
0.197	4	122	179	1.467213	54.66024	-4.66024
0.2	4	125	175	1.4	52.15625	-2.15625
0.202	2	128	182	1.421875	52.97119	-2.97119
0.204	2	115	175	1.521739	56.69158	-6.69158
0.207	2	114	156	1.368421	50.97979	-0.97979
0.209	1	123	155	1.260163	46.94668	3.053316
0.212	2	124	160	1.290323	48.07028	1.929722
0.214	1	134	159	1.186567	44.20493	5.795075
0.216	2	132	163	1.234848	46.00362	3.99638

0.219	2	140	180	1.285714	47.8986	2.101402
0.221	4	157	183	1.165605	43.42399	6.576006
0.223	5	161	187	1.161491	43.27071	6.729286
0.226	5	168	195	1.160714	43.24179	6.75821
0.228	2	151	195	1.291391	48.11007	1.889929
0.231	3	161	198	1.229814	45.81605	4.18395
0.233	3	158	207	1.310127	48.80807	1.191935
0.235	3	168	211	1.255952	46.78983	3.210166
0.238	2	165	210	1.272727	47.41477	2.585226
0.24	2	173	214	1.236994	46.08356	3.916442
0.242	1	155	227	1.464516	54.55977	-4.55977
0.245	1	151	226	1.496689	55.75834	-5.75834
0.247	2	148	224	1.513514	56.38514	-6.38514
0.25	2	154	215	1.396104	52.0111	-2.0111
0.252	2	167	201	1.203593	44.83921	5.160793
0.254	1	164	192	1.170732	43.61498	6.385016
0.257	0	140	197	1.407143	52.42235	-2.42235
0.259	0	84	123	1.464286	54.55118	-4.55118

References

---

[1] D. Williams and C. B. Carter, in *Transmission Electron Microscopy: a Textbook for Materials Science*, (Springer Science+Business Media, Inc., New York, 1996), p.600.

Appendix C

Free Energy of Wurtzite and Zincblende Nanocrystal Nucleation

We examine the size-dependence of nanocrystal phase by considering the free energy for the nucleation of ZB and WZ InN and GaN. The nanocrystals form in an amorphous matrix; thus, strain is not expected to play a role in their nucleation. Therefore, we assume an unstrained spherical solid nucleating from a liquid. We note that the change in free energy needed for the formation of a solid nucleus from a liquid melt with volume V_s and surface area A_{sL} is given by

$$\Delta G = V_s \left(\frac{G_v^s}{V_m} - \frac{G_v^L}{V_m}\right) + A_{sL}\gamma_{SL} \quad \text{(C.1)}$$

where G_v^s and G_v^L are the Gibbs free energy of the solid and liquid, respectively; γ_{SL} is the interface energy between the cluster and the surrounding matrix; and V_m is the molar volume.

We now consider the term $G_v^s - G_v^L$. At a temperature, T, the change in free energy is:

$$G_v^s - G_v^L = \Delta H_v - T\Delta S_v \quad \text{(C.2)}$$

$G_v^s - G_v^L$ must be less than 0 for energetically favorable solidification. Let T_n be the temperature at which nucleation occurs. Then

$$\Delta H_v(T_n) - T_n \Delta S_v = 0 \quad \text{(C.3)}$$

$$\Delta S_v = \frac{\Delta H_v(T_n)}{T_n} \quad \text{(C.4)}$$

In the temperature range of 298 to 1400 K, the formation enthalpy of GaN fluctuates by ~5%;[1] therefore, we consider it to be temperature-independent. Inserting Eq. C.4 into Eq. C.2, we obtain:

$$G_v^s - G_v^L = \Delta H_v - T\frac{\Delta H_v}{T_n} \quad \text{(C.5)}$$

Substituting Eq. C.5 into Eq. C.1, we obtain the following expression for the change in free energy:

$$\Delta G = V_s\left(\frac{\Delta H_v}{V_m} - T\frac{\Delta H_v}{V_m T_n}\right) + A_{sL}\gamma_{SL} \quad \text{(C.6)}$$

To calculate the interfacial energy, we consider the method of Miedema and den Broeder.[2] For InN nucleation, we approximate the crystal-melt interface entropy to be that of In and obtain the following expression for the interface energy between the solid InN nanocrystal and the liquid matrix:

$$\gamma = 2.5E-9\frac{\Delta H_v}{V_m^{2/3}} + 0.50E-10\frac{T_n}{V_m^{2/3}} \quad \text{(C.7)}$$

with energy units of kJ.

For GaN nucleation, we approximate the crystal-melt interface entropy to be that of Ga and obtain the following expression for the interface energy between the solid GaN cluster and the liquid matrix:

$$\gamma = 2.5E-9\frac{\Delta H_v}{V_m^{2/3}} + 0.65E-10\frac{T_n}{V_m^{2/3}} \quad \text{(C.8)}$$

To calculate the total free energy, we consider the enthalpy of formation of ZB and WZ InN and GaN, listed in Table C.1. For WZ InN, we use ΔH_v^{WZ} = -146.5 kJ/mol;[3] however, the thermodynamic properties of ZB InN are not widely reported. Instead, we consider the relative enthalpies of ZB and WZ GaN at 1 atm, with $\Delta H_v^{ZB} = 0.991\,\Delta H_v^{WZ}$.[4] Assuming that this relation is comparable for the relative enthalpies of ZB and WZ InN, we use a value of ΔH_v^{ZB} = -145.2 kJ/mol. For RTA at 600ºC, the expression for the change in free energy as a function of radius for ZB and WZ InN becomes

$$\Delta G_{InN}^{ZB} = r^3(-2.155E-23kJ/A^3) + r^2(7.281E-23kJ/A^2) \quad \text{(C.9)}$$

$$\Delta G_{InN}^{WZ} = r^3(-2.159E-23kJ/A^3) + r^2(7.306E-23kJ/A^2)\,. \quad \text{(C.10)}$$

For WZ GaN, we use ΔH_v^{WZ} = -131.326 kJ/mol.[1] We again consider the relative enthalpies of GaN at 1 atm, with $\Delta H_v^{ZB} = 0.991\,\Delta H_v^{WZ}$.[4] We therefore use a value of ΔH_v^{ZB} = -130.144 kJ/mol. For RTA at 800ºC, the change in free energy as a function of radius for ZB and WZ GaN becomes

$$\Delta G_{GaN}^{ZB} = r^3(-2.833E-23kJ/A^3) + r^2(8.588E-23kJ/A^2) \quad \text{(C.11)}$$

$$\Delta G_{GaN}^{WZ} = r^3(-2.987E-23kJ/A^3) + r^2(8.911E-23kJ/A^2)\,. \quad \text{(C.12)}$$

Table C.1 Values of enthalpy of formation as used in the calculation of free energy of formation for nanocrystal GaN and InN.

Parameter	GaN	InN
ΔH_v^{ZB} (kJ/mol)	-130.144	-145.2
ΔH_v^{WZ} (kj/mol)	-131.326	-146.5

References

[1] K. T. Jacob, and G. Rajitha, *J. Crys. Growth* **311**, 3806 (2009).

[2] A. R. Miedema, F. J. A. den Broeder, *Z. Metallkd* **70**, 14 (1979)

[3] I. Zięborak-Tomaszkiewicz and P. Gierycz, *J. Therm. Analysis Calor*. **93**, 693 (2008)

[4] X. Sun, Q. Chen, Y. Chu, and C. Wang, *Physica B* **368**, 243 (2005)

Appendix D

Measuring Thermal Conductivity Using Pump/Probe

We consider the pump/probe experimental setup shown schematically in Fig. D.1. A short laser pulse (<1 psec) of energy Q is incident on a metal film of thickness d. We assume that the optical absorption length, ξ, is much smaller than d. The dimensions of the area illuminated by the light pulse, A, are assumed to be large compared to d and ξ. The total energy deposited per unit volume at a distance z into the film is given by

$$\Delta T(z) = (1 - R)\frac{Q}{C(\xi A)}\exp^{-z/\xi} \qquad \text{(D.1)}$$

where R is the reflectivity.[1]

We can extract the value of the thermal conductivity, κ, of the sample by comparing ΔT to the results of a one-dimensional heat flow calculation, as described in Ref. 2. We assume that the temperature of the metal film is uniform throughout its thickness at times greater than 30 ps. We also assume that the lateral heat flow is negligible compared to the heat flow into the sample. Within the sample, the heat flow away from the metal interface will obey the one-dimensional diffusion equation:

$$\kappa \frac{\partial^2 T_s(z,t)}{\partial z^2} = c_s \frac{\partial T_s(z,t)}{\partial t} \qquad \text{(D.2)}$$

where $T_s(z,t)$ is the temperature of the sample at depth z and time t, and c_s is the specific heat per unit volume of the sample.

The rate of energy loss from the metal film must also be equal to the energy flux into the sample:

$$\kappa \frac{\partial T_s(z,t)}{\partial z}\bigg|_{z=0} = c_s d \frac{\partial T_m(t)}{\partial t} \qquad \text{(D.3)}$$

where $T_m(t)$ is the temperature of the metal film.

We also consider the effect of the thermal-boundary resistance, R_K, which is defined as the ratio of the temperature difference across the metal/sample interface to the heat flow per unit area through the metal/sample interface. This is described by:

$$\kappa \frac{\partial T_s(z,t)}{\partial z}\bigg|_{z=0} = -\frac{T_m(t) - T_s(0,t)}{R_K} \qquad \text{(D.4)}$$

We then vary the unknown parameters, κ and R_K, until we have obtained a curve that best fits the data.

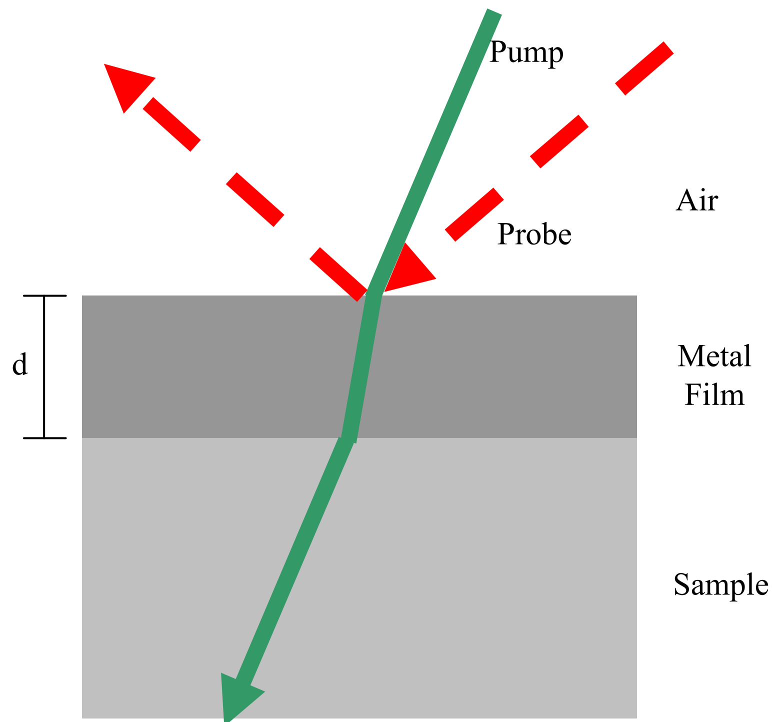

Fig. D.1 Experimental setup for pump/probe time-domain thermoreflectance measurements. A pump laser pulse is incident on a metal film of thickness d. The heat generated from the pulse flows into the sample. A probe laser pulse is used to detect changes in the reflectance. (Adapted from Ref. 1)

References

[1] C. Thomsen, H. T. Grahn, H. J. Maris, and J. Tauc, *Phys. Rev. B* **34**, 4129 (1986).

[2] G. A. Antonelli, B. Perrin, B. C. Daly, and D. C. Cahill, *MRS Bulletin* **31**, 607 (2006).